Fakultät für Medizin, Technische Universität München

Studies of the Planar Bipolar Epithelium of Zebrafish Neuromasts

Eva Lucija Kozak

Vollständiger Abdruck der von der **Fakultät für Medizin** der Technischen Universität München zur Erlangung des akademischen Grades eines **Doktors der Naturwissenschaften (Dr. rer. nat.)** genehmigten Dissertation.

Vorsitzender: Prof. Dr. Mikael Simons

Prüfende der Dissertation:

1. Prof. Dr. Heiko Lickert

2. Prof. Angelika Schnieke, Ph.D.

Die Dissertation wurde am 26.01.2021 bei der Technischen Universität München eingereicht und durch die Fakultät für Medizin am 11.05.2021 angenommen.

Abstract

Planar polarization is one of the key elements of tissue patterning. Generally, plane-polarized epithelia are formed by identically oriented cells. Exceptionally, cells may be oriented in opposite directions, thereby forming a bipolar epithelium. Neuromasts of the lateral line are a striking example of such a pattern. I leveraged this characteristic and the powerful experimental toolbox of zebrafish to gain insights into planar bipolarity. Specifically, I discovered a symmetry-breaking event that initiates the opposing orientation of sibling hair cells.

I employed a combination of single-cell transcriptional analysis, high-resolution microscopy, and genetic and pharmacological manipulations to study the spatiotemporal dynamics of Emx2, the hair-cell orientation determining factor. I found that the key step underlying planar bipolarity is the asymmetric expression of Emx2 among sibling hair cells. This occurs by a symmetry-breaking process the results in one of the cells stochastically losing Emx2 expression immediately after they are formed by the division of a progenitor cell. Importantly, the mutational analysis revealed that the Notch1a receptor is responsible for the stochastic loss of Emx2. I also found that the establishment of planar bipolarity precedes a phenomenon called planar cell inversion, which is a mysterious patterning event that occurs during the development and regeneration of hair cells in neuromasts. Quantitative live video microscopy revealed that Emx2 is dispensable for the planar cell inversion process, and that is also superfluous for the final positioning of the sibling cells along the planar polarity axis of the neuromast epithelium. Altogether, my findings provide new insights into multicellular patterning processes that govern the formation of complex tissues and organs.

Moreover, the results of this thesis contribute to the understanding of how epithelial planar bipolarity is established and maintained.

Zusammenfasung

Die planare Polarisation ist eines der Schlüsselelemente der Gewebemusterung. Im Allgemeinen werden planpolarisierte Epithelien von identisch orientierten Zellen gebildet. In Ausnahmefällen können Zellen in entgegengesetzte Richtungen ausgerichtet sein, wodurch ein bipolares Epithel gebildet wird. Ein auffälliges Beispiel für ein solches Muster sind Neuromasten des Seitenlinienorgans. Ich nutzte diese Eigenschaft und die leistungsstarke experimentelle Toolbox des Zebrafisches, um Einblicke in die planare Bipolarität zu gewinnen. Konkret entdeckte ich ein symmetriebrechendes Ereignis, das die entgegengesetzte Ausrichtung von Geschwisterhaarzellen auslöst.

Ich verwendete eine Kombination aus Einzelzelltranskriptionsanalyse, hochauflösender Mikroskopie, genetische- und pharmakologische Manipulationen, um die räumlich-zeitliche Dynamik von Emx2, den bestimmenden Faktor für die Haarzellorientierung zu untersuchen. Ich fand heraus, dass der Schlüsselschritt, der der planaren Bipolarität zugrunde liegt, der asymmetrische Ausdruck von Emx2 in den Geschwisterhaarzellen ist. Dies geschieht durch einen Symmetriebrechungsprozess, der dazu führt, dass eine der Zellen der Emx2-Ausdruck unmittelbar nach ihrer Bildung durch die Teilung der Vorläuferzelle stochastisch verliert. Überraschenderweise ergab die Mutationsanalyse, dass der Notch1a-Rezeptor für den stochastischen Verlust von Emx2 verantwortlich ist. Ich fand auch heraus, dass die Etablierung der planaren Bipolarität einem Phänomen vorausgeht, das als planare Zellinversion bezeichnet wird. Dies ist ein mysteriöses Musterungsereignis, das während der Entwicklung und Regeneration von Haarzellen in Neuromasten auftritt. Quantitative Live-Videomikroskopie ergab, dass Emx2 für den planaren Zellinversionsprozess entbehrlich ist und auch für die endgültige Positionierung der Geschwisterzellen entlang der planaren Polaritätsachse des Neuromastenepithels ohne Bedeutung ist. Meine Erkenntnisse liefern insgesamt neue Einblicke in mehrzellige Musterbildungsprozesse, die die Bildung komplexer Gewebe und Organe steuern.

Darüber hinaus tragen die Ergebnisse dieser Arbeit zum Verständnis bei, wie die epitheliale planare Bipolarität hergestellt und aufrechterhalten wird.

Acknowledgments

First of all, I want to express sincere gratitude to my supervisor **Dr. Hernán López-Schier**, who supported and guided me during my doctoral studies. He enabled me to work on the most exciting biological questions, offered me several learning opportunities, and encouraged me to explore scientific questions in different fields. I highly value his advice and appreciate his general enthusiasm for science.

Furthermore, I want to thank all the members of my thesis committee: my Ph.D. advisor **Prof. Dr. Heiko Lickert**, who always offered me kind support and constructive feedback, and **Prof. Angelika Schnieke, Ph.D.** and **Prof. Dr. Barbara Treutlein**, who both provided me valuable advice and comments on my project.

I am also very thankful to all the members of the López-Schier lab: **Laura**, **Andrés**, **Augusto**, **Petra,** and especially **Jerónimo,** with whom I had the pleasure to work in a team. I also want to thank the former members of the lab: **Oriol**, **Weili**, **Gema**, **Marta**, **Amir**, **Yan,** and **Prisca**, and the animal caretakers from the zebrafish facility.

I want to acknowledge our collaborators, with whom we had very pleasant and productive collaborations, especially **Subarna Palit**, who very largely helped me with the data analysis, and also **Aleksandar Janjic**, **Dr. Anika Böttcher**, **Dr. Osvaldo Chara**, **Prof. Dr. Wolfgang Enard,** and **Prof. Dr. Fabian J Theis**. I am most thankful for their contributions, the opportunity to work with and learn from them.

Finally, I want to thank my husband **Valter**, **family,** and **friends** for their ongoing support and encouragement.

Parts of this thesis have been published in:

Kozak, EL, Palit, S, Miranda-Rodríguez J, Janjic A, Böttcher A, Lickert H, Enard W, Theis F and López-Schier H. (2020) “Epithelial Planar Bipolarity Emerges from Notch-Mediated Asymmetric Inhibition of Emx2" Current Biology**,** volume 30, issue 6, P1142-1151.E6, https://doi.org/10.1016/j.cub.2020.01.027

Parts of this thesis result from collaborations and are acknowledged accordingly.

Table of Contents

Table of Contents

Table of Contents

List of Abbreviations

7AAD	7-AAD (7-amino-actinomycin D)
Ab	antibody
AGE	agarose gel electrophoresis
BSA	bovine serum albumin
(c)DNA	(complementary) deoxyribonucleic acid
crRNA	clustered regularly interspaced short palindromic repeats RNA
DAPI	4’,6-diamidino-2-phenylindole
DAPT	N-[N-(3,5-difluorophenacetyl)-L-alanyl]-S-phenylglycine-t-butyl ester
DC	diffusion component
DiAsp	4-(4-diethylaminostyryl)-1-methylpyridinium iodide
dpf	days post fertilization
DMSO	dimethylsulfoxide
DPT	diffusion pseudotime
e.g.	for example
E. coli	*Escherichia coli*
EDTA	ethylenediaminetetraacetic acid
(E)GFP	(enhanced) green fluorescent protein
FACS	fluorescence-activated cell sorting
FBS	fetal bovine serum
FDR	false discovery rate
GEO	Gene Expression Omnibus
GO	gene ontology
GRCz11	Genome Reference Consortium Zebrafish assembly 11
HC(s)	hair cell(s)
het	heterozygous
hom	homozygous
KEGG	Kyoto Encyclopedia of Genes and Genomes

List of Abbreviations

KO	knockout
LB	Luria broth
LPR	line of polarity reversal
lq	lower quality
mcSCRBseq	molecular crowding single-cell RNA barcoding and sequencing
(m)RNA	(messenger) ribonucleic acid
MS-222	3-aminobenzoic acid ethyl ester methanesulfonate
mut	mutant
NICD	Notch intracellular domain
nls	nuclear localization sequence
NM	neuromast
o/n	over-night
PBS	phosphate-buffered saline
PCA	principal component analysis
PCI	planar cell inversion
polyA	polyadenylation signal
QC	quality control
(sc)RNAseq	(single-cell) RNA sequencing
sgRNA	short guide RNA
RNPs	ribonucleoproteins
tracrRNA	trans-activating crispr RNA
UAS	upstream activating sequence
UHCP	unipotent hair cell progenitor
UMAP	Uniform Manifold Approximation and Projection
vs.	versus
wt	wild type
yHC(s)	young hair cell(s)

1. Introduction

1.1. Zebrafish larvae as an experimental organism

Zebrafish (*Danio rerio*) are commonly used vertebrate experimental organisms. There are numerous advantages of using zebrafish as an experimental model organism, including their small size. Furthermore, zebrafish are easy and economical to maintain (Westerfield, 2007). The zebrafish eggs develop outside the mother, facilitating early embryonic development studies; they are also commonly used for regeneration and neurobiology studies and as human disease models. Zebrafish have the same major organs and share 70 % of their genes with humans (Howe et al., 2013). A female zebrafish can lay 100 - 200 eggs per mating, providing an easily accessible large number of larvae for studies. Moreover, the zebrafish larvae can rapidly regenerate complex organs and are translucent, providing an excellent opportunity for intravital imaging-based studies (Westerfield, 2007).

1.2. Zebrafish lateral line

Aquatic vertebrates such as amphibians and fish possess a mechanosensory organ called the lateral line. The lateral line system allows such animals to detect hydrodynamic changes in their immediate vicinity. This mechanical information is transmitted to the central nervous system via afferent neurons, allowing the animal to adjust its behavior (Kalmijn, 1989). Numerous studies have shown that the lateral line plays a role in various behaviors, including escape, prey detection, sexual courtship, and rheotaxis (Kalmijn, 1989; Oteiza et al., 2017; Stewart et al., 2013). The superficial lateral-line system is subdivided into anterior and posterior sub-systems. The former is positioned anterior to the animal's ear and the latter is located posterior to the ear along the animal's trunk (Ghysen & Dambly-Chaudière, 2004; Gompel et al., 2001).

1.2.1. Posterior lateral line in larval zebrafish

The zebrafish posterior lateral line is composed of small organs called neuromasts, located on the lateral side of an animal's body and connected with a line of interneuromast cells. During the development, the pro-neuromasts (which later develop into neuromasts) are

deposited as clusters of cells left behind by migrating primordia, which progress from head to the tail (Ledent, 2002; Metcalfe et al., 1985). The first primordium (primI) starts migrating at 22 hours post fertilization (hpf), and is followed by a smaller second primordium (primII) at 38 hpf (Ghysen & Dambly-Chaudière, 2004; Metcalfe et al., 1985; Nechiporuk & Raible, 2008; Nuñez et al., 2009; Sapède et al., 2002). The direction of primordium migration along the horizontal myoseptum is set by a gradient of chemoattractant sdf1a (David et al., 2002). At the end of embryonic development, a zebrafish larva possesses 7-9 neuromasts of the posterior lateral line on each lateral side of the body (Gompel et al., 2001) (Figure 1.1). The localization of the neuromasts is stereotypic (Ledent, 2002; López-Schier et al., 2004).

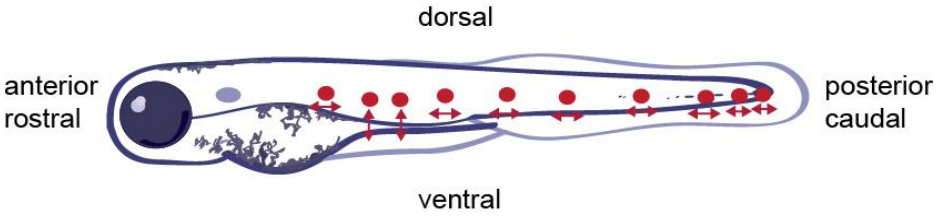

Figure 1.1: Illustration of a larva. Schematic illustration of zebrafish larvae with posterior lateral line neuromasts positions and their sensitivity axis shown in red. Anatomical terms of location are written on each side.

Interestingly, adult fish possess a much higher number of neuromasts, including canal and superficial neuromasts (Wada et al., 2010). Additional neuromasts are later formed by the proliferation of interneuromast cells (Grant et al., 2005) or through a budding process, resulting in accessory neuromasts (Ledent, 2002; Wada et al., 2010).

1.2.2. The posterior lateral line neuromast functional structure

Neuromasts are composed of 60 to 70 cells and consist of a radial-symmetric neuroepithelium (Ghysen & Dambly-Chaudière, 2007; López-Schier & Hudspeth, 2006; Norden, 2017; Viader-Llargués et al., 2018). Three main cell classes have been identified to form a neuromast (Figure 1.2): the sensory hair cells (HCs), located in the center of the organ, the supportive sustentacular cells that surround the sensory hair cells, and the supportive mantle cells that form the outer rim of the neuromast.

The hair cells act as mechanical sensors and are covered by a gelatinous cupula secreted by mantle cells (Nicolson, 2017). The sustentacular cells have been identified as tripotent progenitors involved in the replenishment of other cell type classes (Cruz et al., 2016; Viader-Llargués et al., 2018). In addition to in situ hybridization and immunostaining experiments, bulk RNA-sequencing of neuromast support cells studies provided insights into genes expressed in neuromasts during homeostasis and regeneration (L. Jiang et al., 2014; Steiner et al., 2014). Intriguingly, several subtypes of sustentacular cells have recently been identified using a single-cell RNA-sequencing (scRNAseq) approach (Lush et al., 2019). Subtypes of neuromast support cells include central support cells, anterior/posterior (A/P) pole cells, dorsal/ventral (D/V) pole amplifying cells, and unipotent hair cell progenitors (UHCPs) (Lush et al., 2019; Pinto-Teixeira et al., 2015; Wibowo et al., 2011).

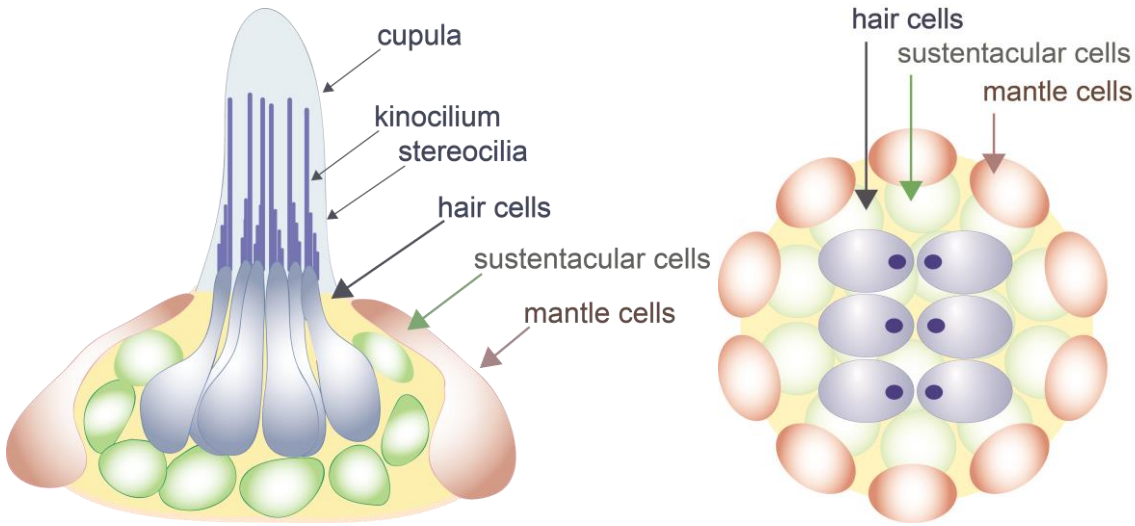

Figure 1.2: Illustration of a neuromast. Schematic illustration of the side view (left) and top view (right) of a wild-type horizontal neuromast depicting the main neuromast cell types: hair cells and supportive mantle and sustentacular cells. Each hair cell bundle is composed of stereocilia and kinocilium.

A neuromast can detect mechanical stimuli by sensory hair cells and transmit the signal to associated nerve fiber. Each neuromast can detect stimuli in both directions along its axis of sensitivity as it is composed of hair cells oriented in two opposite directions along this single axis (López-Schier et al., 2004; Wibowo et al., 2011).

1.2.3. Neuromast hair cell structure and function

Neuromast hair cells are mechanosensory cells that detect mechanical stimuli using their hair bundles. Each hair cell possesses an asymmetric hair bundle on the apical surface. The hair bundle is composed of stereocilia arranged in a staircase pattern with an additional, larger microtubule-based kinocilium at the higher edge of the stereocilia (Figure 1.2). Deflection of the bundle towards the kinocilium triggers the signal transmission by opening the ion channels, causing cell depolarization, which leads to excitation of the associated nerve fiber. A single hair cell is depolarized by the water flow from one direction only, namely towards the kinocilium (Hudspeth & Corey, 1977; Kindt et al., 2012; Shotwell et al., 1981).

1.2.4. Analogous sensory organs in other vertebrates

Neuromasts are discrete mechanosensory organs of the lateral line and are evolutionary and functionally analogous to the inner ear (Jørgensen, 1989; Kalmijn, 1989). During the evolution, the inner ear developed from the lateral line organ and consequently shares genetic, physiological, and structural similarities (Å. Flock & Lam, 1974; Jørgensen, 1989). Furthermore, the inner ear hair cells share many similarities across all vertebrate species, and known deafness gene orthologues (e.g., *tmc1*, *otofb*, and *myo6b*) are expressed both in mammalian and zebrafish hair cells (Barta et al., 2018; Whitfield et al., 1996). In the vertebrate vestibular system, the utricle and saccule are populated by patches of hair cells of the same orientation, divided by a line of polarity reversal (LPR) from the cells of opposite orientation (May-Simera & Kelley, 2012). On the contrary, oppositely oriented hair cells in neuromasts are located in the same area at the center of the organ (see also chapter 1.4.2.).

A notable distinguishing characteristic between mammalian and non-mammalian vertebrate mechanosensory hair cell populations is their ability to regenerate. Upon damage, the hair cell populations are naturally replenished in non-mammalian vertebrate species, such as fish and chicken (Brignull et al., 2009; Corwin & Oberholtzer, 1997; A. K. Groves et al., 2013) – such regeneration is not observed in mammals. Due to their inherent position on the surface of an animal, the neuromast hair cells are very prone to injury (due to ototoxicity or mechanical damage), which is compensated by their remarkable regenerative ability (Pinto-

Teixeira et al., 2015; Williams & Holder, 2000). Complete sensory hair cell recovery after their total ablation from a neuromast, and the response of support cells to the hair cell damage, has been reported in numerous studies (Harris et al., 2003; Hernández et al., 2006; L. Jiang et al., 2014; Ma et al., 2008; Namdaran et al., 2012; Pei et al., 2018; Pinto-Teixeira et al., 2015; Romero-Carvajal et al., 2015; Steiner et al., 2014; Williams & Holder, 2000). Furthermore, even when the whole organ is severely damaged, the neuromasts regenerate and regain normal proportions, geometry, and function (Cruz et al., 2015; Viader-Llargués et al., 2018). After regeneration, the organ symmetry is rebuilt by polarized cell sorting and localized differentiation (Viader-Llargués et al., 2018; Wibowo et al., 2011).

1.3. Planar cell polarity (PCP)

In addition to the apical-basal polarity, several cell types express a specific orientation within the epithelial plane, called planar cell polarity (Butler & Wallingford, 2017; Zallen, 2007). The planar polarity has first been studied by V. B. Wigglesworth in an insect *Rhodnius prolixus* (Wigglesworth, 1940). The planar cell polarity was later extensively studied in fruit flies *Drosophila melanogaster*, in which crucial planar polarity genes were identified, including *Frizzled*, *Van Gogh*, *Flamingo*, *Dishevelled*, *Prickle*, and *Diego* (Tarchini & Lu, 2019; Zallen & Wieschaus, 2004). The planar cell polarity is evolutionarily conserved in vertebrates (Goodrich & Strutt, 2011; Montcouquiol et al., 2003). Planar polarization of the epithelium is established by a core planar-polarity network that coordinates the orientation of neighboring cells and by translating global planar polarity cues (Deans, 2013; Tarchini & Lu, 2019). Planar cell polarity is an indispensable mechanism governing key morphogenetic events such as body axis elongation or patterning of cells in sensory organs (Dabdoub et al., 2003; Tarchini & Lu, 2019). Disruption of the core planar polarity pathway via, for example, the introduction of mutations in the planar polarity genes generates abnormal planar polarization consisting of changes in cellular orientation (Montcouquiol et al., 2003; J. Wang et al., 2006).

1.4. Neuromast planar bipolarity

The polarity of a neuromast hair cell is defined by the polarity of the cell's hair bundle,

precisely the anisotropic position of stereocilia and the kinocilium. The neuromast hair cells are organized with respect to an internal axis of planar polarity. There are two types of neuromasts, regarding their planar polarity axis: horizontal neuromasts with the anterior-posterior planar polarity axis, which are deposited by the first primordium, and vertical neuromasts with dorsal-ventral planar polarity axis, which are deposited by the second primordium (A. Flock & Wersall, 1962; López-Schier et al., 2004; Metcalfe et al., 1985; Nuñez et al., 2009). The neuromast planar polarity axis refers to the parallel alignment of all the hair cell bundles within a neuromast along the axis of neuromast's sensitivity. Furthermore, the planar polarity axis is established during the lateral line development (López-Schier et al., 2004). To this end, it has been shown that when the direction of the primordium migration is disrupted, the planar polarity of the deposited neuromasts correlates with the primordium migration path line (López-Schier et al., 2004). Moreover, a recent study suggests that the tissue polarity is established already in the primordia, and it, later on, determines the hair cell polarity in neuromasts (Navajas Acedo et al., 2019). Interestingly, in addition to the orientation of hair cell bundles, the alignment of the support cells along the planar polarity axis has been observed (Navajas Acedo et al., 2019).

In summary, horizontal neuromasts possess hair cells oriented parallel to the planar polarity axis, whereas in vertical neuromasts, the hair cells orient perpendicular to it. Notably, the hair cells within a single neuromast are oriented in both directions along a single axis. The orientation of hair cells on a local level is referred to as cell-intrinsic polarity.

1.4.1. Core planar polarity pathway and cell-intrinsic polarity in hair cells

The genes involved in hair cell polarity determination have been studied in zebrafish and other organisms. Briefly, the core planar polarity proteins localize asymmetrically on one side of all the hair cells within the organ, regardless of their individual orientation. The G-protein complex components are involved in the migration of the kinocilium to one edge of the cell and the formation of the staircase-patterned stereocilia, establishing the cell-intrinsic polarity (Ezan et al., 2013; Tarchini & Lu, 2019). The G-protein complex components localize asymmetrically in hair cells of opposite polarities, forming a mirror-symmetric pattern when observing the whole organ (Ezan et al., 2013; Tarchini et al., 2016). So far, the link between the core planar polarity pathway and cell-intrinsic polarity remains

incompletely understood, even though a set of proteins interacting with components of both pathways has been recently identified (Siletti et al., 2017).

In neuromasts, distinct components of the core planar polarity pathway and wnt signaling pathway have been shown to play a role in establishing neuromast hair cell polarity using a genetic approach. *vangl2* is a vertebrate homolog of the *Van Gogh* gene in *Drosophila* and is one of the components establishing core planar polarity in zebrafish neuromasts. *vangl2* mutant larvae (also known as trilobite mutants) possess randomly orientated hair cells (López-Schier & Hudspeth, 2006; Navajas Acedo et al., 2019). Furthermore, the asymmetric subcellular localization of Vangl2 has been shown directly: Vangl2 localizes at the caudal edges of hair cells in horizontal neuromasts and ventral edges in vertical neuromasts (Mirkovic et al., 2012; Navajas Acedo et al., 2019). A similar phenotype with randomly oriented hair cells has been demonstrated in another core planar polarity gene mutant, namely in the *scrib* mutant larvae (Navajas Acedo et al., 2019). In contrast, the mutations in the genes involved in the wnt signaling pathway, specifically in *wnt11f1*, *gpc4*, and *fzd7a/b*, cause abnormal hair cell orientation with concentric pattern (Navajas Acedo et al., 2019). Moreover, the mutations in the wnt signaling pathway genes do not affect the PCP pathway and might indirectly affect hair cell orientation (Navajas Acedo et al., 2019).

In short, the hair cell polarity is regulated by the core planar polarity pathway and cell-intrinsic polarity pathway, both affecting the orientation of mechanosensory hair cells.

1.4.2. Neuromast mirror symmetry

Neuromasts of the lateral line are one of the few exceptions in nature, where the plane-polarized cells orient themselves not in parallel but opposite directions (Figure 1.3 A). This phenomenon, called bipolarity, is established in neuromasts in the early stages of organ development and results in a mirror-symmetric pattern (Figure 1.3 B).

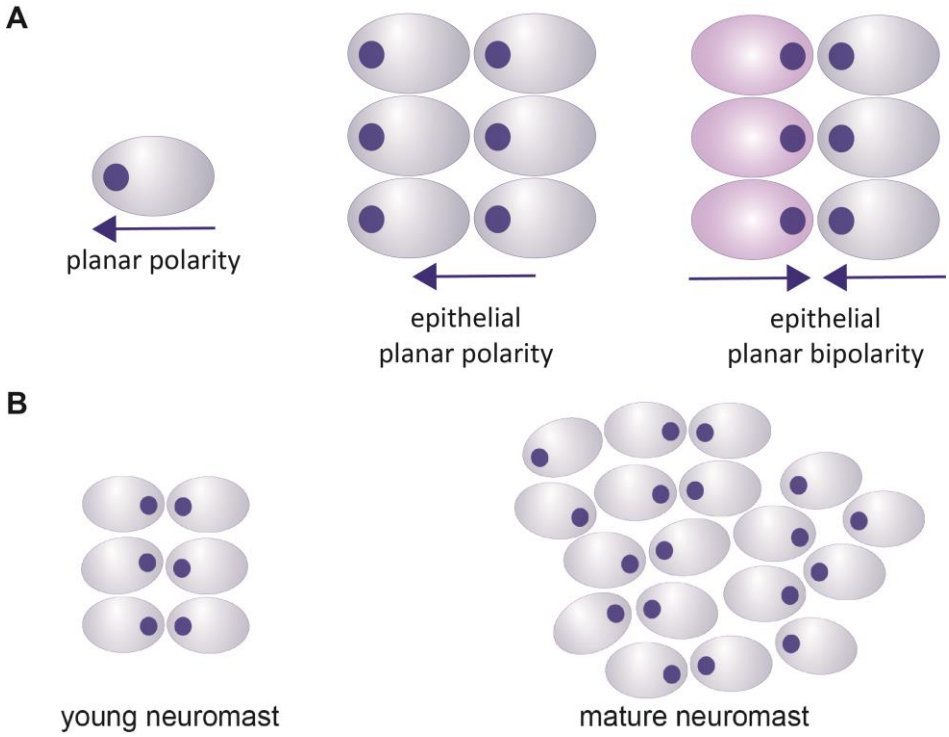

Figure 1.3: Illustration of an epithelial planar bipolarity. (**A**) Illustration depicting the difference between a plane-polarized cell, planar epithelial polarity, and epithelial planar bipolarity using hair cells with kinocilia (blue dots). (**B**) An illustration is depicting neuromast mirror symmetry with a realistic approximation of hair cells' orientation. Note that a transient establishment of the line of polarity reversal is visible in neuromasts containing only a few hair cell pairs (a phase during the development or regeneration).

Hair cells arise by mitotic division of a non-sensory epithelial cell, the unipotent hair cell progenitor (UHCP). Two daughter hair cells have opposite polarities with the kinocilia of sibling hair cells pointing towards each other in 96% of the cases (López-Schier et al., 2004; Navajas Acedo et al., 2019). During the production of the first 3 – 4 couples of hair cells, there is a clear correlation of hair cell polarity and location, resulting in a line of polarity reversal (LPR). In other words, the neuromast hair cell bundles are positioned in a mirror-symmetric pattern, reminiscent of what is observed in analogous mammalian organs, albeit on a smaller scale (López-Schier & Hudspeth, 2006; Wibowo et al., 2011). Nevertheless, this line of polarity reversal is only transient in neuromasts and is rapidly blurred upon organ maturation (Figure 1.3 B). Importantly, Emx2 has been recognized as the key genetic factor determining the orientation of the polarized hair cells (Holley et al., 2010; Y. R. Ji et al.,

2018).

1.4.2.1. Hair cell orientation terminology

In this thesis, I would like to clarify that the direction of the hair cell planar polarity is referred to as **hair cell orientation** to stress the difference between the hair cell planar polarity and its direction. The **hair cell polarity** term is referring to the asymmetry of the hair cell bundle. The neuromast hair cells are all plane-polarized in the same manner (asymmetric position of hair bundle), but they are oriented in distinct directions. In other words, each hair cell is plane-polarized or oriented in a particular direction. Furthermore, following the nomenclature protocol introduced by Dow et al. (2018), the terms **anterior and posterior** are used for describing hair cell position. In contrast, the terms **rostral and caudal** are used for describing hair cell orientation and its sensitivity (Figure 1.1). In horizontal neuromasts, two sibling hair cells have opposite orientations: the anterior hair cell possesses caudad orientation, and the posterior hair cell possesses rostrad orientation.

1.4.3. The role of Emx2 in neuromast hair cell polarity

1.4.3.1. Emx2, general overview

emx2 (*empty spiracles homeobox 2*) is a homeodomain-containing transcription factor homologous to the *ems* (*empty spiracles gene*) in *Drosophila*. The zebrafish Emx2 consists of 247 amino acids (28 kDa).

Studies in various organisms have shown that *Emx2* is expressed in a wide variety of epithelial tissues, such as the developing ureters, urogenital system, and brain (Bayatti et al., 2008; Cecchi, 2002; Pellegrini et al., 1997; Taylor, 2015). Furthermore, Emx2 is important for many processes, including neuro- (Cecchi, 2002) and bone development (Askary et al., 2017; Pröls et al., 2004). For example, *Emx2* is required for cortex patterning (Cholfin & Rubenstein, 2008; Simeone et al., 1992), where it defines the posterior-medial area of the neocortex, influencing proliferation, identity, and position of cortical neuronal progenitors (Sierra et al., 2015). Mutations in the *Emx2* gene result in a broad range of phenotypes, e.g. in mice loss of *Emx2* expression in the kidneys results in death shortly after birth (Miyamoto et al., 1997). In *Emx2* mutant animals, distinct brain structures are reduced or absent, largely

due to decreased cell proliferation (Pellegrini et al., 1996; Yoshida et al., 1997). Furthermore, downregulation of Emx2 leads to defects in migration, differentiation, and innervation in specific neuronal populations (Cecchi, 2002). Moreover, altered expression of *Emx2* has been discovered (Abate-Shen, 2002), and a tumor suppressor role of *Emx2* was reported in several cancers (Monnier et al., 2018; L. Wang et al., 2019).

Altogether, *Emx2* is expressed in many epithelial tissues and plays a vital role in distinct developmental processes. Disruption of Emx2 expression has been linked with several disease states.

Emx2 is expressed in various tissues, where it modulates the expression of its target genes, for instance, genes from Ten-m/Odz/teneurins family (Beckmann et al., 2011; Li et al., 2006). Furthermore, studies in various organisms have identified or predicted several interaction partners of Emx2, suggesting potential novel roles of Emx2. For instance, in the neocortex, Emx2 binds to Sp8 (Zembrzycki et al., 2007); during the scapula formation, Emx2 cooperates with pbx1 (Pröls et al., 2004). In axons of olfactory sensory neurons, it interacts with the translation initiation factor eIF4E (Nédélec et al., 2004). Emx2 functionally interacts and overlaps with other transcription factors, such as Dmrt3 and Dmrt5 (Desmaris et al., 2018). It could be involved in post-transcriptional gene regulation by interacting with Quaking protein isoforms (J. A. Groves et al., 2019). Emx2 may also function outside of the nucleus (Nédélec et al., 2004).

In short, the transcription factor Emx2 has several known or predicted target genes. Additionally, novel targets of Emx2 and novel molecular mechanisms of Emx2 function are still being discovered.

1.4.3.2. Discovering the role of Emx2 in hair cell orientation

The involvement of *Emx2* in hair cell orientation determination was first discovered in the mice vestibular system in 2010 (Holley et al., 2010) after middle and inner ear defects have been observed in *Emx2* mutant mice (Rhodes et al., 2003). A patterning defect and an abnormal hair cell number in the mice organ of Corti have been observed in the heterozygous mice carrying a missense mutation in the *Emx2* gene and heterozygous *Emx2*

knockout (KO) mice, but no defects in polarity were reported at the time (Rhodes et al., 2003). Scanning electron microscopy revealed the absence of cell polarity reversal across the striola in the utricular macula, meaning that they were populated exclusively by identically oriented hair cells (Holley et al., 2010). Numerous hair cells in the *Emx2* KO mice existing as closely apposed pairs were noticed, and a slight delay in the hair cell differentiation was observed, attributing the *Emx2* influence on hair cell polarity to an indirect consequence of progenitor differentiation abnormalities (Holley et al., 2010). Crucially, in 2017 Emx2 was revealed as the hair cell polarity-determining factor (T. Jiang et al., 2017), as explained in the following chapter.

1.4.3.2.1. The role of Emx2 in determining hair cell orientation in neuromasts

The role of *Emx2* in hair cell orientation was first discovered in a genetic study in mice in 2010 (Holley et al., 2010). In zebrafish, genetic manipulation of *emx2* expression produces neuromasts with identically oriented hair cells (T. Jiang et al., 2017). Horizontal neuromasts of the Emx2 loss of function (*emx2* mutant) fish are populated exclusively by rostrally-oriented hair cells, whereas vertical neuromasts consisted of dorsally-oriented hair cells (Y. R. Ji et al., 2018; T. Jiang et al., 2017; Lozano-Ortega et al., 2018). Contrary, misexpression of *emx2* (also referred to as Emx2 gain of function) results in all hair cells oriented in the direction opposite to what is observed upon loss of function, namely in caudad and ventral direction in horizontal and vertical neuromasts, respectively (T. Jiang et al., 2017) (Figure 1.4). Functionally, neuromasts harboring Emx2 gain of function or loss of function are responsive to stimuli only in one direction (T. Jiang et al., 2017).

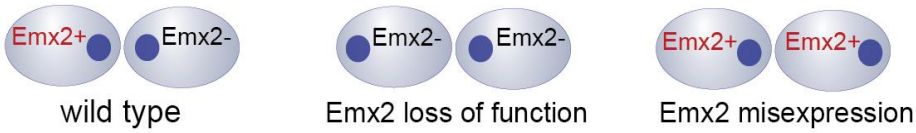

Figure 1.4: Illustration of sibling HCs. Schematic illustration presenting the orientation of hair cell bundles of siblings HC pair in a horizontal neuromast of wild type, Emx2 loss of function (mutant) and Emx2 misexpression (*emx2* overexpression in all HCs) larvae. The Emx2 expression status of each cell is depicted as positive (Emx2+, red) or negative (Emx2-, black). HC – hair cell.

Taken together, Emx2 is necessary and sufficient to determine hair cell orientation in neuromasts (Y. R. Ji et al., 2018; T. Jiang et al., 2017; Lozano-Ortega et al., 2018). Furthermore, in zebrafish neuromasts, Emx2 was detected in caudally-oriented hair cells but not in the rostrally-oriented hair cells (in horizontal neuromasts), and, similarly, Emx2 was detected only in ventrally-oriented hair cells of the vertical neuromasts (T. Jiang et al., 2017). Moreover, the role of *emx2* is evolutionarily conserved in zebrafish, mice, and chickens (T. Jiang et al., 2017).

1.5. Planar cell inversions

Planar cell inversions are cellular rearrangements of sibling neuromast hair cells (Wibowo et al., 2011). They present a fascinating but very poorly understood phenomenon. Planar cell inversions have been observed in zebrafish neuromasts and were first reported a decade ago by Wibowo et al. (2011) and Mirkovic et al. (2012). Interestingly, the planar cell inversions occur in zebrafish neuromasts but do not occur in mice (Deans et al., 2007).

The neuromast hair cells arise in pairs from a division of a unipotent progenitor cell. Soon after the division, the nascent hair cells undergo spatial rearrangements by rotating about an axis through their interface (Wibowo et al., 2011). Consequently, the two nascent sibling hair cells exchange their positions during the process of planar cell inversion (Figure 1.5). The process of planar cell inversions includes the following steps: (I) the initiation step when the two nascent hair cells come close together, and their interface is elongated, (II) The inversion step when the two cells migrate in a circular way and exchange their positions, and (III) the termination of inversion when the cells stop inverting and increase the distance between them (Wibowo et al., 2011).

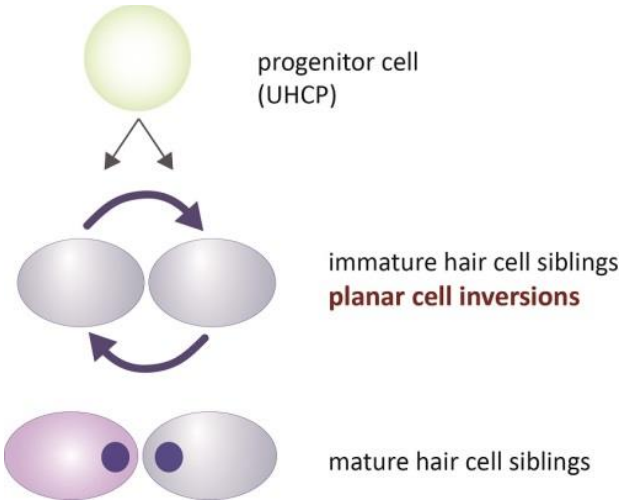

Figure 1.5: Illustration of a PCI. An illustration is presenting the course of planar cell inversion of sibling hair cells. UHCP – unipotent hair cell progenitor.

Interestingly, not all couples of sibling nascent hair cells invert. The non-inverting pairs simply keep their approximate positions after the division of the UHCPs. Distinct, independent studies showed that more than half of the nascent hair cell pairs undergo planar cell inversions. Specifically, Wibowo et al. (2011) reported the planar cell inversions taking place in 60 %, Mirkovic et al. (2012) 71 %, and Navajas Acedo et al. (2019) 60,8 % of the newly produced hair cell pairs. Nevertheless, the non-inverting hair cell pairs also initiate the rearrangements (Mirkovic et al., 2012).

Notably, the link between the planar cell inversions and the planar polarity pathway has been investigated. Specifically, it has been reported that the planar cell inversions take place in *vangl2* mutant larvae (Mirkovic et al., 2012; Navajas Acedo et al., 2019). Interestingly, the hair cell rearrangements in the *vangl2* mutant larvae were reported to last twice as long as in wild-type larvae with higher variability of the inversion duration time (Mirkovic et al., 2012).

To summarize, the planar cell inversions are cellular rearrangements of nascent hair cell pairs occurring in zebrafish neuromasts. So far, little is known about the process of planar cell inversions. Why nascent hair cells undergo planar cell inversion is unknown, and the mechanism of rearrangements remains to be elucidated.

1.6. Overview of zebrafish hair cell transcriptome studies

The transcriptome of zebrafish hair cells has been studied with various approaches. A large number of genes, expressed in neuromast hair cells, has been identified by *in situ* hybridization experiments as well as microarrays and other RNA sequencing techniques (Barta et al., 2018; Erickson & Nicolson, 2015; D. Ji et al., 2015). For instance, to surpass the challenges of the hair cell isolation step, Matern et al. (2018) used an approach including specific tagging of hair cell RNA molecules in combination with immunoprecipitation. However, most studies were focused on the transcriptome of inner ear hair cells and were performed in adult zebrafish (Barta et al., 2018; Erickson & Nicolson, 2015; McDermott et al., 2007). Nevertheless, due to known similarities among vertebrate hair cells, numerous genes detected in the zebrafish inner ear hair cells have been reported as neuromast hair cell-expressed genes as well (Erickson & Nicolson, 2015).

In short, distinct methods have been used to study genes expressed in zebrafish hair cells, and bulk transcriptional RNA sequencing analyses gave us valuable clues about their identity and quantity. Importantly, a recent study included scRNA sequencing analysis of all neuromast cells, including a subset of hair cells (Lush et al., 2019).

1.6.1. Neuromast hair cells marker genes

Marker genes are considered genes with specific or highly enriched expression in distinct tissue- or cell types. Several genes have high expression in neuromast hair cells but not in surrounding support cells. For example, *otofb* (*otoferlin b*) and *anxa5a* (*annexin A5a*) are highly enriched in hair cells but are not expressed in support cells (Erickson & Nicolson, 2015). Moreover, *pvalb8* (*cytosolic calcium buffers parvalbumin 8*), *s100t* (*S100 calcium-binding protein T*), *s100s* (*S100 calcium-binding protein S*), *cabp2b* (*calcium-binding protein 2b*), *chrna9* (*cholinergic receptor, nicotinic, alpha 9a*), *myo6b* (*myosin VIb*) are all highly expressed in neuromast hair cells (Barta et al., 2018; Di Donato et al., 2013; Erickson & Nicolson, 2015; Seiler et al., 2004; Bernard Thisse et al., 2004). Taking into account the highly specialized neuromast hair cell function and structure, it is not surprising that the hair cells express stereocilia-related genes, such as *clrn1* (*clarin 1*) (Ogun & Zallocchi, 2014), *tekt3* (Erickson & Nicolson, 2015; Lush et al., 2019), ion channel *slc17a8* (Erickson & Nicolson,

2015) and genes involved in signal transduction, such as the aforementioned cytosolic calcium buffers *pvalb8*, *s100*t and *s100s* (Erickson & Nicolson, 2015; Lush et al., 2019). Similarly, genes involved in sensory perception of the mechanical stimuli, such as *atp2b1a* (*ATPase plasma membrane Ca2+ transporting 1a*), have been detected in neuromast hair cells using various methods (Barta et al., 2018; Erickson & Nicolson, 2015; B. Thisse et al., 2001). Importantly, *atoh1a* (*atonal bHLH transcription factor 1a*) and delta ligands are known hair cell fate determination factors (Ma et al., 2008). In summary, distinct genes are specifically expressed in neuromast hair cells and can serve as markers of their identity.

1.6.2. Single-cell transcriptional profiling

The details of cellular states, cell-type differences, and developmental lineages can only be studied on a single-cell level. State-of-the-art technologies enable us to gain insights into individual cells and have become indispensable for numerous biological studies (Potter, 2018). The basic principle of single-cell transcriptomics is derived from the possibility of simultaneously performing several hundred or thousands of separate, small-scale amplification reactions. Specifically, a single cell solution is used as the input sample material. Each cell is individually lysed within a well or inside a droplet and, using barcoded oligonucleotides, which can bind to polyadenylated (mature) transcripts; the cellular mRNA pool is reverse-transcribed into cDNA with an incorporated sequence describing molecules' origin. Importantly, barcodes can, in addition to the cell-specific sequence, also include a unique molecular identifier (UMI), used to reduce the amplification bias produced during the amplification step and thus allowing for a more accurate estimation of mRNA abundances. The cDNA libraries are subsequently pooled, amplified by PCR in bulk, and sequenced. Finally, the sequencing data analysis consists of several steps: barcode processing, read mapping (alignment of the reads to the genome), demultiplexing cellular barcodes, and collapsing UMIs (avoiding counting the transcripts, which were better amplified during PCR), and finally discarding low-quality cells and sparse counts. The tools for analyzing the scRNAseq data are still emerging (Y. Wu & Zhang, 2020). The scRNAseq data is often visualized after dimensionality reduction, which is achieved by choosing principal components that disperse the data but retain the relevant data structures (e.g., cell to cell similarities). Cells are then clustered, and the temporal trajectories are analyzed using

pseudotime or RNA velocity (Haghverdi et al., 2016; La Manno et al., 2018; Trapnell et al., 2014). Several methods of single-cell RNA sequencing with individual strong points are currently in continuous development (Choi & Kim, 2019; Papalexi & Satija, 2018; Ziegenhain et al., 2017).

Commercial Chromium kit, developed by 10x Genomics, is widely used for single-cell RNA sequencing (Vieth et al., 2019; Zhang et al., 2019). Molecular crowding SCRBseq (mcSCRBseq) is an improved version of the Single-Cell RNA-Barcoding and Sequencing (SCRBseq) method, a plate-based sequencing method with high accuracy and efficiency but with more limitations on the number of processed cells (Bagnoli et al., 2018).

2. Objectives

Epithelial planar polarity is an essential feature of numerous tissues of multicellular organisms (Butler & Wallingford, 2017; Hale et al., 2015; Zallen, 2007). Epithelial planar bipolarity, the phenomenon of cells being oriented in two opposite directions along a single axis, can only be observed in a small number of biological systems. Specifically, planar bipolarity has been observed in vestibular and lateral line systems, where the polarity of sensory hair cells is oriented in two opposite directions along a single axis (Tarchini & Lu, 2019). Being one of the few exceptions where planar bipolarity can be observed, neuromasts of the zebrafish lateral line are an ideal model to study epithelial planar bipolarity. In addition, neuromast cells can be labeled and easily visualized due to the organ's superficial location. Furthermore, the option to efficiently perform genetic studies as well as long-term live imaging in zebrafish is a great advantage.

The establishment of epithelial planar polarity is a poorly understood phenomenon. The core planar polarity pathway plays a role in cell alignment along an axis, thereby forming a tissue planar polarity (Goodrich & Strutt, 2011). On the contrary, the orientation of individual cells necessitates a cell-intrinsic pathway (Ezan et al., 2013). In order to establish cell planar bipolarity, a symmetry-breaking step is required to produce two populations of cells with opposite orientations. It is currently not known how some cells acquire one orientation, but others acquire the opposite orientation.

Interestingly, it has been shown that cells of one orientation express a polarity-determining transcription factor Emx2, but no expression of Emx2 has been detected in the cells of opposite orientation (T. Jiang et al., 2017). It remains to be investigated how the symmetry in *emx2* expression is broken. Moreover, it has not yet been elucidated when the opposite polarities of the two populations of sensory hair cells arise.

In my doctoral thesis, I investigated the establishment of epithelial planar bipolarity in zebrafish neuromasts. I aimed to shed light on the symmetry-breaking event and find out when the neuromast hair cells of opposite polarities become different and whether there are any major transcriptional differences between them. To this end, I set out to investigate the spatiotemporal expression of *emx2*, the hair cell polarity-determining factor. Moreover, I wanted to address the question of how emx2 gets expressed in only one of the sibling hair

cells. Since the single-cell transcriptional analysis suggested it a likely candidate, I focused on determining the role of *notch1a* in the establishment of the bipolar planar epithelium. In particular, I wanted to reveal the relationship between *emx2* and *notch1a* during orientation determination, using pharmacological manipulations of the Notch signaling pathway, genetic manipulations, and protein visualization techniques. Finally, my last goal was to determine if the cellular rearrangements, called planar cell inversions, are critical patterning steps in establishing planar bipolarity in neuromasts. To investigate this, I aimed to acquire new knowledge about the planar cell inversions by characterizing the process and comparing the dynamics of planar cell inversions in wild type and *emx2* mutant larvae.

In summary, epithelial planar bipolarity is a rare and poorly understood phenomenon. Neuromasts of the zebrafish lateral line are the ideal model to study the epithelial planar bipolarity. The goal of my doctoral thesis project was to shed light on its establishment. Combining the single-cell transcriptional analysis with advanced imaging techniques and genetic manipulations, I aimed to improve our knowledge about the symmetry-breaking event that leads to epithelial planar bipolarity.

3. Materials

Overview of materials used in this thesis.

3. 1. Zebrafish lines, used in this thesis

Ethics statement

Experiments with zebrafish embryos were conducted under the protocol number Gz.:55.2-1-54- 2532- 202-2014 approved by the “Regierung von Oberbayern,” Germany.

Zebrafish lines used in this thesis are summarized in Table 3.1. Additionally, the zebrafish larvae studied in this thesis are listed below.

Table 3.1: Zebrafish lines.

Zebrafish line	**Referred to as**	**Reference**
AB wild type, Tübingen background	wild type	/
ET(krt4:EGFP)SqGw57a	Gw57a	(Kondrychyn et al., 2011)
Tg[myo6b:actb1-EGFP]	myo6b:GFP	(Kindt et al., 2012)
Tg(pou4f3:GAL4)	brn3c:gal4	(Xiao & Baier, 2007)
Tg(UAS:Notch1a-intra)	UAS:NICD	(Scheer & Campos-Ortega, 1999)
emx2 mutant (Chr13:idc5), Tg[myo6b:actb1-EGFP]	emx2 mutant, myo6b:GFP	(T. Jiang et al., 2017)
atoh1a mutant line	atoh1a mutant	(Pujol-Martí et al., 2014)
Tg[-8.0cldnb:Lyn-EGFP]	cldnb:GFP	(Haas & Gilmour, 2006)

notch1a mutant	notch1a mutant	this thesis (Kozak et al., 2020)
Tg(alpl:nlsEGFP)	alpl:nlsEGFP	this thesis (Kozak et al., 2020)
Tg(myo6b:Gal4VP16-pA)	myo6b:gal4	this thesis (Kozak et al., 2020)
Tg(alpl:nlsEGFP), Tg[myo6b:actb1-EGFP]	alpl:nlsEGFP, myo6b:GFP	this thesis

(E)GFP – green fluorescent protein

Importantly, all live experiments were performed in larvae of up to 5 days post fertilization (dpf). The list of zebrafish larvae used in this thesis and generated by crossing the above-listed transgenic and mutant lines or somatic mutagenesis follows below.

Zebrafish larvae used in this thesis:

- Tg(pou4f3:GAL4), Tg(UAS:Notch1a-intra)
- Tg(myo6b:Gal4VP16-pA), Tg(UAS:Notch1a-intra)
- Tg[-8.0cldnb:Lyn-EGFP], Tg[myo6b:actb1-EGFP]
- Tg(alpl:nlsEGFP), Tg[myo6b:actb1-EGFP]
- Tg[myo6b:actb1-EGFP]
- *emx2* mutant (Chr13:idc5) (hom), Tg[myo6b:actb1-EGFP]
- *emx2* mutant (Chr13:idc5) (hom), *notch1a* mutant (hom), Tg[myo6b:actb1-EGFP]
- *notch1a* mutant (hom), Tg[myo6b:actb1-EGFP]
- *atoh1a* mutant (hom)

3. 2. Bacterial strains

Bacterial strains used in this thesis are summarized in Table 3.2.

Table 3.2: Bacterial strains.

Bacterial strain	**Manufacturer**	**Catalog number**
Subcloning Efficiency™ DH5α Competent Cells	Thermo Fischer	18265017
One Shot™ TOP10 Chemically Competent *E. coli*	Invitrogen	C404003

3. 3. Chemicals, general reagents, recombinant proteins, and antibodies

Chemicals and reagents, including recombinant proteins and antibodies used in this thesis, are summarized in Table 3.3.

Table 3.3: Chemicals, reagents, and recombinant proteins.

Compound	**Manufacturer**	**Catalog number**
2-mercaptoethanol	Sigma-Aldrich	M6250
DiAsp (4-(4-diethylaminostyryl)-1-methylpyridinium iodide)	Sigma-Aldrich	D3418
7-AAD (7-amino-actinomycin D)	BD	BDB559925
10x Dream Taq Buffer	Thermo Scientific	B65
Ab: Rabbit anti Emx2	Trans Genic	KO609
Ab: Goat anti rabbit Alexa Fluor-594	Abcam	ab150080
Accumax	Sigma-Aldrich	A7089
Accutase	Sigma-Aldrich	A6964
Acetone	Merck	100014

Agarose LE	Lonza	50004
Alexa Fluor™ 488 Phalloidin	Thermo Fischer	A12379
Ampicillin sodium salt	Sigma-Aldrich	A8351
Bacteriological Agar	Sigma-Aldrich	A5306
Bacto Tryptone	Gibco	211705
BSA (Bovine Serum Albumin solution)	Sigma-Aldrich	A1595
Biozym Phor Agarose	Biozym Scientific GmbH	850180
$CaCl_2$	Sigma-Aldrich	499609
Cas9 protein	Sigma-Aldrich	CAS9PROT
DAPI (4',6-diamidino-2-phenylindole)	Sigma-Aldrich	1.24653
DAPT (N-[N-(3,5-difluorophenacetyl)-L-alanyl]-S-phenylglycine-t-butyl ester)	Sigma-Aldrich	565770
Dimethylsulfoxid (DMSO)	Sigma-Aldrich	D2650
Dream Taq polymerase	Thermo Fischer	EP0702
FastDigest Green Puffer (10x)	Thermo Fischer	B72
FastDigest ApaLI (restriction enzyme)	Thermo Fischer	FD0505
FastDigest PvuI (restriction enzyme)	Thermo Fischer	FD0634
GeneRuler DNA Ladder Mix	Thermo Fischer	SM0331
Glycerol	Sigma-Aldrich	G6279
Guanidine hydrochloride	Sigma-Aldrich	G3272
EDTA ((Ethylenedinitrilo)tetraacetic acid)	Sigma-Aldrich	1233508
Ethanol	J. T. Baker	8025
Fetal Bovine Serum (FBS)	Sigma-Aldrich	F9665

HEPES	Sigma-Aldrich	H3375
Isopropanol	Merck	109634
Kanamycin	Sigma-Aldrich	K0254
KCl	Sigma-Aldrich	P9541
Low-melting point agarose	Lonza	50104
MgSO4	Sigma-Aldrich	M7506
NaCl	Sigma-Aldrich	S7653
NotI (restriction enzyme)	Thermo Scientific	ER0591
MS-222 (Tricaine, Powder for Solution for Fish Treatment)	PharmaQ	CRN000V55
Pierce™ Lysozym	Thermo Scientific	89833
Paraformaldehyde 16% w/v Solution	Alfa Aesar	AA433689M
PCR Nucleotide Mix	Thermo Scientific	R0191
Phalloidin Alexa Fluor™ 488	Invitrogen	A12379
RNAse A	Thermo Scientific	EN0531
Sheep serum	Sigma-Aldrich	S3772
SOC medium	Invitrogen	15544034
Sucrose	Sigma-Aldrich	S9378
Tartrazine	Sigma-Aldrich	T0388
TE buffer	Thermo Scientific	12090015
Tris	Carl Roth GmbH	5429.3
Trypan Blue Stain (0.4 %)	Thermo Scientific	15250061
Tween-20	Sigma	P1379

Yeast extract	Carl Roth	2363

Ingredients of buffers and media used in this thesis are listed below.

Solutions, buffers, and media

- Danieau's solution

  5 mM NaCl, 0.17 mM KCl, 0.33 mM $CaCl_2$, 0.33 mM $MgSO_4$; pH=7.2

- Blocking solution

  1.5% sheep serum, 1.5% BSA in PBST

- Easy buffer

  10 mM Tris-HCl pH = 8, 1 mM EDTA, 15% w/v sucrose, 2 mg/mL lysozyme, 0.2 mg/mL RNAse A, 0.1 mg/mL BSA, 0.1mM tartrazine

- LB medium

  10g/L Bacto-Tryptone, 5 g/L Yeast extract 10 g/L NaCl, pH=7

- LB agar

  10g/L Bacto-Tryptone, 5 g/L Yeast extract, 10 g/L NaCl, 13 g/L agar

- MS-222

  The stock solution of MS-222 (4g/L), pH=7 adjusted with 1M Tris (pH=9), stored at 20°C.

  MS-222 was used at a final concentration of 0.16 g/L in Danieau's solution. During the live video microscopy, the MS-222 concentration was 0.08 g/L.

- PBS(T)

  137 mM NaCl, 2.7 mM KCl, 10 mM Na_2HPO_4, 1.8 mM KH_2PO_4; pH=7.4, (0,5% tween)

- Ringer's solution

116 mM NaCl, 2.6 mM KCl, 1.8 mM $CaCl_2$, 5 mM HEPES; pH=7

- Sort buffer

  116 mM NaCl, 2.6 mM KCl, 5 mM HEPES, 2 mM EDTA, 10% FBS; pH=7

- TAE buffer

  40 mM Tris, 20 mM Acetic acid, 1 mM EDTA

3. 4. Commercial kits

The kits used in this thesis are listed in Table 3.4.

Table 3.4: Commercial kits.

Commercial kits	**Manufacturer**	**Catalog number**
AccuPrime™ *Pfx* SuperMix	Thermo Fischer	12344040
Ambion mMessage mMachine SP6 Kit	Thermo Fischer	AM1340
Gateway™ BP Clonase™ II Enzyme mix	Invitrogen	11789100
Gateway™ LR Clonase™ II Enzyme mix	Invitrogen	11791100
MEGAshortscript™ T7 Transcription Kit	Thermo Fischer	AM1354
QIAquick Gel Extraction Kit	QIAGEN	28704
Qiagen RNeasy Mini Kit	QIAGEN	74104
QIAprep Spin Miniprep Kit	QIAGEN	27106
Single Cell 3’ Library and Gel Bead Kit v2	10x Genomics	PN-120237

3. 5. Plasmids, DNA oligonucleotides, and RNA molecules

Plasmids generated and used in this thesis are listed in Table 3.5:

Table 3.5: Plasmids.

Plasmid	**Source**
myo6b:Gal4VP16-pA	Kindt lab
pAIP-5kbmCherrySV40polyA	Stenier lab
p5E-alpl	this thesis (Kozak et al., 2020)
pME-nlsEGFP (pEM 385)	Tol2 kit
p3E-polyA (pE3´302)	Tol2 kit
alpl:nlsEGFP	this thesis (Kozak et al., 2020)
pDONRP4-P1R vector	Invitrogen
pCS2FA-transposase	Tol2 kit

The oligonucleotides used in this thesis are listed in Table 3.6. The oligonucleotides were synthesized and purchased from Sigma-Aldrich.

Table 3.6: Oligonucleotides.

Name	**Sequence 5' -> 3'**
5E_p-alpl_F	GGGGACAACTTTGTATAGAAAAGTTGCGCCCACTTTGGCATAATCTTGC
5E_p-alpl_R	GGGGACTGCTTTTTTGTACAAACTTGCAGCGCTGGAAGAACAGACTC
sgRNAs_general_ core	AAAGCACCGACTCGGTGCCACTTTTTCAAGTTGATAACGGACTAGCCTTA TTTTAACTTGCTATTTCTAGCTCTAAAAC
P_sgRNA_*emx2*_1	TAATACGACTCACTATAGGTAAAACACCTCTTCGGTGTTTTAGAGCTAGA AATAGC
P_sgRNA_*emx2*_2	TAATACGACTCACTATAGGACTGTGCGAAGACGACAGTTTTAGAGCTAG AAATAGC

P_sgRNA_*emx2*_3	TAATACGACTCACTATAGGCTTTTCGCAAGCCAGCAATTTTAGAGCTAGA AATAGC
P_sgRNA_*emx2*_4	TAATACGACTCACTATAGGTGAGTTTCTGTGAGGCTATTTTAGAGCTAG AAATAGC
P_sgRNA_*wdpcp*_1	TAATACGACTCACTATAGGGCATCACGCAGCTTCTCT GTTTTAGAGCTAGAAATAGC
P_sgRNA_*wdpcp*_2	TAATACGACTCACTATAGGTCCAGTGGTTTTCTCAGC GTTTTAGAGCTAGAAATAGC
P_sgRNA_*wdpcp*_3	TAATACGACTCACTATAGGCTGGAGCCTACAGAGCCA GTTTTAGAGCTAGAAATAGC
P_sgRNA_*wdpcp*_4	TAATACGACTCACTATAGGTCTGGGCGACGGTTACTAGTTTTAGAGCTA GAAATAGC
P_sgRNA_*hmx2*_1	TAATACGACTCACTATAGGATCGTGAAACTTGAAATGGTTTTAGAGCTA GAAATAGC
P_sgRNA_*hmx2*_2	TAATACGACTCACTATAGGACCGGACTCCGTCGTTTGGTTTTAGAGCTA GAAATAGC
P_sgRNA_*hmx2*_3	TAATACGACTCACTATAGGTCTCCGTTAACTGCAGGCGTTTTAGAGCTAG AAATAGC
P_sgRNA_*hmx2*_4	TAATACGACTCACTATAGGAGGCGAGACAGGCTCTCTGTTTTAGAGCTA GAAATAGC

sgRNAs and mRNA synthesized and used in this thesis are listed in Table 3.7.

Table 3.7: sgRNAs and mRNA.

RNA molecule type	**Gene / Target gene**
short guide RNA	*emx2* (4 sgRNAs), *wdpcp* (4 sgRNAs), *hmx2* (4 sgRNAs)

mRNA	transposase

3. 6. Datasets

Datasets generated and analyzed in this thesis are listed in Table 3.8:

Table 3.8: Datasets generated and analyzed in this thesis.

Dataset	Reference	GEO accession number
Single-cell RNAseq data (10x Chromium)	this thesis (Kozak et al., 2020)	GEO: GSE144827
Single-cell RNAseq data (mcSCRBseq)	this thesis (Kozak et al., 2020)	GEO: GSE143663

3. 7. Software

The software used in this thesis is listed in Table 3.9:

Table 3.9: Software

Software	Reference / Publisher	Website
Adobe Illustrator CS6 (trial version)	Adobe	https://www.adobe.com/
ApE	Wayne Davis, University of Utah	https://jorgensen.biology.utah.edu/wayned/ape/
CCTop - CRISPR/Cas9 target online predictor	(Stemmer et al., 2015)	https://crispr.cos.uni-heidelberg.de/
CRISPRater	(Labuhn et al., 2018)	https://crispr.cos.uni-heidelberg.de/

Fiji	(Schindelin et al., 2012)	https://imagej.nih.gov/ij/
ggplot2 (R package)	(Wickham, 2016)	https://ggplot2.tidyverse.org
Gprofiler (v1.0.0)	(Raudvere et al., 2019)	https://pypi.org/project/gprofigpr-official/
Mendeley	Mendeley	https://www.mendeley.com/?interaction_required=true
MTrackJ (Fiji plugin)	(Meijering et al., 2012)	https://imagescience.org/meijering/software/mtrackj/
Python (3.7)	(Python Software Foundation, 2009)	https://www.python.org/
R (3.5.0) and (4.0.2)	(R Core Team, 2020)	https://www.r-project.org/
Rstudio (1.0.143)	(RStudio Team, 2016)	http://www.rstudio.com/
Scanpy (v1.4.3)	(Wolf et al., 2018)	https://scanpy.readthedocs.io/en/stable/
Scrublet (v0.2.1)	(Wolock et al., 2019)	https://github.com/AllonKleinLab/scrublet
SnapGene	GSL Biotech LLC	https://www.snapgene.com/
Tissue Analyzer (Fiji plugin)	(Aigouy et al., 2016)	https://grr.gred-clermont.fr/labmirouse/software/WebPA/

3. 8. Laboratory equipment

Equipment used in this thesis is listed in Table 3.10:

Table 3.10: Equipment.

Equipment	**Company**
Centrifuge 5415R	Eppendorf
FACS Aria	BD
Freezer Medline, -20°C	Liebherr
Fridge, +4°C	Liebherr
HiSeq4000	Illumina
Incubator Refrigerated Shaker Innova 4230	New Brunswick Scientific
Incubator Memmert BM 600	Memmert
Injector FemtoJet	Eppendorf
Mastercycler gradient	Eppendorf
Microwave	Severin
Micropipette puller PC-10	Narishige
Nanodrop ND-1000 Spectrophotometer	NanoDrop
pH-meter	Inolab
Research pipettes (0.2-2µL,2-20µL, 10-100 µL, 100- 1000µL)	Eppendorf
Scale	Sartorius
Shaker Polymax 1040	Heidolph
Spinning disc, inverted, custom-built (Zeiss Axioscope) microscope	Zeiss

Stemi SV11 Microscope	Zeiss
Stereomicorscope Lumar V12	Zeiss
Thermomixer Comfort	Eppendorf
(Vortex) MS Minishaker	IKA
Ultraviolet lamp for gel analysis	Konrad Benda Laborgeräte

4. Methods

4.1. Cloning

4.1.1. The polymerase chain reaction

The polymerase chain reaction (PCR) was used to amplify the 5 kb (4575 bp) *alpl* promoter from the *alpl* promoter template, a gift from Steiner lab (Steiner et al., 2014). Specifically, I used the AccuPrime Pfx polymerase (Invitrogen) and primers with overhangs to add att sites:

- GGGGACAACTTTGTATAGAAAAGTTGCGCCCACTTTGGCATAATCTTGC,
- GGGGACTGCTTTTTTGTACAAACTTGCAGCGCTGGAAGAACAGACTC.

The program used for PCR reaction for amplification of *alpl* promoter is summarized in Table 4.1.

Table 4.1: Program of the Thermal Cycler used for PCR reaction for DNA amplification.

Step	**Temperature**	**Duration**	**Repetition**
initial denaturation	95°C	5 min	1x
denaturation	95°C	30 s	30x
annealing	60° C	45 s	30x
elongation	68° C	7 min	30x
final elongation	68° C	10 min	1x
storage	4° C	∞	1x

The PCR product was inspected and cleaned with AGE using 0.8 % agarose gel. The alpl promoter PCR product was extracted from the agarose gel with QIAquick Gel Extraction Kit.

4.1.2. Gateway/Tol2 transposition system cloning reactions

- Gateway BP reaction was used to ligate the alpl-promoter PCR fragment into pDONRP4-P1R vector using the BP clonase kit (Gateway™ BP Clonase™ II Enzyme

mix), following the manufacturer's instructions. Briefly, 1 µL the insert (PCR-product) with concentration 50 fmol/µL and 1 µL of pDonor 5' plasmid with concentration 50 fmol/µL were added to 6 µL of TE buffer. Finally, 2 µL of BP clonase was added to the reaction.

- Gateway LR reaction was used to ligate the p5E-alpl, pME-nlsEGFP, p3E-polyA plasmids into the pDestTol2pA using the LR clonase kit (Gateway™ LR Clonase™ II Enzyme mix), following the manufacturer's instructions. Briefly, 1 µL each plasmid (pDestTol2pA, p5E-alpl, pME-nlsEGFP, p3E-polyA) with concentration 20 fmol/µL were added to 4 µL of TE buffer. Finally, 2 µL of LR clonase was added to the reaction.

The Gateway BP and LR reactions were incubated at 25°C o/n. Next, the treatment with proteinase K (1 µL added to the total reaction mix) for 15 min at 37°C took place. Finally, the reaction mixture was used to transform competent *E. coli* cells.

4.1.3. Transformation of competent *E. coli*

Transformation of competent *E. coli* was used to amplify plasmids.

To this end, the competent cells were thawed on ice, and 5 µL of the reaction mix (after LR/BP reaction) was added to the cells. 10 min incubation on ice was followed by a heat shock at 42°C for 45 s and additional 2 min incubation on ice. Next, 400 µL of SOC medium was added to the transformed bacteria and shacked at 300 rpm for 1 h at 37°C. The transformed bacteria were plated on LB agar plates with a selection marker (100 µg/mL ampicillin or 50 µg/mL kanamycin) and incubated o/n at 37°C.

- For amplification of p5E-alpl plasmid after the BP reaction, the DH5α competent *E. coli* cells were transformed and plated on kanamycin agar plates o/n.
- For the amplification of alpl:nlsEGFP plasmid after the LR reaction, the One-shot Top10 *E. coli* cells were transformed and plated on ampicillin agar plates o/n.

The next day, several colonies were picked for the production of over-nigh cultures.

4.1.4. Identification of colonies containing the correct plasmid

The identification of colonies containing the correct plasmid was achieved by restriction analysis. First, following the Gateway LR reaction transformation, the colonies were inspected visually, and only the clear colonies were identified to potentially contain the correct plasmid. Nevertheless, several colonies were picked from agar plate to inoculate the LB medium with a selection marker (100 µg/mL ampicillin or 50 µg/mL kanamycin) and incubated o/n at 37°C in the incubator (200 rpm shaking). Second, 20 % of the overnight cultures were used for Easyprep isolation. To this end, the bacteria from 1.5 mL of overnight culture were pelleted by centrifugation at 6000 rpm for 3 min in a tabletop centrifuge. 50 µL of Easy buffer was added, and the bacteria and, after resuspension, incubated for 1 min at 99°C. A 5 min incubation at room temperature and then a 15 min centrifugation at >8000 rpm followed. Third, the restriction reaction was set as follows: 15 µL Easyprep mixture, 7 µL H_20, 2.5 µL restriction buffer, and 0.5 µL restriction enzyme. The restriction reaction took 1 h, and the size of DNA fragments was directly inspected by AGE. In particular, the colonies containing alpl:nlsEGFP clone were identified by confirming correct fragment size by two separate restriction analyses with ApaLI (resulting in fragments of 8598 bp and 1246 bp) and PvuI (resulting in fragments of 6299 bp and 3545 bp). Restriction of pDestTol2pA plasmid was used as control.

4.1.5. Plasmid isolation

Plasmids were isolated from overnight cultures prepared as described above. The bacteria were pelleted by centrifugation at 6000 rpm for 3 min. Next, the plasmids were isolated with QIAprep Spin Miniprep Kit, following the manufacturer's instructions. Finally, the yield was measured on Nanodrop.

4.1.6. DNA Sequencing

The cloned DNA plasmids were sequenced by Eurofins Genomics company (the Supreme Run Tube Custom DNA sequencing offer). The sequencing results were inspected with ApE or SnapGene programs.

4.1.7. mRNA synthesis

mRNA for injections into zebrafish embryos was transcribed *in vitro*. In particular, transposase mRNA was transcribed *in vitro* from the pCS2FA-transposase plasmid. Briefly, the pCS2FA-transposase plasmid was first linearized with NotI, and the restriction reaction was quenched with a solution containing 0,5 µL of 0,5 M EDTA, 1 µL 3 M Na-acetate and 20 µL ethanol and cooled at -20ºC for 30 min. Next, a 15-min centrifugation step and removal of supernatant took place, and the linearized plasmid was diluted in water. 1 µ of the linearized plasmid was used as the template for *in vitro* transcription using the Ambion mMessage mMachine SP6 Kit Transcription Kit, following the manufacturer's instructions. The transposase mRNA was purified using ethanol precipitation as described in the protocol. Finally, the yield was measured by Nanodrop, and the RNA integrity was verified by AGE.

4.1.8. sgRNA synthesis

The short guide RNAs were synthesized in three steps: design, template generation, and in vitro transcription, as described in the following paragraphs.

4.1.8.1. sgRNA design

First, the sgRNAs were designed using the CCTop - CRISPR/Cas9 target online predictor (Stemmer et al., 2015). From the sgRNAs predicted with CCTop, the sgRNAs were selected based on the following criteria:

- no possible off-target binding sequences, or with a maximum available number of mismatching nucleotides, preferably in the non-coding region,
- their target site location (close downstream of the gene start codon),
- their suitability for *in vitro* transcription (target site 5' limitation: desired GG),
- no single nucleotide polymorphism (SNP) sites in the target region,
- targeting of several transcripts if existing,
- high efficiency as predicted by CRISPRater (Labuhn et al., 2018),
- when using the redundant gene-targeting approach, the sgRNAs, binding to non-

overlapping regions, were given priority (R. S. Wu et al., 2018).

The following crRNAs were selected:

- targeting *emx2*: GGTAAAACACCTCTTCGGTG, GGACTGTGCGAAGACGACAG, CTCTTTTCGCAAGCCAGCAA, CCTGAGTTTCTGTGAGGCTA
- targeting *wdpcp*: GGGCATCACGCAGCTTCTCT, GGTCCAGTGGTTTTCTCAGC, GGCTGGAGCCTACAGAGCCA, TCTCTGGGCGACGGTTACTA
- targeting *hmx2*: GGATCGTGAAACTTGAAATG, CGACCGGACTCCGTCGTTTG, TGTCTCCGTTAACTGCAGGC, GGAGGCGAGACAGGCTCTCT

4.1.8.2. Template for sgRNA generation

Next, the templates for *in vitro* transcription were generated by annealing the general primer with the sgRNA primer as described previously (Varshney et al., 2015).

For each sgRNA, a sgRNA-target oligonucleotide composed of the T7 promoter sequence (TAATACGACTCACTATA), GG, specific sgRNA (without PAM), and a sequence complementary to the general primer (sgRNAs_general_core, TTTTAGAGCTAGAAATAGC) was designed.

- General primer (sgRNAs_general_core) tracrRNA sequence:

AAAAGCACCGACTCGGTGCCACTTTTTCAAGTTGATAACGGACTAGCCTTATTTTAACTTGCTATTTCTAGCTCTAAAAC

The underlined sequence of the general primer anneals to the sgRNA-specific target oligonucleotide. The template was generated with annealing and elongation of general (sgRNAs_general_core) and sgRNA-specific target oligonucleotide. Specifically, 8 µL of sgRNA-specific target oligonucleotide (or an equimolar mixture of 4 oligonucleotides targeting the same gene), 8 µL of general primer (sgRNAs_general_core), 2 µL of 10x Dream Taq Buffer, 1.7 µL dNTP mix 2mM, and 0.3 µL Dream Taq polymerase were mixed in a PCR-tube. A thermocycler was used for annealing and elongation, running one cycle with the program described in Table 4.2:

Table 4.2: sgRNA template generation program.

Step	Temperature	Duration
denaturation	98° C	2 min
annealing	50° C	10 min
elongation	72° C	10 min

After the template generation, 2µL of the product was inspected with AGE using 2.5% agarose gel, and 2 µL was used as the template for in vitro transcription.

4.1.8.3. sgRNA *in vitro* transcription

The in vitro transcription of sgRNAs was performed with MEGAshortscript™ T7 Transcription Kit, following the manufacturer's instructions with reaction taking place at 37ºC for 4 h. sgRNAs were purified using ethanol precipitation and inspected with AGE using 2.5% agarose gel. Finally, the sgRNAs were prepared for injections.

4.1.9. Ribonucleoprotein solution preparation

Cas9-sgRNA ribonucleoproteins (RNPs) were produced *in vitro* prior to injections, as described in Table 4.3.

Table 4.3: RNP injection mix assembly composition.

Compound	Concentration
Cas9 protein	15 µL
KCl	300 mM
sgRNAs	1 µg/µL

To generate the RNP was the injection mix was set and incubated at 37ºC for 5 min just

before the microinjections.

4.2. Zebrafish lines and husbandry

Zebrafish embryos and larvae were kept under standardized conditions at 28.5°C in the 0,3 x Danieau's solution (5 mM NaCl, 0.17 mM KCl, 0.33 mM $CaCl_2$, 0.33 mM $MgSO_4$; pH adjusted to 7.2). E-5 % (w/v) Methylene Blue was added as an antifungal agent. The maximum density of larvae was 50 larvae per 85-mm Petri dish.

The zebrafish lines used in this thesis are described in Table 4.4. For the Ethics statement, please see chapter 3. 1.

Table 4.4: Zebrafish lines and comments.

Zebrafish line	**Comments**	**Reference**
ET(krt4:EGFP)SqGw57a	Transgenic line with an enhancer trap of minimal promoter krt4 driving expression of EGFP. Green fluorescence visible in neuromast support cells.	(Sieger et al., 2003)
Tg[myo6b:actb1-EGFP]	Transgenic line expressing actb1-EGFP in HCs (and UHCPs). Visible hair bundles and their orientation.	(Kindt et al., 2012)
Tg(pou4f3:GAL4)	Transgenic line expressing Gal4 in HCs.	(Xiao & Baier, 2007)
Tg(UAS:Notch1a-intra)	Transgenic line, expressing NICD when combined with Gal4-expressing line.	(Scheer & Campos-Ortega, 1999)
emx2 mutant (Chr13:idc5), Tg[myo6b:actb1-EGFP]	*emx2* mutant line (HCs with rostrad orientation). Transgenic line expressing actb1-EGFP in HCs (and UHCPs). Visible hair bundles and their orientation.	(T. Jiang et al., 2017)

atoh1a mutant	*atoh1a* mutant line (no HCs produced)	(Pujol-Martí et al., 2014)
Tg[-8.0cldnb:Lyn-EGFP]	Transgenic line with 8 kb cldnb promoter driving expression of EGFP. Green fluorescence visible membranes of lateral line cells.	(Haas & Gilmour, 2006)
notch1a mutant	*notch1a* mutant line (HCs with caudad orientation)	(Kozak et al., 2020)
Tg(alpl:nlsEGFP)	Transgenic line with 5 kb *alpl* promoter driving expression of nuclear EGFP. Green fluorescence visible in neuromast cells.	this thesis (Kozak et al., 2020)
Tg(myo6b:Gal4VP16-pA)	Transgenic line expressing Gal4 in HCs and UHCPs.	this thesis (Kozak et al., 2020)

4.3.1. Identification of transgenic larvae

For the selection of larvae expressing the green fluorescent protein in all transgenic lines, a Stereomicorscope Lumar V12 was used. In Table 4.5, the probable phenotypes of transgenic fish according to the Mendelian ratio are summarized. During the screening, the larvae were under anesthesia in 0.3x Danieau's solution with 0.16 g/L MS-222.

Table 4.5: Overview of the probable genotypes of transgenic fish.

The variation between the weak or strong expression of the transgene is not differentiated.

Cross	**Phenotype**
wt x het	50% positive, 50% negative
wt x hom	100% positive

het x het	75% positive, 25% negative
het x hom	100% positive
hom x hom	100% positive

wt – wild type, hom – homozygous, het – heterozygous

4.3.2. Identification of mutant larvae

The homozygous mutant larvae were identified visually. In Table 4.6, the probable genotypes of mutant fish according to the Mendelian ratio and the observed phenotypes are summarized for a cross of two heterozygous mutant fish. The observed phenotype percentages correspond to phenotypes caused by a homozygous gene mutation.

Table 4.6: Overview of the probable genotypes of mutant fish

Genotype **cross: het mut x het mut**	**Observed phenotype** **cross: het mut x het mut**
25% wt	wt
50% het mut	wt
25% hom mut	mut

wt – wild type, mut – mutant, hom – homozygous, het – heterozygous

Identifications of *notch1a*, *emx2*, and *atoh1a* mutant larvae:

- The homozygous *notch1a* mutant larvae were identified by disordered somites phenotype (Gray et al., 2001), using a light-microscope (Stemi SV11 Microscope).
- The homozygous *emx2* mutant larvae were identified in myo6b:GFP transgenic background by observing the orientation of their neuromast hair cells using a custom-built inverted spinning-disc microscope (Zeiss Axioscope).

- The *atoh1a* homozygous mutant larvae were identified by their absence of neuromast hair cells. In particular, the larvae were stained with DiAsp dye and observed using a fluorescent microscope. The larvae without signal in neuromast hair cells were identified as *atoh1a* mutants.

4.3.2.1. DiAsp staining

To visualize the hair cells, when screening the atoh1a mutant larvae, the hair cells of live larvae were stained with vital dye DiAsp (4-(4-diethylaminostyryl)-1-methylpyridinium iodide). The stock solution of 5mM DiAsp in DMSO (dimethylsulfoxide) was prepared in advance and stored at 4°C. For the hair cell labeling, the larvae were incubated in 5 µM DiAsp in 0.3 x Danieau solution for 5 min in the dark, at room temperature. Afterward, the larvae were washed and kept protected from light.

4.3.3. Embryo chorion removal

The embryos were left to hatch naturally. If embryos younger than 3 dpf were analyzed, they were dechorionated manually by a pair of forceps.

4.4. Single-cell embryo microinjections

The injections into single-cell embryos were used for somatic mutagenesis with CRISPR/Cas9 redundant targeting of single-gene approach and zebrafish line generation. The embryos were injected at room temperature using a micro FemtoJet injector. The injection tray, namely agarose gel with linear grooves, was generated in advance by pouring hot 1.5% agarose gel in a Petri dish and placing a plastic mold on top of the gel. The injection trays were stored at 4°C for a maximum of two weeks and were warmed before the injections.

For the microinjections, the zebrafish eggs were collected and washed with 0.3 x Danieau solutions. Next, the eggs were placed on the agarose gel with linear grooves bathed in the 0.3 x Danieau solutions. The eggs were gently pushed into depressions and positioned in the same orientation using a pipette tip. Critically, the injection solution was then transferred into the injection needle. For this purpose, the injection needle was produced with a

micropipette puller by location-specific heating to 85°C and simultaneous pulling of a glass capillary resulting in an elongated closed end of the capillary. Then, the injection needle containing the injection solution was placed into the injector, and the closed end of the injection needle was broken with forceps to produce a small hole.

Finally, 1 nL (volume estimated from droplet size) of injection solution was injected into one-cell-stage embryos using under a bright field light microscope (Stemi SV11 Microscope) using a microinjector (FemtoJet). Specifically, for line generation, the embryos were injected into the cell (Figure 4.1). Contrary, for somatic mutagenesis, the embryos were injected into the yolk. Finally, the injected embryos were washed from the injection tray and grown in the 0.3 x Danieau solution at 28.5°C. The injected embryos are called F0 generation; the generations' nomenclature is explained in Table 4.7. The non-injected embryos were used for control in all experiments.

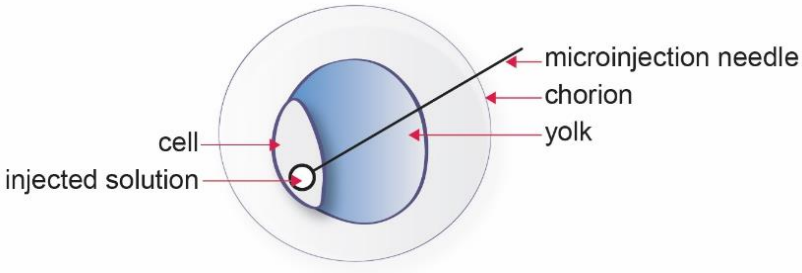

Figure 4.1: Illustration of microinjection. An illustration of microinjection into the one-cell stage zebrafish embryo. Note that the injection needle enters into the cell through the yolk and exits following the same path.

Table 4.7: Overview of zebrafish generation nomenclature.

Generation	Comments
F0	fish generated with injections or crossing resulting in new transgenic/mutant line
F1	first-generation (outcross of F0)

F3	second-generation (outcross of F1)
...	

4.5. Transgenic line generation using the Tol2 system

The Tol2 system is commonly used to generate transgenic lines (Kawakami & Noda, 2004; Kwan et al., 2007). The method is based on introducing transgenic DNA into the zebrafish genome by the transposase. Tol2 system takes advantage of three-insert multisite Gateway cloning (att4-att1-att2-att3) from Invitrogen. The Gateway BP reactions are used to produce three plasmids: p5'E, pME, and p3'E, usually containing the promoter or enhancer (p5'E), reporter or gene of interest, or N-fusion domain (pME), and polyadenylation (polyA) signal, reporter or C-fusion domain (p3'E). The three plasmids (p3'E, pME, p5'E) are cloned into a backbone plasmid with Gateway LR reaction. Notably, the backbone plasmid contains transposon ends (Tol2 terminal inverted repeats) recognizable by the transposase.

Additionally, the backbone contains polyA signal and optionally a sequence encoding elements for expression of a marker gene outside the tissue of interest (heart or eye lenses) to facilitate identification of carrier fish. The plasmid containing the transgenic sequence with short tol2 sites on each side and transposase mRNA are injected into the first cell of the embryo. The transgenic sequence is integrated into the genome at a random location. The location of integration can impact the expression pattern of the transgene. Furthermore, the injected fish (F0) are potentially mosaic, and a fish carrying the transgenic sequence in germ cells needs to be identified by screening the progeny of the injected fish (F1). Importantly, in order to generate a stable transgenic line, another outcross is required because the construct is potentially duplicated (even multiplicated) or integrated at more than one location in the genome. Therefore, a stable transgenic line is established with F2 generation (Table 4.7).

The Tol2 system was used for the generation of Tg(alpl:nlsEGFP) and Tg(myo6b:Gal4VP16-pA) transgenic lines.

4.5.1. Generation of Tg(alpl:nlsEGFP) transgenic line

The Tg(alpl:nlsEGFP) transgenic line was generated using the Tol2/Gateway zebrafish kit (Kawakami & Noda, 2004; Kwan et al., 2007). The alpl:nlsEGFP plasmid was cloned as described in chapters 4.1.1- 4.1.5. Next, 25 µg/µL alpl:nlsEGFP plasmid and 25 µg/µL transposase mRNA solution was injected into the cell of the one-cell stage wild-type embryos (see also chapter 4.4, Figure 4.1). The embryos were screened for fluorescence at 5 dpf, and GFP-expressing larvae were raised to adulthood. Adult F0 fish with the transgene in the germline were identified by screening the F1 larvae. Distinct patterns were identified in the F1 generation. Pattern A with labeled neuromast cells was selected to establish a stable alpl:nlsEGFP transgenic line.

4.5.2. Generation of Tg(myo6b:Gal4VP16-pA) transgenic line

The Tg(myo6b:Gal4VP16-pA) transgenic line was generated using the Tol2 transposition system (Kwan et al., 2007). The myo6b:Gal4VP16-pA plasmid was a gift from K. Kindt. In addition to the myo6b:Gal4VP16-pA DNA sequence, the plasmid contained a transgenesis marker cassette cmlc2:EGFP-polyA (cytoplasmic EGFP in the heart). The myo6b:Gal4VP16-pA plasmid was injected with a concentration of 25µg/mL and 25µg/mL transposase mRNA into the cell of one-cell stage wild-type embryos. The carrier F0 fish was identified in the next generation by observing the green fluorescence in the heart of the F1 larvae. A stable transgenic line was obtained in two generations of outcrossing.

4.5.2.1. Gal4 – UAS expression system

In combination with the Tol2 transposition system (Kwan et al., 2007), the galactose-inducible system of yeast Gal4 – UAS is commonly used in zebrafish to achieve tissue or cell-type-specific expression of the desired gene (Asakawa & Kawakami, 2008). The transcriptional activator Gal4 and its consensus UAS binding site drive the expression of the downstream gene. The system easily enables specific labeling of a tissue or testing function of the selected gene while bypassing its potential lethality. For example, a transgenic zebrafish line expressing Gal4 activator under a tissue or cell-type specific promoter is crossed with another transgenic zebrafish line, with inserted transgene after the upstream

activating sequence (UAS) sequence. In the double transgenic progeny, the Gal4 binds to the UAS and drives the expression of the selected gene.

In this thesis, Gal4 – UAS expression system was used to drive the expression of Notch1a intracellular domain (NICD) in hair cells by combining myo6b:gal4 and UAS:NICD transgenic lines. Note that commonly used, a more potent version of the Gal4 transcriptional activator, namely Gal4 fused to the activating region of the herpes simplex virus protein VP16, is expressed in the myo6b:gal4 transgenic line.

4.6. Somatic mutagenesis

Somatic mutagenesis was performed using a CRISPR-Cas9 approach with redundant sgRNAs targeting of a single gene (R. S. Wu et al., 2018). The average efficiency of the method is around 90% (R. S. Wu et al., 2018).

For somatic mutagenesis of *emx2,* the sgRNAs, generated using MEGAshortscript™ T7 Transcription Kit (see chapter 4.1.8), were used. Briefly, a solution of 1 µg/µL equimolar mixture of 4 sgRNAs, 5 µM Cas9 protein, 300 mM KCl (see also chapter 4.1.9) was injected into one-cell stage embryos (wild type or *notch1a* mutant). The genotypes and phenotypes after somatic mutagenesis with 90 % efficiency are summarized in Table 4.8. In practice, the efficiency of somatic mutagenesis was assessed by observing the Emx2-deficient hair cell polarity phenotype in 2-3 dpf larvae.

Table 4.8: Overview of the probable phenotypes after *emx2*, *notch1a* double mutant generation by somatic mutagenesis of *emx2* in *notch1a* mutants.

***notch1a* het x *notch1a* het mut**		***emx2* somatic mutagenesis, *notch1a* het x *notch1a* het mut**
Phenotype	Genotype	Phenotype
	25% wt	23% *emx2* mut, 2% wt

75% wt	50% *notch1a* het mut	45% *emx2* mut, 5% wt
25% *notch1a* mut	25% *notch1a* hom mut	23% *emx2*, *notch1a* double mut, 2% *notch1a* mut

wt – wild type, mut – mutant, hom – homozygous, het – heterozygous

The probability of genotypes and phenotypes is summarized for 90% efficiency of somatic mutagenesis of *emx2* in the embryos from the incross of heterozygous *notch1a* mutant fish.

The somatic mutagenesis of *wdpcp* and *hmx2* was performed in the same way as somatic mutagenesis of *emx2* described above, but the RNPs were injected into wild-type, myo6b:GFP one-cell stage embryos. The results were observed in 3 dpf larvae.

4.7. Pharmacology: DAPT-treatment

DAPT (N-[N-(3,5-difluorophenacetyl)-L-alanyl]-S-phenylglycine-t-butyl ester) was used for global inhibition of Notch signaling. In particular, 2 dpf-old larvae were incubated in 100 µM DAPT in 0.3x Danieau's solution for 24h. During the next 24h, they were left to recover in 0.3x Danieau's solution. The incubations were performed at 28.5°C, and DMSO was diluted in 0.3x Danieau's solution for control specimens.

4.8. Immunohistochemistry

4.8.1. Larvae fixation

Larvae were fixed prior to dye staining or immunochemistry. The larvae fixation included three steps: First, the larvae were euthanized. Second, the larvae were fixed with 4% PFA (paraformaldehyde) solution in PBS medium for 4 h at room temperature. Third, the larvae were washed four times with PBST (0.05% tween-20) for 10 min.

4.8.2. Antibody staining

Immunohistochemistry allows for direct protein visualization with protein-specific antibodies. The following protocol was used for Emx2-antibody staining of freshly fixed wild type; *emx2* mutant; *notch1a* mutant; brn3c:gal4, UAS:NICD and myo6b:gal4, UAS:NICD larvae. The mutant or transgenic lines were stained simultaneously as wild-type control. Importantly, no methanol was used to preserve the hair bundles. Therefore, the fixed embryos were permeabilized with pre-chilled acetone at −20°C for 5 minutes and rinsed with PBST. 2 h incubation in blocking solution (1.5% BSA, 1.5% sheep serum in PBST) followed at room temperature. Third, the samples were bathed in the solution with primary Ab (Emx2 1:200) for 40 hours at 4°C. Afterward, the primary Ab was removed, and three washing steps followed. The samples were bathed in the solution with secondary Ab (GaRb 594) and incubated ON at 4°C. In the final step, the samples were washed with PBST and further stained or mounted for imaging.

4.8.3. DAPI staining

To visualize the nuclei, fixed larvae (or following the immunostaining) were stained with DAPI (4',6-diamidino-2-phenylindole) by 1 h incubation at room temperature.

4.8.4. Phalloidin staining

To visualize the hair bundles, fixed larvae were stained overnight with phalloidin (Alexa Fluor™ 488 Phalloidin diluted 1:20). Importantly, the samples were protected from light.

4.9. Imaging and live video-microscopy

For imaging of fixed immunohistochemically stained samples, screening live *emx2*-mutant embryos at 2-3 dpf, and live video microscopy, a custom-built inverted spinning disc microscope (Zeiss Axioscope) with 63× water immersion objective was used.

4.9.1. Larvae mounting

For the *in vivo* imaging, the larvae were bathed in MS-222 (tricaine) 0.16 g/L and mounted in 1% low–melting-point agarose with a diluted anesthetic. Specifically, 4 – 6 larvae were placed on a coverslip of a glass-bottom dish (MatTek) and covered with melted low–melting-point agarose. Before the agarose solidified, the larvae were gently positioned in a lateral position by a pipette tip. Next, the agarose was left for 5 min to harden completely. Then the 0.3x Danieau's solution with MS-222 0.16 g/L (for live video-microscopy, 0.08 g/L of MS-222 was used) was added. During live videomicroscopy of *emx2* mutant larvae, at least one of the simultaneously imaged larvae was wild type. The larvae were positioned so that the x-axis of the images corresponded to the animal's body axis.

Fixed larvae were imaged immediately after staining and were mounted in the same way as live samples.

4.9.2. Imaging

Images of mounted larvae (see the previous chapter) with stained or fluorescently labeled neuromast cells were taken with 63x objective of the custom-build spinning disc microscope 12 – 20 z-stack images of single neuromasts were taken with 1 µm z distance. The images for the red, green, and blue channels were taken sequentially for each stack. Image acquisition of live larvae was performed at 28.5°C. Furthermore, the video-microscopy included time-lapse image acquisition every 150 - 240 seconds.

4.9.3. Image processing

All images were viewed and processed with Fiji (Schindelin et al., 2012). The contrast correction was performed separately for each channel; the gamma-value was not adjusted.

Processing of time-lapse images included stitching of sequential parts of a movie and manual movie registration for image stabilization and cropping the region of interest (neuromast) to reduce the file size.

4.9.4. Quantification of hair cells orientation

The hair cell orientation was observed in myo6b:GFP (wild type or mutant) transgenic line or in the fixed, phalloidin-stained larvae, where the orientation of hair bundles is visible. Moreover, the orientation of hair cells was analyzed from images of horizontal neuromasts, obtained with a spinning-disc microscope, 63x objective (see chapters 4.9.1-4.9.3). The images were analyzed in Fiji (Schindelin et al., 2012). Specifically, a line corresponding to the orientation of each hair bundle was drawn manually as an overlayer. The hair cells, of which the polarity was not clearly evident, and the neuromasts with only one hair cell with visible polarity, were not used in the analysis. Next, the angles of all lines from all images of neuromasts from an experimental condition (or phenotype) were calculated in Fiji (Schindelin et al., 2012). Next, the angles were plotted in a circular histogram using R 4.0.2 (R Core Team, 2020). Additionally, the percentage of cells with caudad (angle 0 – 90 and 180 – 360 degrees) or rostrad (angle 90 – 180 degrees) orientation was quantified.

The orientation of hair cell bundles was quantified in the same manner in wild type, or mutant, myo6b:GFP transgenic larvae and wild type or transgenic brn3c:gal4, UAS:NICD larvae stained with phalloidin. Additionally, the orientation of hair cells in *emx2*, *notch1a* double mutant larvae was analyzed in larvae of the *notch1a* mutant line with somatically mutated *emx2* as described in the previous section. To this end, the efficiency of the somatic mutagenesis of *emx2* was first assessed by injecting the wild-type embryos and quantifying the hair cells' orientation. Approximately 10% of background (hair cells without mutations) was expected in the *emx2*, *notch1a* double mutant.

4.9.5. Tracking of cells in time-lapse movies

The time-lapse movies of neuromasts resulting from live videomicroscopy experiments were produced and processed as described in chapters 4.9.2 and 4.9.3. To analyze the movement of cells in two dimensions, the centers of cells were tracked manually in a hyper stack movie using the Fiji plugin MTrackJ (Meijering et al., 2012). This way, the coordinates of centers of the analyzed cells at different time points of the movie were obtained and used for further analyses as described in the following chapters.

First, for analysis of planar cell inversions, only the newly produced hair cells were tracked

from the moment of their production. The newly produced hair cells were tracked the same way in movies from wild type and *emx2* mutant larvae, both expressing GFP in hair cells (all the movies were produced by imaging larvae of the myo6b:GFP transgenic line, additionally some larvae were also expressing alpl:nlsEGFP or cldnb:GFP). If more than one new hair cell pair was produced in the same neuromast, the cells were tracked and later analyzed independently. 42 pairs of nascent sibling HCs from *emx2* mutant larvae and 71 pairs of nascent sibling HCs from wild-type larvae were tracked for a minimum of 5h from the moment of the production (a division of a UHCP).

Second, for analysis of all cellular movements in a neuromast, all the cells in a wild-type neuromast were tracked for the analysis of pair-wise movements of all the neighboring cells in a neuromast. For this purpose, movies from transgenic line myo6b:GFP, alpl:nlsEGFP, and myo6b:GFP, cldnb:GFP were tracked. Specifically, 323 cells from 5 neuromasts were tracked for a minimum of 6h per movie.

4.9.6. Calculation of the positional angle of a cell pair

The coordinates of two cells in time were obtained by cell tracking as described in chapter 4.9.5. The angle of the line going through the center of both cells with the x-axis was calculated from cell x and y coordinates using R 4.0.2 (R Core Team, 2020). Importantly, the angle of the cells with the x-axis was named their **positional angle** at a given moment (Figure 4.2). Importantly, the positional angle was calculated in the same way for nascent sibling HCs' movement as well as for the pairs of neighboring cells. For example, a positional angle of 0^{o} or 180^{o} at a specific time point would mean the cells are aligned with the planar polarity axis (x-axis). Moreover, the angular movement was defined as the positional angle vs. time. It was plotted in R 4.0.2 (R Core Team, 2020) for all analyzed HC pairs to obtain a general overview of the process. Notably, the dataset with information of the positional angle in time was used to analyze the PCI frequency, PCI onset, PCI termination, and final positional angle of sibling HCs. Additionally, the information about the positional angle of all neuromast cells was used for the analysis of the whole-neuromast cellular movements.

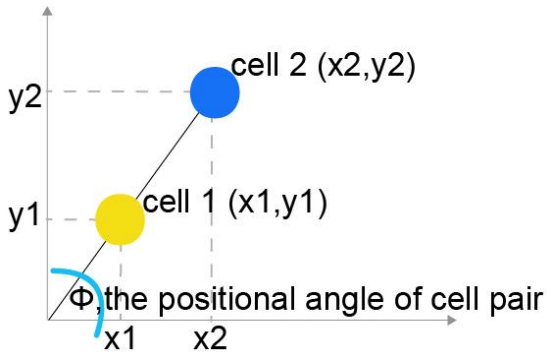

Figure 4.2: Positional angle. Schematic presentation of the definition of the positional angle of two cells. Note that ϕ=arccos ($\frac{|(|x2|-|x1|)|}{\sqrt{(|x2|-|x1|)^2+(|y2|-|y1|)^2}}$).

4.9.7. Analysis of a cell pair rotation consistency

The rotational movement of the cell pair was analyzed as the positional angle change in time. Additionally, to estimate the degree of coordination of the movement of cell pairs, the ratio between positional angle change and absolute positional angle change was calculated, which signifies the amount of rotation consistency. For example, a cell pair, which performed a rotation of a certain angle, would have a high rotation consistency if the cells did not wobble while rotating.

4.9.8. Pair-wise analysis of all neuromast cells' movements

The pair-wise movements of all the neighboring cells in a neuromast were analyzed from the tracking data produced as described in chapter 4.9.5 and illustrated in the figure below (Figure 4.2 A-B). The movement of the cells was analyzed using R 4.0.2 (R Core Team, 2020).

To this end, all cell pairs with cell-to-cell distance between 1 and 6µm and coexisting for no less than 250 minutes were considered biologically relevant based on manual curation and taken into analysis. The positional angle of the cell pair (Figure 4.2) was calculated at each time point, and subsequently, the change in angle was calculated as the minimal change (in respect to the direction of rotation) between any frame and the frame preceding it (Figure 4.3 C). The angle change was defined as the sum of angle changes between all frames. The absolute angle change was defined as the sum of absolute angle changes across the movie, approximating undirected cell behavior (cell wobbling).

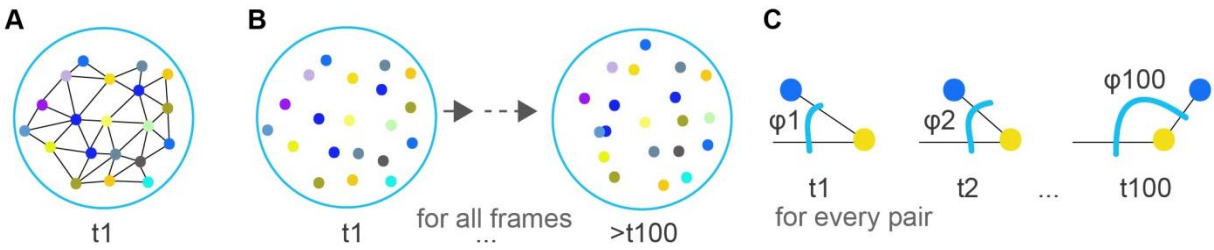

Figure 4.3: Workflow of neuromast cell's movements. Schematic illustration depicting the first steps of the analysis of the movement of all neuromast cells. (**A**) Selecting the neighboring pairs, (**B**) tracking the cells in all frames, (**C**) calculating the positional angle of each pair in all frames.

4.9.9. Definition of PCI and the quantification of PCI frequency

The frequency of the PCI was calculated as the number of inverting HC pairs vs. the total number of HC pairs analyzed. A pair was counted as having performed a PCI if the two sibling hair cells changed their angular position for more than 90 degrees. The frequency of PCI in wild type and *emx2* mutant larvae was compared using an exact binominal test using R 4.0.2 (R Core Team, 2020).

4.9.10. Analysis of PCI dynamics

Distinct aspects of PCI dynamics were analyzed. First, plots of angular change in time were generated for each pair of nascent sibling HCs to gain an overview of the process. Next, a four-parameter logistic curve (L4) was fitted to the absolute cumulative angle in time using R 4.0.2 and library drc 3.0-1 using the following R notation:

drm(positional angle ~ time, data_for_cell_pair, fct = L.4(), type = "continuous")

Specifically, the times of PCI onset, termination, and duration were analyzed for nascent sibling HCs from wild type and *emx2* mutant larvae. First, the onset of PCI, which corresponds to the time when the HC pair starts inverting. The onset was defined as the time when the line with the maximum derivative of the corresponding L4 curve, going through the inflection point of the same curve, intersects the curve's minimum value. In a similar manner, the termination of PCI was defined as when the same line intersects the curve's maximum value, and this corresponds to the cessation of rotational migration of

sibling HCs. Third, the duration of PCI corresponds to the time of PCI termination minus the time of the PCI onset.

Additionally, an average absolute angle change corresponding to the wobbling (see chapter 4.9.7 and Figure 4.2) of nascent sibling HCs from wild type and *emx2* mutant larvae was computed.

4.9.11. Quantification of sibling HC pair final angular position

The final angular position of the sibling HC pair was defined as the angular position of the HC pair after the HCs stopped rearranging. Specifically, the final angular position was calculated from tracking data as the average positional angle of 10 frames of the movie 500 min after the HC pair was produced. Note that in movies shorter than 500 min, the final positional angle was calculated at the end of the movie after inspecting that a PCI termination has taken place before. The final angular position was calculated to quantify the HC pair's final alignment with the x-axis (anterior-posterior axis in horizontal neuromasts). Importantly, I did not differentiate between sibling HC pairs, which did or did not perform a PCI before reaching their final angular position. Subsequently, the angular positions of 0 and 180 degrees were considered equivalent.

4.10. scRNAseq

4.10.1. scRNAseq sample preparation (larvae dissociation)

Enzymatic dissociation of larvae was the first step of sample preparation for scRNAseq.

The trunks of 6 and 7 dpf zebrafish larvae were cut manually after the yolk in order to collect only the cells from the posterior lateral line neuromasts and discard the GFP-positive cells in the heart of myo6b:GFP line. The cut trunks were collected in ice-cold Ringer's solution and dissociated enzymatically. I optimized the process of enzymatic dissociation by testing different enzymes (trypsin, papain, Accutase - proteolytic and collagenolytic enzymes), varying concentrations, duration, and temperature of the dissociation. The 1:1 mixture of Accutase and Accumax performed best when dissociating the larval trunks at room temperature for 25 minutes. To accelerate the dissociation, I gently triturated the solution

with a 1 ml pipette tip every 3 min at room temperature. The incompletely dissociated parts of the tissues were let to sink to the bottom, and the solution, containing dissociated cells, was moved to a fresh tube and washed with cold Ringer's solution without $CaCl_2$. The cells were resedimented by centrifugation at 17000rpm. Next, the cells were kept on ice and resuspended in sort buffer (Ringer's solution without $CaCl_2$, 2 mM EDTA, 10% FBS) and filtered twice through a 40-µm strainer. After the larvae dissociation, the FAC-sorting followed shortly.

4.10.1.1. scRNAseq sample preparation (FACS)

Fluorescence-activated cell sorting (FACS) was used for the isolation of GFP-expressing cells for the scRNAseq. Immediately after the dissociation, the single-cell solution was FAC-sorted. To distinguish between live and dead cells, 5 min staining with 5 µg/mL 7-AAD took place. The following gating strategy was used: First, the single cells, live cells were isolated, and the second gate isolated the GFP-expressing cells, which were collected in the sort collection buffer. To avoid sequencing cells being exposed to stress conditions for a longer period of time, the sorting time was limited to 25 min.

For the scRNAseq with 10x Chromium, the GFP-positive cells from myo6b:GFP and Gw57a transgenic lines were FAC-sorted and collected separately. GFP-negative cells were added to both 10x samples for control of gating specificity.

For the scRNAseq with mcSCRB-seq, the protocol as described previously (Bagnoli et al., 2018) was followed. The cells expressing green fluorescent protein (myo6b:GFP and myo6b:GFP; *emx2*-mutant) were placed one cell per well into two 96-well plates, which already contained lysis buffer, consisting of 5 M Guanidine hydrochloride, 1% 2-mercaptoethanol, and a 1:500 dilution of Phusion HF buffer, and immediately frozen on dry ice.

4.10.2. Single-cell library construction and data processing

Single-cell sequencing is based on cell-unique barcoding of transcripts.

For the scRNAsq with 10x Chromium, the FAC-sorted cells were loaded onto the 10x

Chromium™ Chip (10x Genomics) to produce Gelbeads-in-Emulsions, using the gel bead kit v2 from 10x Genomics. The barcodes were introduced in the reverse transcription step. Next, the cDNA was amplified, and 3' gene expression libraries were generated using the Chromium Single Cell 3' library (10x Genomics) from two FAC-sorted samples (cells isolated from Gw57a line, named support cells sample, and cells isolated from myo6b:GFP line, named hair cells sample). The libraries were pooled and sequenced together to a depth of approximately 100,000 reads per cell on the HiSeq4000 (Illumina) with 150 bp paired-end sequencing. Next, the data was demultiplexed by sample indices and mapped to the zebrafish genome GRCz11.

For the scRNAsq with mcSCRB-seq (Bagnoli et al., 2018), the FAC-sorted, lysed cells in a 96-well plate were cleaned using SPRI beads and resuspended with 9 µL of reverse transcription master mix and 1 µl 2 µM barcoded oligo-dT primer. Libraries were paired-end sequenced on a high output flow cell of a HiSeq 1500 (Ilumina) to the depth of 811,000 reads per cell (approaching the theoretical saturation). The labeling of transcripts was achieved by oligonucleotides with 16 bases for the cellular barcode and UMI and 8 bases for the i7. 50 bases for the cDNA were read. Fastq files were evaluated using FastQC (v0.10.1) and preprocessed using zUMIs (v2.0) with the default settings. Finally, the data were mapped to the zebrafish genome GRCz11.

4.10.2.1. Quality control and single-cell data processing

The single-cell data quality control and processing steps were performed by **Subarna Palit**. In short, standard quality control filtering steps were used to eliminate noisy and unreliable cells by assessing the number of UMIs (Unique Molecular Identifiers), the number of detected genes, and the fraction of counts from mitochondrial genes. In particular, cells with less than 800 detected genes were filtered out (potentially dying cells or empty droplets driven by ambient RNA contamination). Next, the library size was normalized to counts per million, and a log-transformed gene expression matrix was generated. The top 4000 highly variable genes were identified using the Python package Scanpy (v1.4.3) (Wolf et al., 2018) and later used to perform principal component analysis (PCA). Scrublet v0.2.1 pipeline was followed for doublet removal (Wolock et al., 2019).

Similarly, the mcSCRB-seq dataset was subject to QC measures. The limit of the count depth was set to 20 000 reads. Cells with less than 1 250 genes were eliminated. The normalization step included the count depth scaling and log transformation. The batch effect between plates was corrected using Combat (Johnson et al., 2007). PCA and Louvain clustering were applied similarly to the previous cluster analysis.

4.10.3. scRNAseq data analysis

4.10.3.1. Selection of neuromast cell clusters in 10x Data

After the QC steps, the UMAP (Uniform Manifold Approximation and Projection) algorithm was used for the visualization of data. Following dimensionality reduction and setting the local neighborhood to 25, the data were clustered by Louvain clustering with resolution 0.4. The merged dataset included GFP-expressing neuromast hair and support cells, the EGFP-non-expressing cells (control of sorting specificity), as well as the cells, which were FAC-sorted as EGFP-positive cells from the Gw57 line. However, the EGFP was not detected in those cells, suggesting they belonged to other non-neuromast cell types. The neuromast cell clusters were selected based on the expression of previously selected neuromast marker genes. 2 out of 7 clusters were annotated as neuromast cells and therefore selected for second-level clustering.

4.10.3.2. Neuromast cell clusters annotation

The neuromast cells identified in the merged 10x dataset (support and hair cell samples) were sub-clustered using Lovain clustering. Resolution 0.55 was used, and the local neighborhood was lowered to 15 using Scanpy (Wolf et al., 2018). Specifically, clusters of support cells, UHCPs, young hair cells, and mature hair cells were identified. An additional cluster was annotated as hair cells with lower quality (or potentially damaged cells) due to the lower cout depth of this cluster, high mitochondrial reads, and a lower number of detected genes.

4.10.3.3. Pseudotime analysis

Pseudotime analysis was performed on 1,167 cells scRNA-sequenced by 10x Chromium and identified as neuromast cells. Pseudotime analysis was done using the Scanpy toolkit (v1.4.3) (Wolf et al., 2018). The root required for pseudotime analysis was placed into the support cell with the maximum diffusion component (DC) DC1 or minimum DC2 value. The diffusion pseudotime was calculated using a random-walk-based cell-to-cell distance metric. Moreover, the expression of selected genes across the pseudotime was analyzed. 100 data points were used to compute the running average expression for each gene.

4.10.3.4. Analysis of cluster-enriched genes

To get a broad overview of the features of each cluster, the enriched gene ontology (GO) terms of each cluster were identified. First, the top 100 genes characterizing each cluster were computed using the *scanpy.api.tl.rank_genes_groups* function of the Scanpy toolkit (v1.4.3) (Wolf et al., 2018)., using default parameters. Second, the differentially expressed genes in each cluster were analyzed with an online tool, GOrilla (Gene Ontology enRIchment anaLysis and visuaLizAtion tool) (Eden et al., 2009). Specifically, I used the target and background list as an input, where the target list included the top 100 genes characterizing each cluster and the background list included all detected genes. Search for enriched GO terms allowed me to find which biological processes and molecular functions are enriched in each cluster.

4.10.3.4.1. KEGG pathway analysis

To identify the biological pathways enriched in the UHCPs cluster, a Kyoto Encyclopedia of Genes and Genomes (KEGG) pathway analysis was performed with the Python toolkit GProfiler (v1.0.0) (Raudvere et al., 2019). The top 200 genes characterizing UHCPs (computed using the Scanpy toolkit (v1.4.3) (Wolf et al., 2018) as in the previous chapter) were used as an input for the GProfiler function: statistical enrichment analysis from KEGG. All the genes in the filtered dataset were used as the background genes. The p-value was corrected for multiple testing using a false discovery rate (FDR).

4.11. Illustrations

All schematic illustrations were drawn manually using Adobe Illustrator software.

5. Results

5.1. Single-cell transcriptional analysis of neuromast cells of larval zebrafish

To gain knowledge about the symmetry-breaking event, which is an essential step in the establishment of bipolar epithelium, I set out to transcriptionally profile the neuromast hair cells on a single-cell level. My goal was to learn about the hair cells, particularly when their polarity is established, to determine when the polarity-associated molecular signature is acquired. The hair cell lineage originates from the support cells. Following a unipotent hair cell progenitor (UHCP) division, the two sibling nascent hair cells differentiate into functional, mature hair cells that acquire opposite orientations. Based on this, I chose to perform the single-cell transcriptional analysis of support cells, UHCPs, and hair cells. To transcriptionally profile the neuromast cells at a single-cell level, I took advantage of the 10x Chromium single-cell RNA sequencing method and the molecular crowding single-cell RNA barcoding and sequencing (mcSCRBseq) sequencing method. 10x Chromium scRNAseq method has been shown to provide reliable results and is less expensive than other methods with comparable accuracy (Vieth et al., 2019; Zhang et al., 2019). mcSCRBseq is a very sensitive method with high accuracy and has been reported to give biologically meaningful results even when sequencing a small number of cells (Bagnoli et al., 2018; Vieth et al., 2019; Ziegenhain et al., 2017).

The transcriptional analysis consisted of six sequential steps: (I) dissociation of larval trunks, (II) isolation of GFP-expressing neuromast cells with FAC-sorting, (III) single-cell RNA-sequencing with 10x Chromium or mcSCRBseq, (IV) data alignment and processing, (V) data analysis, including identification and annotation of neuromast clusters, analysis of the expression of selected genes in each cluster, pseudotime analysis, comparison of selected cell groups, and (VI) experimental validation of results.

5.1.1. Isolation of neuromast cells

The first step for transcriptional analysis on a single cell level was preparing a single-cell solution as the input sample material (Figure 5.1).

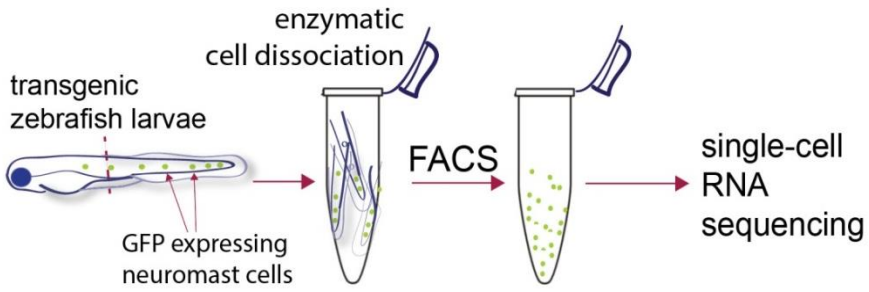

Figure 5.1.: Workflow of scRNAseq sample preparation. Workflow scheme of the single-cell transcriptional analysis, including sample preparation. GFP – green fluorescent protein, RNA – ribonucleic acid, FACS – fluorescence-activated cell sorting. Figure 5.1 is published in Kozak et al., 2020.

For the sample to include neuromast support and hair cells, I isolated cells from larvae of the transgenic zebrafish lines, expressing the (E)GFP in neuromast cells. The transgenic lines used for the scRNAseq analysis with 10x Chromium:

- Gw57a transgenic line has support cells labeled with green fluorescent protein;
- myo6b:GFP transgenic line has hair cells (and less intensively the UHCPs) labeled with a green fluorescent protein.

Additionally, to get information about the hair cells with uniform orientation, I isolated the hair cells from *emx2* mutant larvae as well. Note that the isolation of the hair cells from the *emx2* mutant line included an additional initial step, where the homozygous mutant larvae were selected as described in the methods section 4.3.2. Both zebrafish lines used for the scRNAseq analysis with mcSCRBseq have hair cells (and less intensively the UHCPs) labeled with green fluorescent protein:

- myo6b: GFP;
- *emx2* mutant, myo6b:GFP.

The first step of neuromast cell isolation included cutting the sacrificed larvae and collecting their trunks in an ice-cold Ringer's solution. I collected only the trunks of the larvae in order to discard the GFP-expressing cells from the heart of the myo6b:GFP line and simultaneously discard the GFP-expressing hair cells from the ear as well as cells from the anterior lateral line neuromasts. Immediately following, I enzymatically dissociated the larval trunks in an Accutase and Accumax solution (containing proteolytic and collagenolytic enzymes). Next, I

filtered out the undissociated cell clumps, washed the cells, and kept them on ice in the sort buffer. The cells were stained with 7-AAD before the FACS, to distinguish between live and dead cells.

The second step included fluorescence-activated cell sorting with a two-gate mechanism. The first gate was set to discard the dead cells, which were labeled with 7-AAD, as well as doublets and debris (Figure 5.2). The second gate discarded non-fluorescent cells, and the GFP-positive cells of interest were collected (Figure 5.2, far-right panel). For the scRNA sequencing with a 10x Chromium system, I collected the GFP-positive cells in a tube, where GFP-negative cells were also added as a control for sorting specificity.

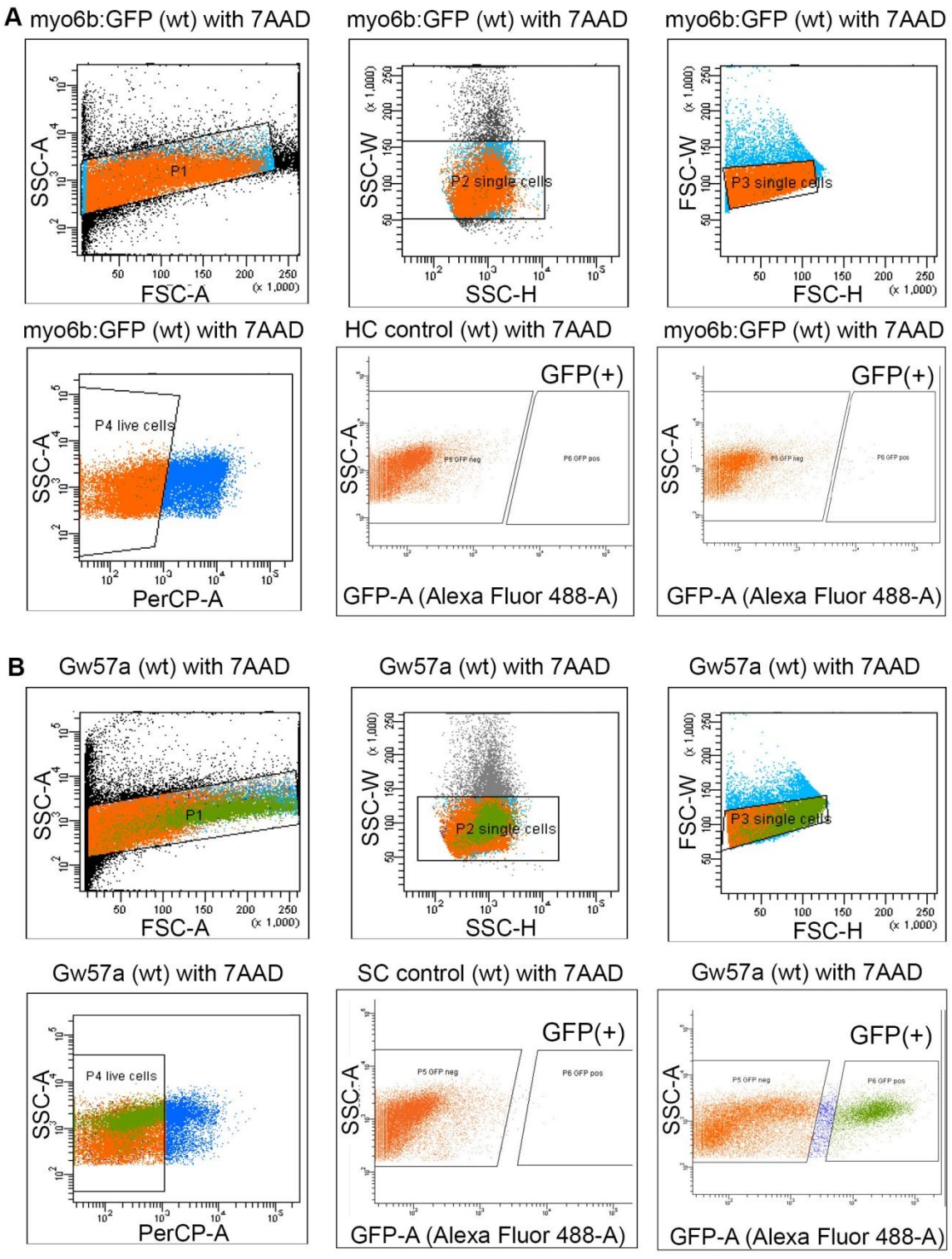

Figure 5.2: FAC-sorting (for sequencing by 10x). (**A**) FACS plots showing the isolation of single cells, live cells, and GFP-labelled cells from myo6b:GFP transgenic larvae (hair cells sample). (**B**) FACS plots showing the isolation of single cells, live cells, and GFP-labelled cells from Gw57a transgenic larvae (support cells sample). Note that the first three panels from

the left served to distinguish single cells vs. debris and doublets. Live cells were identified in the fourth panel and the GFP-expressing cells in the far right panel. wt – wild type, FACS – fluorescence-activated cell sorting, GFP – green fluorescent protein, 7AAD – (7-amino-actinomycin D). The FACS was performed in close collaboration with Dr. Anika Böttcher and Figure 5.2 is published in Kozak et al., 2020.

For the scRNA sequencing with mcSCRBseq, I collected GFP-positive cells in a 96-well plate, with one cell per well. In particular, on each plate, half of the cells originated from the wild-type myo6b:GFP and half from the *emx2* mutant (Figure 5.3).

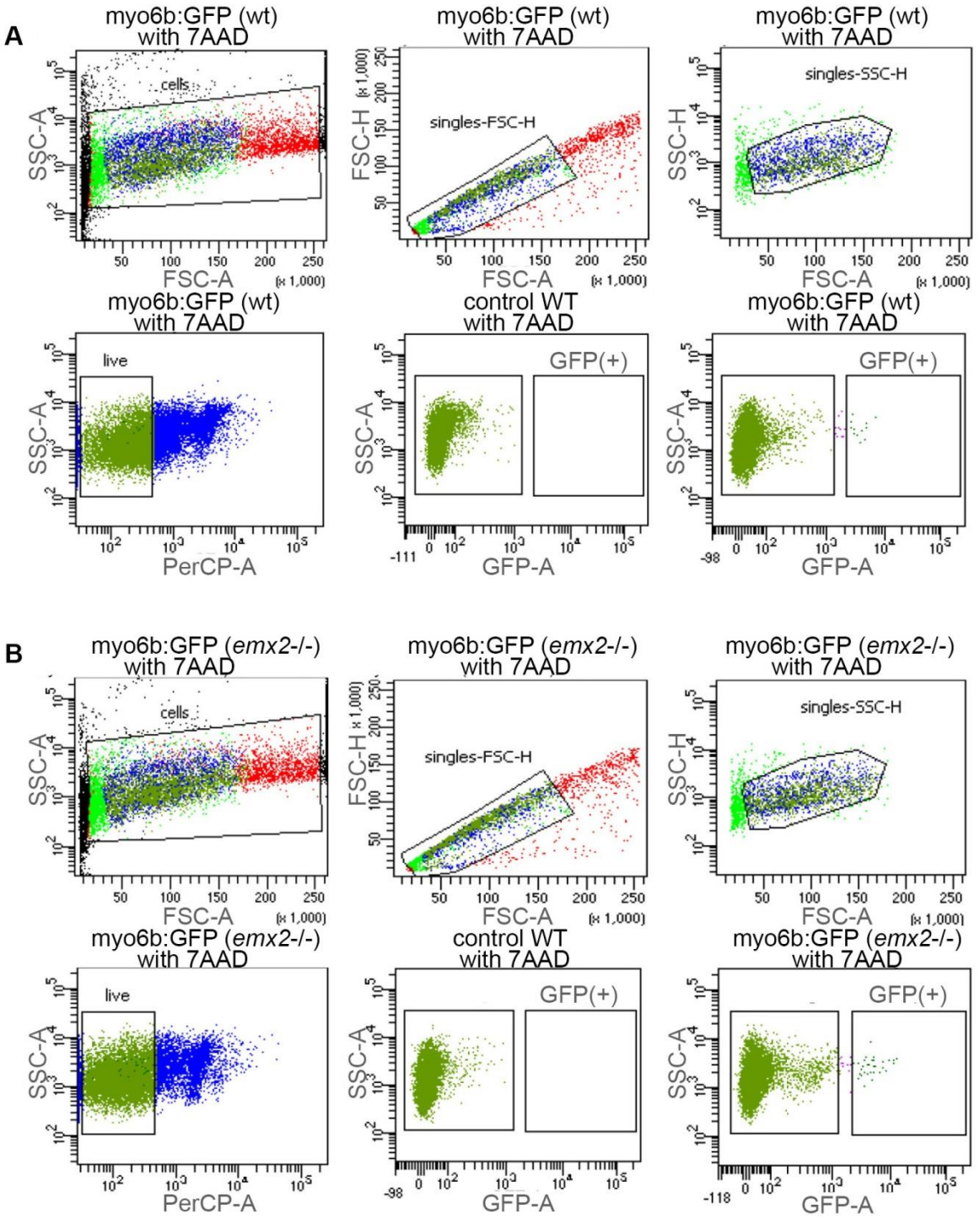

Figure 5.3: FAC-sorting (for sequencing by mcSCRBseq). (**A**) FACS plots showing the isolation of single cells, live cells, and GFP-labelled cells from wild type myo6b:GFP transgenic larvae (wild type hair cells sample). (**B**) FACS plots showing the isolation of single cells, live cells, and GFP-labelled cells from *emx2*-mutant, myo6b:GFP transgenic larvae (*emx2*-/- hair cells sample). Note that the first three panels from the left served to distinguish single cells vs. debris and doublets. The live cells were identified in the fourth panel and the GFP-expressing cells in the far right panel. wt – wild type, FACS – fluorescence-activated cell sorting, GFP –

green fluorescent protein, 7AAD – 7-amino-actinomycin D.

5.1.2. Transcriptional analysis and data processing

For the scRNAseq with 10x Chromium system, the two FAC-sorted samples containing support and hair cells from Gw57a and myo6b:GFP lines, respectively, were merged at the level of the barcoded cDNA libraries and sequenced together. For the scRNAseq with mcSCRBseq, the plates contained the cells from wild-type myo6b:GFP and *emx2* mutant, myo6b:GFP line, which were consequently processed and sequenced together.

The datasets were aligned to the zebrafish genome (GRCz11) by Dr. Thomas Walzthoeni (Bioinfor-matics Core Facility, Institute of Computational Biology, Helmholtz Zentrum Muünchen) and Alexandar Janjic (Prof. Dr. Wolfgang Enard lab, Department Biology II, Anthropology and Human Genomics, Ludwig-Maximilians-Universität München). Next, the pre-processing steps were applied by Subarna Palit from Fabian Theis' lab at the Institute of Computational Biology, Helmholtz Zentrum München. Briefly, Subarna Palit used the Scanpy toolkit (Wolf et al., 2018) and applied the standard pre-processing and quality control steps to the raw data. In particular, the doublets were removed, and the cells were filtered based on the number of detected genes, count depth, and the fraction of mitochondrial reads. The pre-processing steps ensured that only viable cells were used for downstream analyses.

5.1.3. Identification of neuromast cells clusters

After the processing steps, the 10x Chromium dataset cells (10,431 single cells) were clustered in 7 distinct clusters using the Louvain clustering function of the Scanpy toolkit (Wolf et al., 2018) (Figure 5.4 A). I looked into the expression of known neuromast marker genes in all clusters. Specifically, I analyzed the expression of sox2, myo6b, klf17, s100s, tmc2b, sost, tekt3, stm, eya1, si:dkey-205h13.2, atoh1a, s100s and GFP (Barta et al., 2018; Erickson & Nicolson, 2015; Lush et al., 2019; Ma et al., 2008; Steiner et al., 2014; Bernard Thisse et al., 2004; Thomas & Raible, 2019) For a brief description of neuromast marker genes, please see section 1.6.1 and note that the expression of non-neuromast genes was verified as control. The enrichment of the above-stated marker genes in clusters 3 and 7 revealed that those clusters consisted of neuromast cells and were consequently selected

for more refined analysis (Figure 5.4 B).

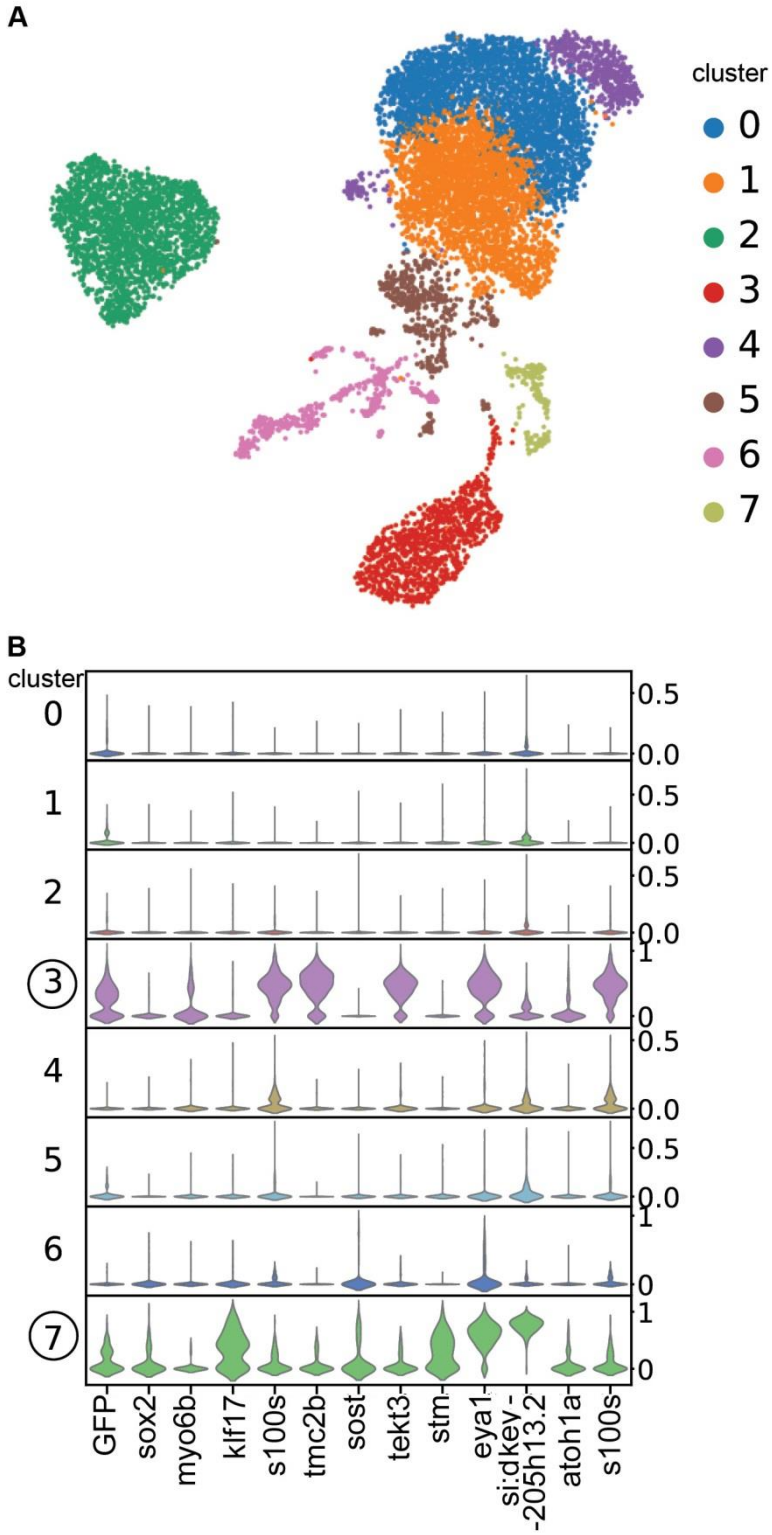

Figure 5.4: Neuromast clusters. (**A**) UMAP plot showing the clustering of all the cells sequenced by 10x Chromium (hair cells and support cells samples). (**B**) Violin plots showing the expression levels of selected genes (known neuromast marker genes and genes with high expression in neuromasts) in each cluster. Note that higher levels of neuromast marker

genes were detected in clusters 3 and 7. These clusters were selected for further analysis. GFP – green fluorescent protein. Figure 5.4 was generated in close collaboration with Subarna Palit (Fabian Theis' lab, Institute of Computational Biology, Helmholtz Zentrum München) and is published in Kozak et al., 2020.

5.1.4. Annotation of neuromast cells clusters

The 1167 cells forming clusters 3 and 7 in the previous step, which were identified as neuromast cells, with 1533 detected genes and 6074 counts per cell, were separately used in another round of dimensionality reduction (UMAP) and re-clustered using the Louvain function of the Scanpy toolkit (Wolf et al., 2018). The cells were clustered into five clusters corresponding to the major cell type groups (Figure 5.5 A). I examined the distribution of cells from the 10x hair cells sample and 10x support cells sample on the UMAP projection (Figure 5.5 B). The expression of several pre-selected neuromast and hair cell marker genes was analyzed in all cells. First, I evaluated the expression pattern of support cells marker genes: stm, sost, klf17 and si:dkey-205h13.2 (Bernard Thisse et al., 2004; Thomas & Raible, 2019) (Figure 5.5 C-F). Next, I analyzed the expression of hair cells marker genes: tekt3, myo6b, pvalb8, s100t, and s100s cells (Barta et al., 2018; Erickson & Nicolson, 2015; Lush et al., 2019; Bernard Thisse et al., 2004) (Figure 5.5 G-H) as well us hair cells and UHCPs marker genes atoh1a and dld (Ma et al., 2008) (Figure 5.5 I-J). The cells with high expression of marker genes for each cell type clustered together, which enabled me to annotate the cell clusters as support cells, UHCPs, young HCs, and mature HCs (published in Kozak et al., 2020, Figure 5.5 K).

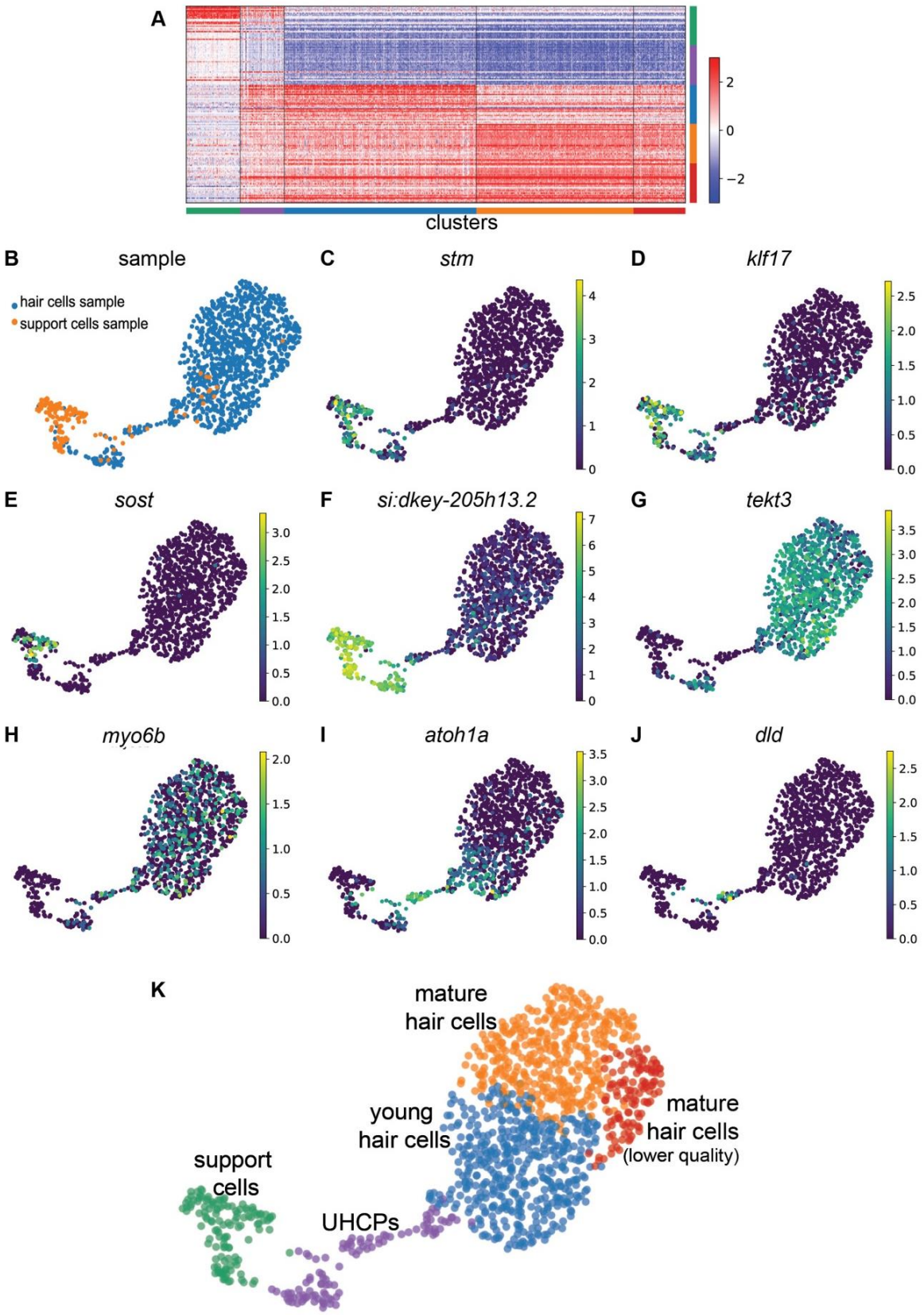

Figure 5.5: Annotation of neuromast cells clusters. (**A**) Heat-map is showing gene-

expression differences between clusters (the expression of the top 30 ranked genes of each cell cluster). (**B**) UMAP plot showing clustering of neuromast cells from support cells (orange) and hair cells (blue) samples. (**C**-**J**) UMAP plots showing log-transformed expression of selected genes: stm (**C**), klf17 (**D**), sost (**E**), si:dkey-205h13.2 (**F**), tekt3 (**G**), myo6b (**H**), atoh1a (**I**), dld (**J**). (**K**) UMAP plot showing 1,167 neuromast cells clustered into five clusters: support cells, UHCPs, young HCs (including nascent, immature HCs), mature HCs, and mature HCs of lower quality. UHCPs – unipotent hair cell progenitors, UMAP – Uniform Manifold Approximation and Projection. Figure 5.5 was generated in close collaboration with Subarna Palit (Fabian Theis' lab, Institute of Computational Biology, Helmholtz Zentrum München) and Figures 5.5 A and K are published in Kozak et al., 2020.

Even though cells in the fifth cluster expressed the mature hair cells marker genes, they had lower count depth, a higher fraction of mitochondrial genes, and fewer detected genes (Figure 5.6 A-C). Consequently, I annotated the fifth cluster as mature hair cells of lower quality (potentially damaged hair cells) (Figure 5.5 K). The mature hair cells of lower quality were omitted from further analysis.

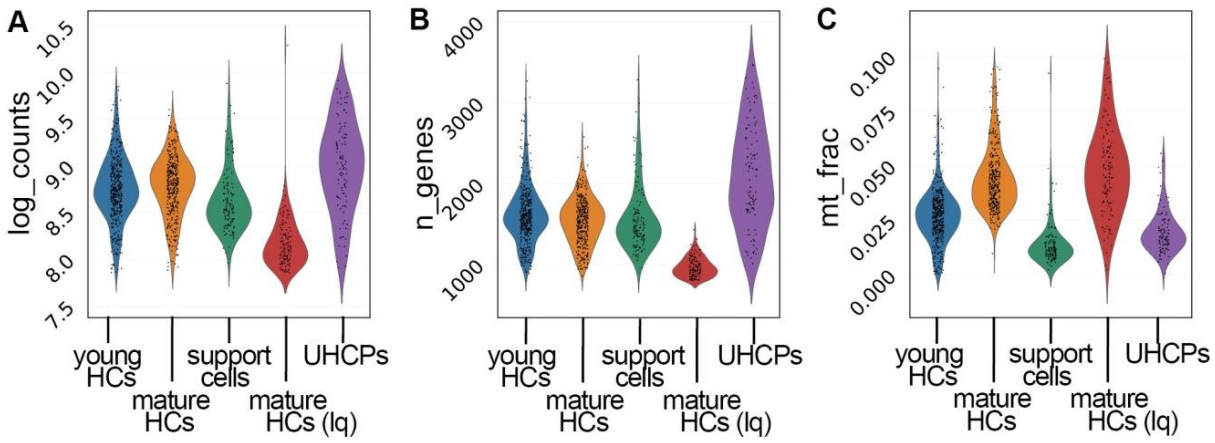

Figure 5.6: Neuromast clusters sequencing details. (**A**) Violin plots showing the distribution of count depth (log_counts), number of detected genes (n_genes), and the fraction of reads from mitochondrial genes (mt_frac) in different clusters of neuromast cells. HCs – hair cells, UHCPs – unique hair cell progenitors, lq – lower quality. Figure 5.6 was generated by Subarna Palit (Fabian Theis' lab, Institute of Computational Biology, Helmholtz Zentrum

München) and is published in Kozak et al., 2020.

Furthermore, I examined the genes with the highest differential expression in each cluster by analyzing the enriched GO-terms linked to each cluster's top 100 differentially expressed genes. To this end, I used GOrilla (Gene Ontology enRIchment anaLysis and visuaLizAtion tool), a tool for identifying and visualizing enriched GO terms (Eden et al., 2009). The analysis revealed that the enriched processes in support cells and UHCPs are in large liked to high ribosomal activity (enriched GO-terms biosynthetic process and translation, and cellular component ribosome subunit), whereas the processes in all hair cells clusters are in large linked to high mitochondrial activity (enriched GO term electron transport chain, and cellular component mitochondrial membrane part). The enriched GO terms (molecular functions) for support cells, UHCPs, young hair cells, and mature hair cells are shown in Figure 5.7 (Figure 5.7). A high expression of mitochondrial genes in hair cells as well as high ribosomal activity in the hair cell progenitors have been reported before (Barta et al., 2018; Lush et al., 2019), 2019). The support cells are a heterogeneous population consisting of the mantle and central support cells, which present a quiescent stem cell population and amplifying support cells that, in general, have high ribosomal activity (Lush et al., 2019).

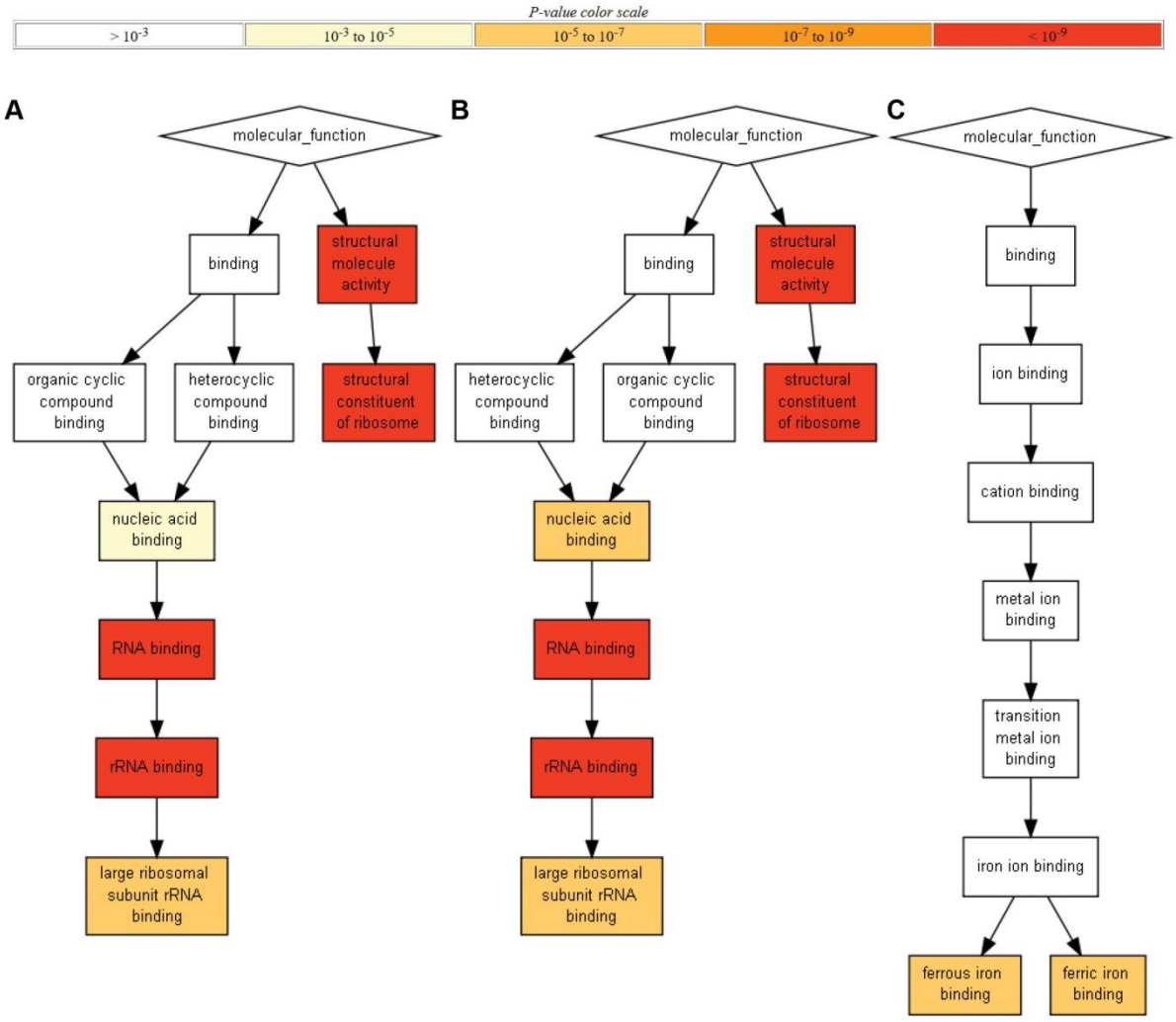
P-value color scale
> 10-3
10-3 to 10-5
10-5 to 10-7
10-7 to 10-9
< 10-9
A
molecular_function
binding
structural molecule activity
organic cyclic compound binding
heterocyclic compound binding
structural constituent of ribosome
nucleic acid binding
RNA binding
rRNA binding
large ribosomal subunit rRNA binding
B
molecular_function
binding
structural molecule activity
heterocyclic compound binding
organic cyclic compound binding
structural constituent of ribosome
nucleic acid binding
RNA binding
rRNA binding
large ribosomal subunit rRNA binding
C
molecular_function
binding
ion binding
cation binding
metal ion binding
transition metal ion binding
iron ion binding
ferrous iron binding
ferric iron binding

Figure 5.7: GO analysis. Enriched molecular function GO terms in support cell cluster (**A**), UHCPs cluster (**B**), young hair cells cluster (**C**), mature hair cells cluster (**D**). The enriched GO terms were analyzed by the Gorilla tool for identifying and visualizing enriched GO terms (Eden et al., 2009). GO – Gene Ontology.

5.1.5. Identification of *emx2*-correlating genes

The unbiased clustering of neuromast cells resulted in cells clustered based on cell type (support cells and hair cells) and their differentiation status (UHCPs, young and mature hair cells). The clustering of hair cells did not show any subdivision that could correlate with the hair cell polarity. There are two known differences between the populations of hair cells with opposite orientations, their anatomical differences, visible through the polarity of the hair bundles, and the expression of the transcription factor Emx2. To be precise, *emx2* is expressed only in caudad-oriented cells. Consequently, I decided to use *emx2* as a proxy for polarity and further analyze the hair cell subpopulations based on its expression pattern.

emx2 was expressed across all hair cell clusters, further confirming that the hair cells did not cluster based on polarity. These results strongly suggest that hair cells of different orientations are transcriptionally very similar.

Furthermore, I identified *emx2*-correlating genes by manually selecting two groups of cells:

- hair cells, in which *emx2* expression was detected,
- hair cells, in which *emx2* expression was not detected.

Theoretically, these hair cell groups corresponded to the hair cells with posterior and anterior polarity, respectively. However, the *emx2* is a lowly expressed gene, and the sequencing depth used in this analysis potentially did not allow for detection of *emx2* in all cells, in which its expression was predicted based on previous knowledge (Emx2 is expressed in 50% of the hair cells), resulting in an unavoidable bias. Nevertheless, the comparison of the two groups revealed a number of significant differentially expressed genes. *emx2* was detected in a higher percentage of young vs. mature hair cells, resulting in delineation bias between these two groups. Consequently, numerous genes, which were differentially expressed in the two manually selected groups, corresponded to the differentially expressed genes in young vs. mature hair cells. In order to avoid this bias as much as possible, I repeated the comparison of the *emx2*-expressing and *emx2*-non-expressing cells within the young hair cells cluster only. In addition to *emx2*, the analysis revealed 64 genes, which were significantly (adj. p-value<0.05) differentially expressed between the two groups (*emx2*+ and *emx2*-) (Table 5.1 listing top 10 differentially expressed genes of each group).

Table 5.1. List of top 10 differentially expressed genes in young HCs expressing emx2 vs. young HCs not expressing emx2

	Young hair cells not expressing *emx2*				**Young hair cells expressing *emx2***			
	Gene	**score**	**adj. p-value**	**log fold change**	**gene**	**score**	**adj. p-value**	**log fold change**
1	*calm3a*	8.996	1.25E-14	0.21	*emx2*	36.28	1.00E-63	30.12
2	*odf3l2a*	8.614	1.97E-13	0.59	*anxa5a*	8.179	4.31E-10	0.33
3	*AL844518.1*	7.870	9.94E-11	2.67	*fgf10a*	4.639	0.013857	0.76
4	*CU462980.1*	7.339	2.20E-09	2.57	*nqo1*	4.210	0.053546	0.12
5	*hmx2*	7.122	7.97E-09	2.32	*klhl30*	4.073	0.083233	0.53
6	*hmx3a*	6.844	4.25E-08	2.51	*ckbb*	3.821	0.205506	0.90
7	*s100t*	5.975	4.31E-06	0.07	*dnase1l4.2*	3.612	0.386300	0.92
8	*wdpcp*	5.624	3.18E-05	3.87	*zgc:162944*	3.395	0.649962	0.66
9	*zgc:195356*	5.604	3.07E-05	0.66	*gstp1*	3.379	0.649962	0.11
10	*gpx1b*	5.576	3.18E-05	0.08	*atp5pf*	3.248	0.927993	0.22

Table 5.1 was generated in close collaboration with Subarna Palit (Fabian Theis' lab, Institute of Computational Biology, Helmholtz Zentrum München). Table 5.1 lists differentially expressed genes published in Kozak et al., 2020.

5.1.6. Evaluation of *emx2*-correlating genes

The genes, identified as differentially expressed genes between *emx2*-expressing and *emx2*-non-expressing young HCs, could play a role in the HC orientation determination or other

hair cell orientation-biased processes. Their potential involvement in polarity determination was evaluated by two criteria: (I) the significance (p-value) and the log fold change of the differential expression and (II) functions or expression patterns of the genes, as previously reported in the literature.

To avoid analyzing differentially expressed genes resulting from previously described noise inherent for the method, I focused on the top 10 differentially expressed genes (Table 5.1). Apart from a few transcripts identified as part of BACs, only *hmx2*, *hmx3a*, *wdpcp* had a log fold change higher than 2 (Table 5.1, Figure 5.8). None of those genes (*hmx2*, *hmx3a,* and *wdpcp*) are specific hair cell marker genes as they are also expressed in other neuromast cells, for example, *hmx2* and *hmx3a* in A/P pole support cells (Lush et al., 2019).

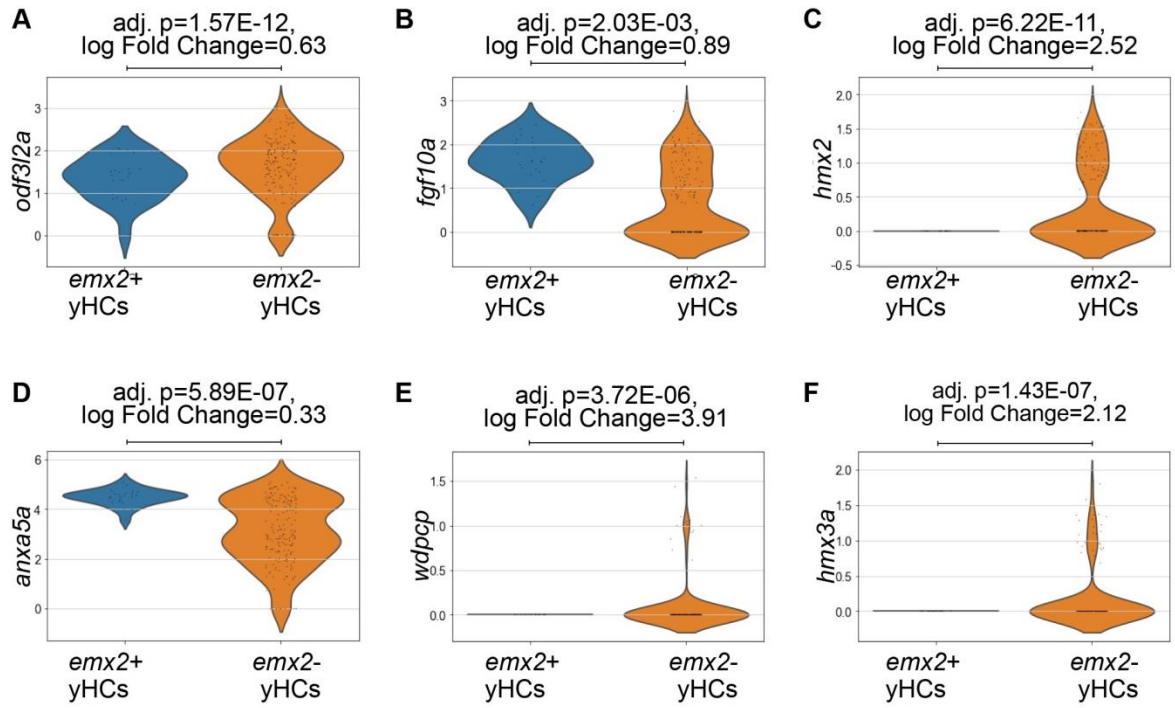

Figure 5.8: emx2-(anti)correlating genes. Violin plots showing the difference in the expression levels of selected genes in young hair cells expressing *emx2* and young hair cells not expressing *emx2*. yHCs – young hair cells. Figure 5.8 was generated in close collaboration with Subarna Palit (Fabian Theis' lab, Institute of Computational Biology, Helmholtz Zentrum München).

Next, I used a somatic mutagenesis approach to study the potential role of *wdpcp* and *hmx2* in hair cell orientation determination. For each gene, I designed four sgRNAs and injected them in the myo6b:GFP embryos together with Cas9 protein using the redundant gene targeting approach (R. S. Wu et al., 2018) (see also section 4.6). At 3 dpf, the neuromasts of the injected larvae (and non-injected controls) were observed directly using a custom-built spinning disc microscope. Somatic mutagenesis of neither *wdpcp*, nor *hmx2* resulted in neuromasts with uniformly oriented hair cells (qualitative estimation). I concluded that genes *wdpcp* and *hmx2* are not promising candidates for a determining role in neuromast hair cell orientation. Consequently, *wdpcp* and *hmx2* were not studied further. Moreover, the goal of the project was to elucidate the establishment of the planar bipolarity; therefore, instead of studying the roles of *emx2*-correlating and anti-correlating genes as its potential targets or regulators, I rather focused on analyzing the spatiotemporal dynamics of *emx2*.

5.1.7. Spatiotemporal analysis of *emx2* expression in neuromasts

To identify the time when the bipolarity of the neuromast is established, I performed a spatiotemporal analysis of *emx2* expression. The orientation-determinant factor Emx2 can reverse the orientation of hair cells; therefore, I reasoned that the time when *emx2* is first expressed correlates with the time of the symmetry-breaking event.

To find out when *emx2* is first expressed, a pseudotime analysis was performed using the pseudotime function implemented in Scanpy (Wolf et al., 2018) (Figure 5.9 A-B). As the hair cell lineage is known to arise from support cells, I selected the start position (the root) in the support cells cluster. Next, the cells were ranked corresponding to their differentiation status. Based on the differentiation status rank, expression of genes with known expression patterns, such as *stm*, *atoh1a*, *pvalb8*, *myo6b*, and *tekt3*, as well as *emx2*, were analyzed (Figure 5.9 B). The analysis of the *emx2* expression further corroborated previous observations (T. Jiang et al., 2017; Lozano-Ortega et al., 2018) that *emx2* is not expressed in support cells. Interestingly, *emx2* expression is detected in UHCPs, suggesting that the expression of this gene is initiated prior to the division that forms the two daughter hair cells (Figure 5.9 B-C). As expected, the analysis of the expression of *emx2* in young hair cells suggests that *emx2* is expressed in half of the hair cells, as also evident from the immunohistochemical analysis. Nevertheless, the identity of a UHCP could not be validated

in the immunohistochemical experiments because there are no known specific marker genes for this cell type. As a control, I also performed immunohistochemical staining of Emx2 in *atoh1a* mutant larvae, which lack UHCPs and hair cells. As expected by previous results, no cells expressing Emx2 were detected in the neuromasts of the *atoh1a* mutant larvae (Figure 5.9 D).

In summary, the pseudotime analysis of *emx2* expression revealed the initiation of *emx2* gene expression in the UHCPs (published in Kozak et al., 2020). Furthermore, the pseudotime analysis suggested that *emx2* was lost in one of the nascent sibling hair cells after the division of the progenitor cells (UHCP).

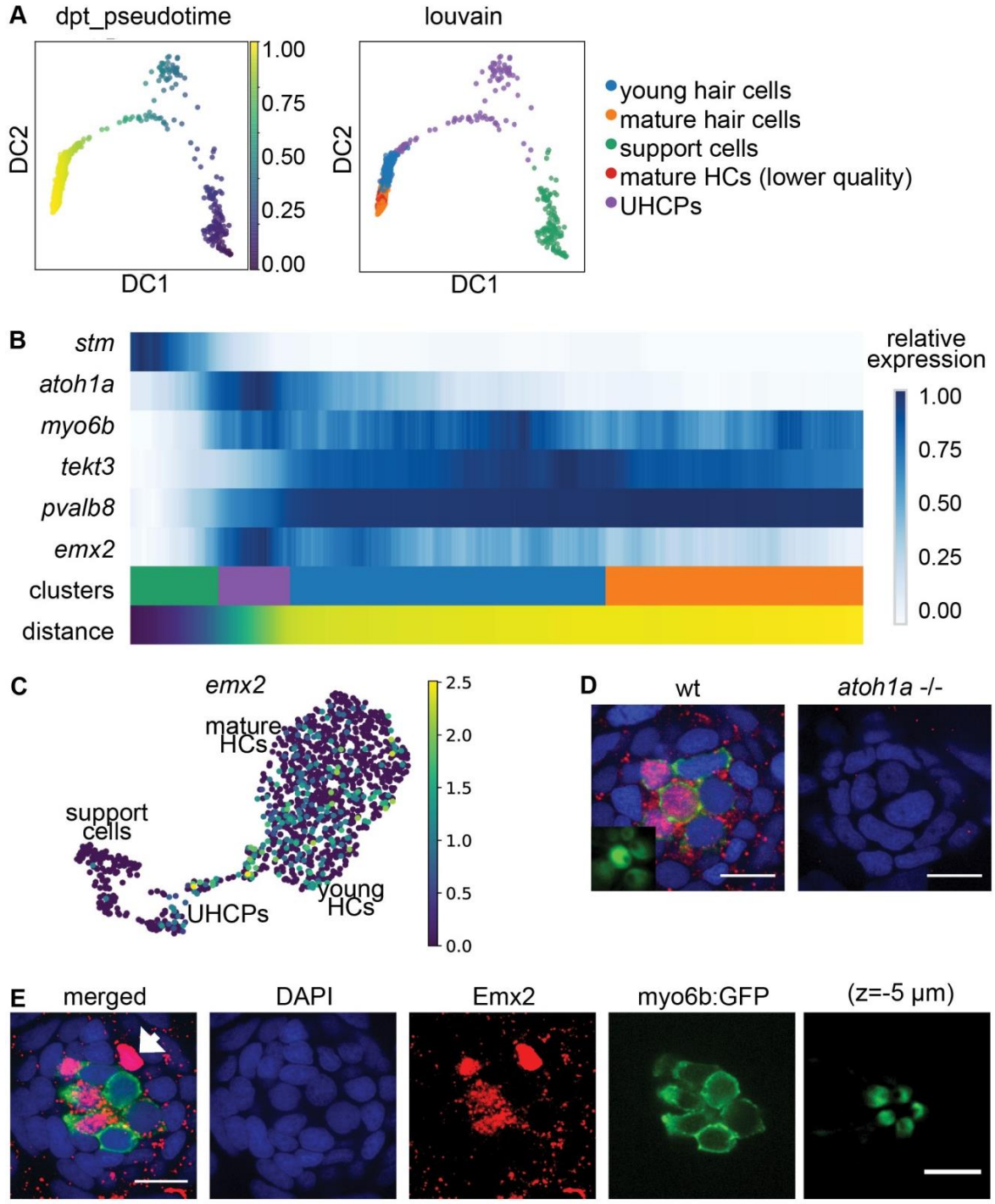

Figure 5.9: Analysis of spatiotemporal emx2 expression. (**A**) Diffusion map showing pseudotime. (left) Dark blue corresponds to the initial state (fixed diffusion pseudotime root), and yellow indicates the final stage of the differentiation process. (right) The same diffusion map is shown in the left panel with color-coded Louvain clusters labels. (**B**) Gene expression dynamics of selected marker genes along the differentiation path (diffusion pseudotime) during the differentiation of hair cells lineage. The relative gene expression is

shown for each gene as a running average of over 100 cells along the pseudotime. (**C**) UMAP plot of log-transformed *emx2* gene expression. (**D**) Immunohistochemical staining of horizontal neuromasts in the transgenic line myo6b:GFP showing HCs in green, nuclei in blue (DAPI staining), and Emx2 in red (antibody staining) in 2dpf old wt and *atoh1a* mutant larvae. wild type n=24 (neuromasts), *atoh1a* -/- n=10 (neuromasts). Scale bars are 10 µm. (**E**) Immunohistochemical staining of wild-type horizontal neuromasts in the transgenic line myo6b:GFP showing HCs in green, nuclei in blue (DAPI staining), and Emx2 in red (antibody staining) in 2dpf old larvae. The white arrow is highlighting a cell (likely a UHCP) expressing Emx2. The scale bar in the far right panel showing hair bundles (z=-5 µm, with 2x magnification) is 5 µm, in all other panels, 10 µm (as in far left). wt – wild type, HCs – hair cells, UHCPs – unique hair cell progenitors, DC – diffusion component, DPT – diffusion pseudotime. Figure 5.9 A-C was generated in close collaboration with Subarna Palit (Fabian Theis' lab, Institute of Computational Biology, Helmholtz Zentrum München). Figure 5.9 is published in Kozak et al., 2020.

5.1.7.1. Emx2 regulation

The molecular mechanism of hair cell orientation determination by Emx2 remains unknown. To gain an understanding of the process, I performed single-cell RNA sequencing of hair cells from wild type and *emx2* mutant larvae using mcSCRBseq (Figure 5.10 A-C). The hair cells from wild type and *emx2* mutant larvae in myo6b:GFP transgenic background were isolated by FAC-sorting (Figure 5.3) as described in chapter 5.1.1. After the quality control and filtering steps, the dataset of 168 single cells with a median number of unique transcripts per cell of approximately 2 500 was analyzed (Figure 5.10 B). The analysis of expression of hair cell marker genes confirmed the identity of hair cells. Note that while no Emx2 protein was detected in Emx2 mutant larvae, the *emx2* mRNA, putatively containing various genomic ablations caused by Cas9 targeting, was still expressed in the mutant line as revealed by scRNAseq and confirmed by fluorescent in situ hybridization (Kozak et al., 2020). Interestingly, *emx2* was detected in a similar fraction of hair cells from wild type and *emx2* mutant samples (37% and 43%) (Figure 5.10 C). This result strongly suggested that Emx2 activity is dispensable for the asymmetric pattern of *emx2* expression, which is therefore not auto-regulated by a feedback loop (published in Kozak et al., 2020).

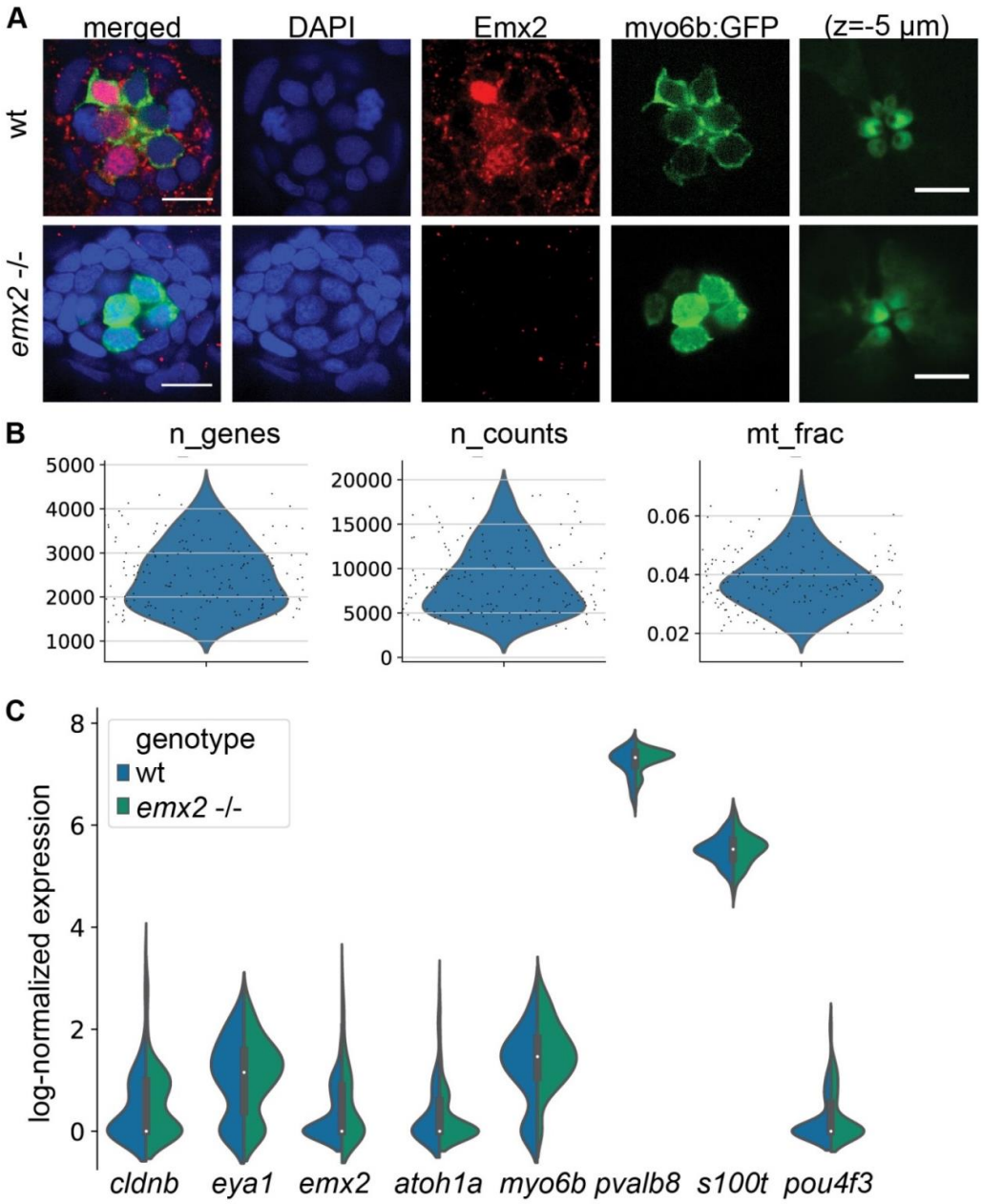

Figure 5.10: scRNAseq of HCs from wt and emx2 -/- larvae. (**A**) Immunohistochemical analysis of a horizontal neuromast in wild type (n=20 neuromasts) *emx2* mutant (n=26 neuromasts) in myo6b:GFP transgenic 2dpf larvae showing HCs in green, nuclei in blue (DAPI staining), and Emx2 in red (antibody staining). The scale bars in the far right panel showing hair bundles (z=-5 µm, with 2x magnification) are 5 µm, in all other panels, 10 µm (as in far left). (**B**) Violin plots showing the number of detected genes (n_genes), number of counts (n_counts), and the fraction of counts from mitochondrial genes (mt_frac) per barcode after quality control in the hair cells sequenced by the mcSCRBseq dataset. (**C**) Violin plots showing the expression of selected HC marker genes in the hair cells from wild type and

emx2 mutant larvae. Note that there are only negligible differences in gene expression (including *emx2*) between the wild type and *emx2* mutants. wt – wild type. Figure 5.10 B was generated by Alexandar Janjic (Prof. Dr. Wolfgang Enard lab, Department Biology II, Anthropology and Human Genomics, Ludwig-Maximilians-Universität München) and Figure 5.10 C was generated in close collaboration with Subarna Palit (Fabian Theis' lab, Institute of Computational Biology, Helmholtz Zentrum München). Figure 5.10 is published in Kozak et al., 2020.

5.2. The role of Notch signaling in hair cell orientation

5.2.1. Pathway enrichment analysis

The analysis of *emx2* expression during the differentiation of hair cells revealed the expression of *emx2* in UHCPs. After discovering that *emx2* is expressed in the UHCPs, I set out to investigate which signaling pathway is active when *emx2* is first expressed, namely in UHCPs.

KEGG pathway enrichment analysis of the top 200 genes characteristic of UHCPs showed that genes encoding for cell adhesion molecules, genes involved in tight junctions, and Notch signaling pathway genes were upregulated in UHCPs (Figure 5.11 A-B). Furthermore, Notch signaling has been reported to play a role in hair cell differentiation (Brooker et al., 2006; Ma et al., 2008), and it has been suggested to have an impact on hair cell polarity (Dow et al., 2018; Mirkovic et al., 2012). Together, this suggested that Notch signaling could be involved in hair cell orientation determination (published in Kozak et al., 2020).

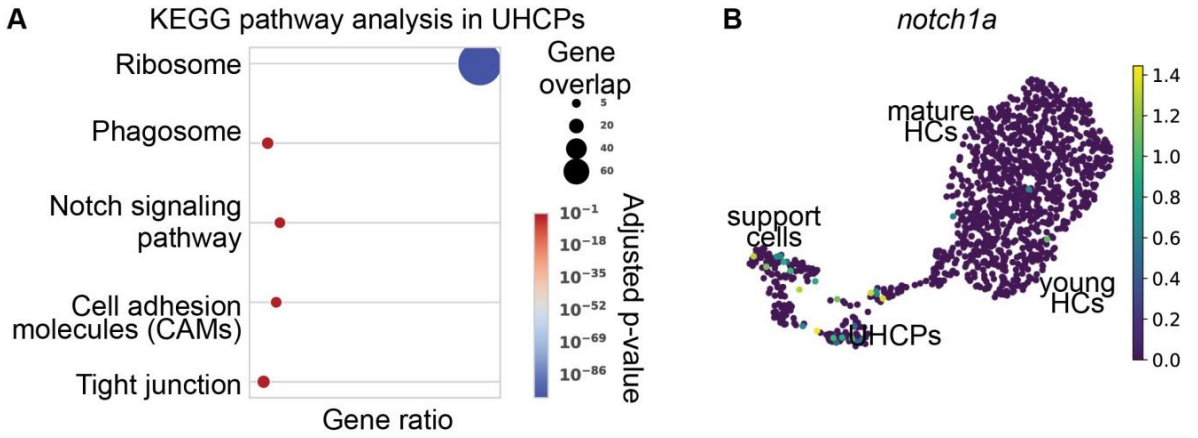

Figure 5.11: KEGG pathway analysis. (**A**) KEGG pathway enrichment analysis of the top 200 ranked genes in UHCPs. The size of the data point corresponds to the number of differentially expressed genes that constitute the given KEGG term. The color indicates the FDR corrected p-value, and the x-axis is the ratio of background genes that are contained the given KEGG term. (**B**) UMAP plot showing log-transformed expression of *notch1a* gene in wild-type neuromast cells. HCs – hair cells, UHCPs – unique hair cell progenitors, KEGG – Kyoto Encyclopedia of Genes and Genomes, FDR – false discovery rate. Figure 5.11 was generated in close collaboration with Subarna Palit (Fabian Theis' lab, Institute of Computational Biology, Helmholtz Zentrum München) and is published in Kozak et al., 2020.

5.2.2 The impact of Notch1a on hair cell orientation

The pathway enrichment analysis revealed an upregulation of Notch signaling-related genes in UHCPs. Moreover, a link between Notch signaling and hair cell polarity has been first suggested in literature after pharmacological experiments, resulting in a higher fraction of hair cells with rostrad orientation due to blocked global Notch signaling (Mirkovic et al., 2012). Larvae with misexpressed Notch intracellular domain were also reported to possess hair cells with rostrad orientation (Dow et al., 2018). Interestingly, the vast majority of the hair cells in *notch1a* mutant larvae have caudad polarity in horizontal neuromasts (Jacobo et al., 2019; Kozak et al., 2020). The pharmacological experiments resulting in the opposite phenotype of genetic manipulations called for a systematic analysis of HC orientation in distinct conditions, which I describe in the following chapters.

5.2.3. Analysis of the Emx2 expression in *notch1a* mutant larvae

The horizontal neuromasts in *notch1a* mutant larvae are populated with hair cells with caudad orientation (Jacobo et al., 2019; Kozak et al., 2020). To find out whether Notch1a acts upstream, downstream, or in parallel with Emx2, I studied the expression of *emx2* in *notch1a* mutant larvae. The *notch1a* mutant line was generated by Dr. Jerónimo Roberto Miranda Rodríguez (Hernán López-Schier lab, Research Unit Sensory Biology and Organogenesis, Helmholtz Zentrum München).

I performed an immunostaining analysis of Emx2 in the *notch1a* mutant larvae, revealing that Emx2 is expressed in all hair cells (Figure 5.12). This observation suggested that Notch1a controls the hair cell orientation by regulating the expression of *emx2* (published in Kozak et al., 2020).

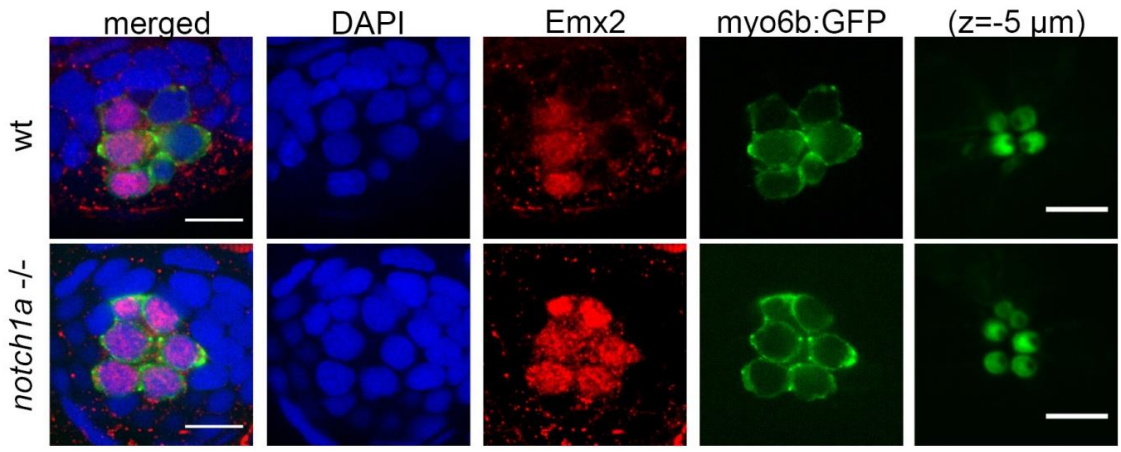

Figure 5.12: Emx2 immunostaining in *notch1a* mutants. (**A**) Immunohistochemical staining of horizontal neuromasts of wild type and *notch1a* mutant larvae in the transgenic line myo6b:GFP showing HCs in green, nuclei in blue (DAPI staining), and Emx2 in red (antibody staining). The scale bars in the far right panel showing hair bundles (z=-5 µm, with 2x magnification) are 5 µm, in all other panels, 10 µm (as in far left). wt – wild type. Figure 5.12 is published in Kozak et al., 2020.

5.2.4. Pharmacological inhibition of Notch signaling

All the hair cells of *notch1a* mutant larvae express Emx2 (Figure 5.12). Furthermore, the hair cells in *notch1a* mutant larvae are caudally orientated (Jacobo et al., 2019; Kozak et al.,

2020). However, this observation was in contrast to previously reported rostrad bias in hair cell orientation after a global pharmacological inhibition of Notch signaling (Mirkovic et al., 2012). To get better insights into this discrepancy, I first repeated the experiment published by Mirkovic et al. (2012) and observed the orientation of hair cells in larvae treated with DAPT. DAPT is a gamma-secretase inhibitor and thereby blocks the Notch signaling.

To assess the impact of DAPT on hair cell orientation, I analyzed the polarity of the hair cells in the DAPT treated larvae (Figure 5.13 A-B). More precisely, I incubated 2 dpf old, dechorionated embryos in 100 µM DAPT for 24 h and observed them 24 h later, by the time the hair cells, which were produced during the DAPT-treatment, fully matured. Importantly, the number of hair cells in the DAPT-treated neuromasts was abnormally high. This observation was not surprising because the impact of Notch signaling on neuromast hair cell number has been reported before (Wibowo et al., 2011). In addition, the quantification of the hair cell polarity revealed a bias with 70% of the hair cells with rostrad orientation (Figure 5.13 A). Note that the orientation of the hair cells was sparser, possibly due to space shortage. Furthermore, the immunostaining experiment revealed that the rostrad bias in hair cell orientation in the DAPT-treated larvae correlated with expression of Emx2 in 30% of cells, indicating that the impact of DAPT on the hair cell orientation is mediated through Emx2 (Figure 5.13 C). However, the surprising phenotype resulting from DAPT treatment remains to be fully understood. Notably, the orientation of hair cells in *notch1a* mutant larvae, treated with DAPT, was caudad, and all the hair cells expressed Emx2, showing that DAPT treatment did not block the Emx2 expression in the hair cells without Notch1a (Figure 5.13 B-C). Furthermore, the fraction of Emx2-expressing hair cells was affected by DAPT and Notch1a function, suggesting that Notch signaling affects hair cell orientation via Emx2 (published in Kozak et al., 2020).

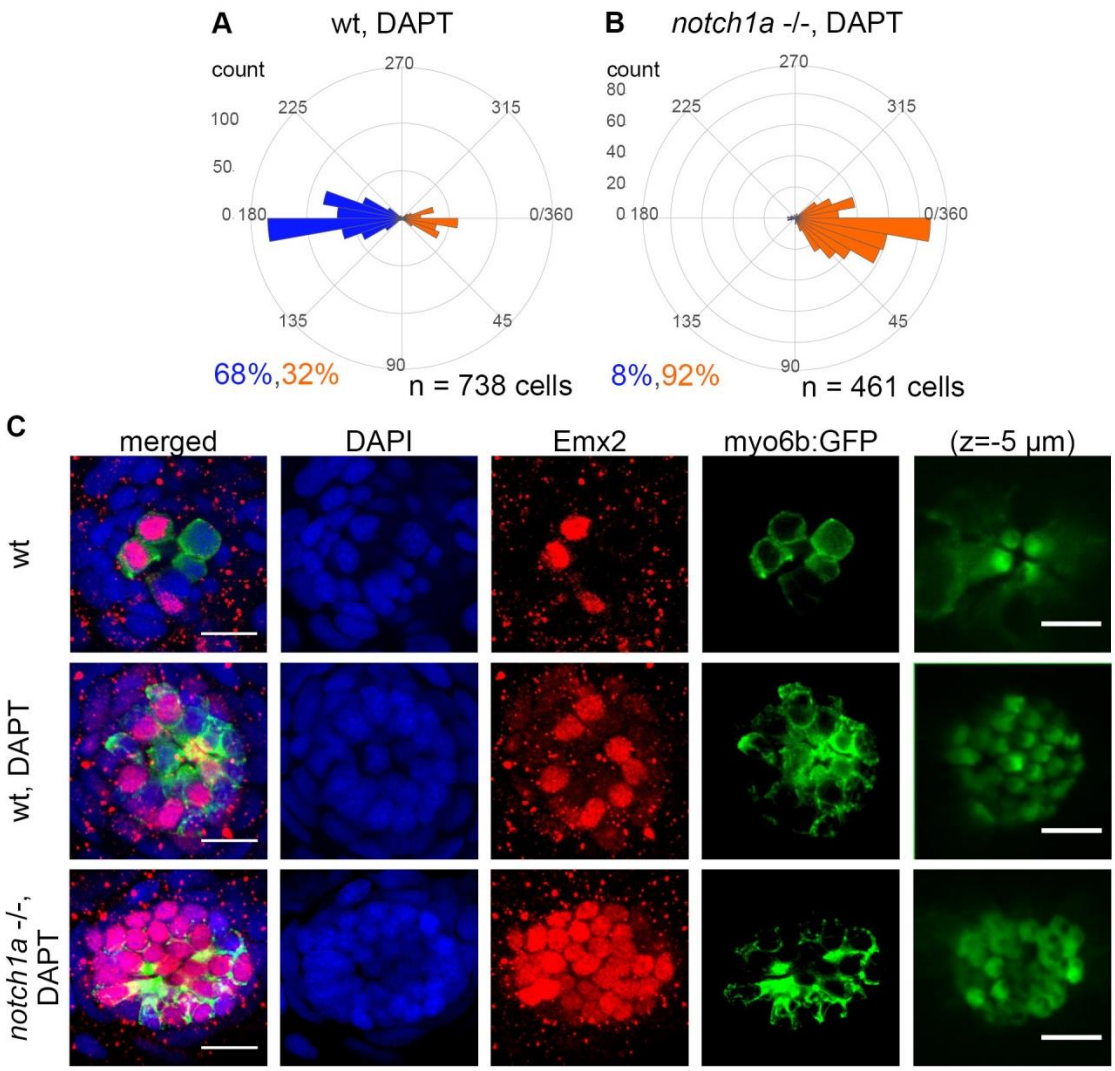

Figure 5.13: Analysis of HC orientation and Emx2 expression after DAPT treatment. (**A**-**B**) Stereociliary hair bundle orientations in the horizontal neuromast of the wild type (**A**) and *notch1a* mutant (**B**) larvae, treated with DAPT. The orientation of cells is depicted with circular histograms, 180° corresponding to the anterior direction in blue and 0/360° corresponding to the posterior direction in orange. The percentage of cells oriented in each direction is stated bottom left in each panel, with blue corresponding to rostrad and orange caudad direction. Note that the orientation of HCs in a wt control was inspected qualitatively. (**C**) Immunohistochemical staining of horizontal neuromasts in the wild type and wild type, treated with DAPT (n=20 neuromasts), and *notch1a* mutant, treated with DAPT (n=41 neuromasts), myo6b:GFP transgenic larvae. The transgenic line myo6b:GFP shows HCs in green, nuclei in blue (DAPI staining), and Emx2 in red (antibody staining) in 3-4 dpf larvae. Insets at the bottom left show the planar polarization of the hair cells, with z=-5 µm. The scale bars in the far right panel showing hair bundles (z=-5 µm, with 2x

magnification) are 5 µm, in all other panels, 10 µm (as in far left). wt – wild type, dpf – days post-fertilization. Figures 5.13 A, B, and selected panels of C (merged and z=-5 µm) are published in Kozak et al., 2020.

5.2.5. Misexpression of Notch1a intracellular domain

Knockout of *notch1a* gene results in opposite phenotype as pharmacological inhibition of global Notch signaling. Consequently, I set out to assess the role of Notch1a with another approach, namely by misexpression of Notch1a intracellular domain (NICD). In order to upregulate Notch1a signaling in hair cells only, I took advantage of the well-established UAS/Gal4 system (Scheer & Campos-Ortega, 1999). The UAS/Gal4 expression system is commonly used for cell-type or tissue-specific expression of transgenes and is described in chapter 4.5.2.1. To achieve a cell-type-specific NICD expression, I used the previously described transgenic line Tg(UAS:Notch1a-intra), later referred to as UAS:NICD (Scheer & Campos-Ortega, 1999). For the tissue-specific expression of Gal4, I set out to generate the myo6b:Gal4 transgenic line. In brief, I injected the myo6b:Gal4 plasmid and the transposase mRNA into a single cell stage UAS:GFP embryos. Next, the injected embryos were raised to adulthood under standard conditions, and their progeny was screened for successful integration of the transgene in the genome. When the carrier fish reached adulthood, the myo6b:Gal4 were crossed to UAS:NICD fish. Finally, I analyzed the hair cell orientation in the double transgenic line myo6b:Gal4, UAS:NICD. To this end, I stained the hair cell bundles of the 3-4 dpf larvae. Surprisingly, the hair cells in the transgenic line myo6b:Gal4, UAS:NICD did not fully mature, but the immature hair cells were visible and the immunostaining analysis revealed that those cells did not express Emx2 (Figure 5.14).

Nevertheless, the orientation of hair cells in the myo6b:Gal4, UAS:NICD transgenic line was not visible. I reasoned that the expression of NICD in the UHCPs interferes with the differentiation of hair cells. To overcome this obstacle, I analyzed the hair cell orientation in brn3c:Gal4, UAS:NICD double transgenic larvae, which I generated with a cross of UAS:NICD and Tg(pou4f3:GAL4) – referred to as brn3c:Gal4 – transgenic lines, both previously described (Scheer & Campos-Ortega, 1999; Xiao & Baier, 2007). Importantly, in the brn3c:Gal4, UAS:NICD transgenic line, the NICD expression occurs later in the differentiation process at the stage of the young hair cells as opposed to UHCPs. The hair cells in the double

transgenic line brn3c:Gal4, UAS:NICD successfully matured as visible from their hair bundle formation. To analyze the orientation of the hair bundle in the brn3c:Gal4, UAS:NICD larvae, I stained the hair bundles with phalloidin. The analysis revealed that the hair cells in the brn3c:Gal4, UAS:NICD transgenic line predominantly oriented rostrally and did not express Emx2 (Figure 5.14).

In summary, the misexpression of NICD in the hair cells results in them not expressing Emx2 and possessing rostrad orientation. Notably, the expression of NICD results in the opposite phenotype of *notch1a* mutants, confirming that Notch1a is involved in establishing rostrad orientation (published in Kozak et al., 2020).

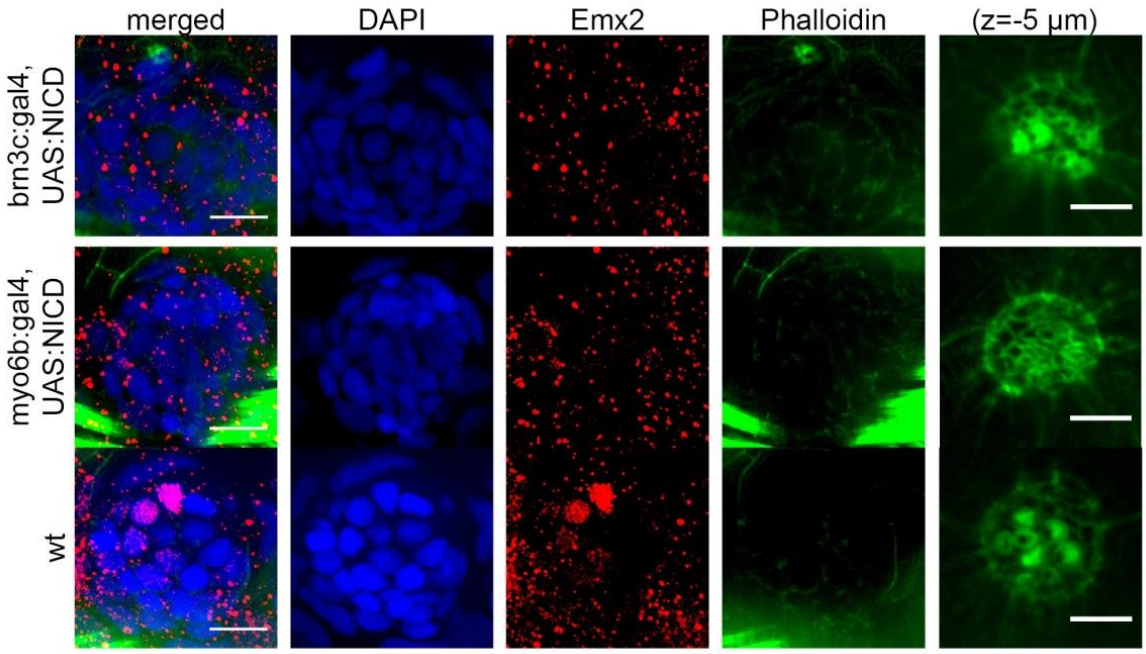

Figure 5.14: Emx2 immunostaining in NICD misexpressing larvae. Immunohistochemical staining of horizontal neuromasts of brn3c:gal4, UAS:NICD (n=10 neuromasts), myo6b:gal4, UAS:NICD (n=10 neuromasts), and wild type 3dpf larvae, showing nuclei in blue (DAPI staining) and Emx2 in red (antibody staining) and hair bundles in green (phalloidin staining). The scale bars in the far right panel showing hair bundles (z=-5 µm, with 2x magnification) are 5 µm, in all other panels, 10 µm (as in far left). wt – wild type, dpf – days post-fertilization. Selected panels of Figure 5.14 (merged and z=-5 µm) are published in Kozak et al., 2020.

5.2.6. Analysis of HC orientation in *notch1a*, *emx2* double mutant larvae

The experiments involving genetic and pharmacological interventions suggested that Notch1a impacts hair cell orientation via Emx2. To corroborate these findings, I evaluated the orientation of the hair cells in horizontal neuromasts in e*mx2*, *notch1a* double mutant larvae (Figure 5.15 A-D). In wild type larvae, the hair cells in horizontal neuromasts were oriented in rostrad (50%) and caudad (50%) direction (Figure 5.15 A), in e*mx2* mutant larvae, the hair cells had rostrad orientation (Figure 5.15 B), in *notch1a* mutant larvae, the hair cells had caudad orientation (Figure 5.15 C). To analyze the orientation of hair cells in *notch1a*, *emx2* double mutant larvae, I performed somatic mutagenesis of e*mx2* gene in *notch1a* mutant line using a redundant sgRNA targeting approach (Varshney et al., 2015; R. S. Wu et al., 2018). I *in vitro* transcribed four sgRNAs, binding to e*mx2* gene, and injected them together with Cas9 protein into the one-cell stage embryos of the myo6b:GFP, *notch1a* mutant line, and wild-type myo6b:GFP line as control. The injected and non-injected control embryos were grown in standard conditions until day 3, when I identified the *notch1a* homozygous larvae by observing the previously reported phenotype of disordered somites (Gray et al., 2001), and in addition, separated the sibling control larvae. I evaluated the hair cell polarity in myo6b:GFP positive larvae of all sample groups: (I) non-injected wild-type, (II) injected wild-type (e*mx2* mutant), (III) non-injected *notch1a* mutant, and (IV) injected *notch1a* mutant (*notch1a*, e*mx2* double mutant). Confirming the efficiency of the method, more than 90% of the hair cells in the larvae from the injected wild-type control group were oriented towards the anterior side. Notably, I discovered the majority of the hair cells in *notch1a*, e*mx2* double mutant larvae possessed rostrad orientation (Figure 5.15 D). Thus, this analysis unambiguously confirmed that Notch1a controls hair cell orientation via Emx2 (published in Kozak et al., 2020).

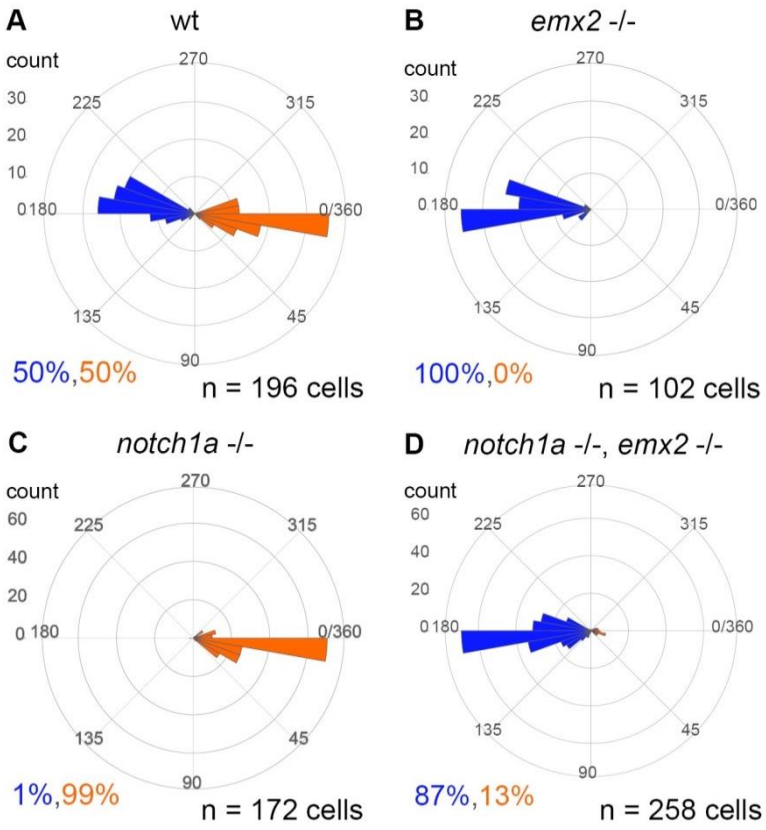

Figure 5.15: HC orientation quantification in wt and mutant larvae. Stereociliary hair bundle orientations in the horizontal neuromast of the wild type, n=24 neuromasts (**A**), e*mx2* mutant, n= 18 neuromasts (**B**), *notch1a* mutant, n=18 neuromasts (**C**), and double e*mx2*, *notch1a* mutant n=51 neuromasts (**D**). The orientation of cells is depicted with circular histograms, 180° corresponding to the anterior direction in blue and 0/360° corresponding to the posterior direction in orange. The percentage of cells oriented in each direction is stated bottom left in each panel, with blue corresponding to rostrad and orange caudad direction. wt – wild type. Figure 5.15 is published in Kozak et al., 2020.

5.3. Analysis of Emx2 expression in nascent hair cells

To gain new insights into the initial step of the establishment of the planar bipolar epithelium, I inspected the expression of Emx2 in nascent hair cells (Figure 5.16). Note that it has been previously established that Emx2 is expressed in half of the hair cells (Figure 5.9). Importantly, the Emx2-expressing cells are oriented caudally and are located on the more anterior side. The anterior localization of the Emx2-positive cells is evident in the young neuromasts populated with only 6 or 8 hair cells. In the young neuromasts, the pairs of the

hair cells are positioned in an ordered manner, with each pair of the cells facing each other, thereby forming a mirror-symmetric image of the whole organ with a line of polarity reversal in the middle. For this reason, individual pairs of hair cells can be identified.

The immunostaining analysis confirmed that the Emx2-expressing hair cell is always positioned on the anterior side of the HC-couple, which is in line with the fact that Emx2 is expressed by caudad-oriented hair cells. Importantly, I observed exceptions to this rule when observing the nascent hair cells (Figure 5.16 A). Intriguingly, among the nascent hair cell couples, which are still immature and do not yet possess hair cell bundles (Figure 5.16 B), the Emx2-expressing cell was located either on the anterior or posterior side of the couple (Figure 5.16 A, C).

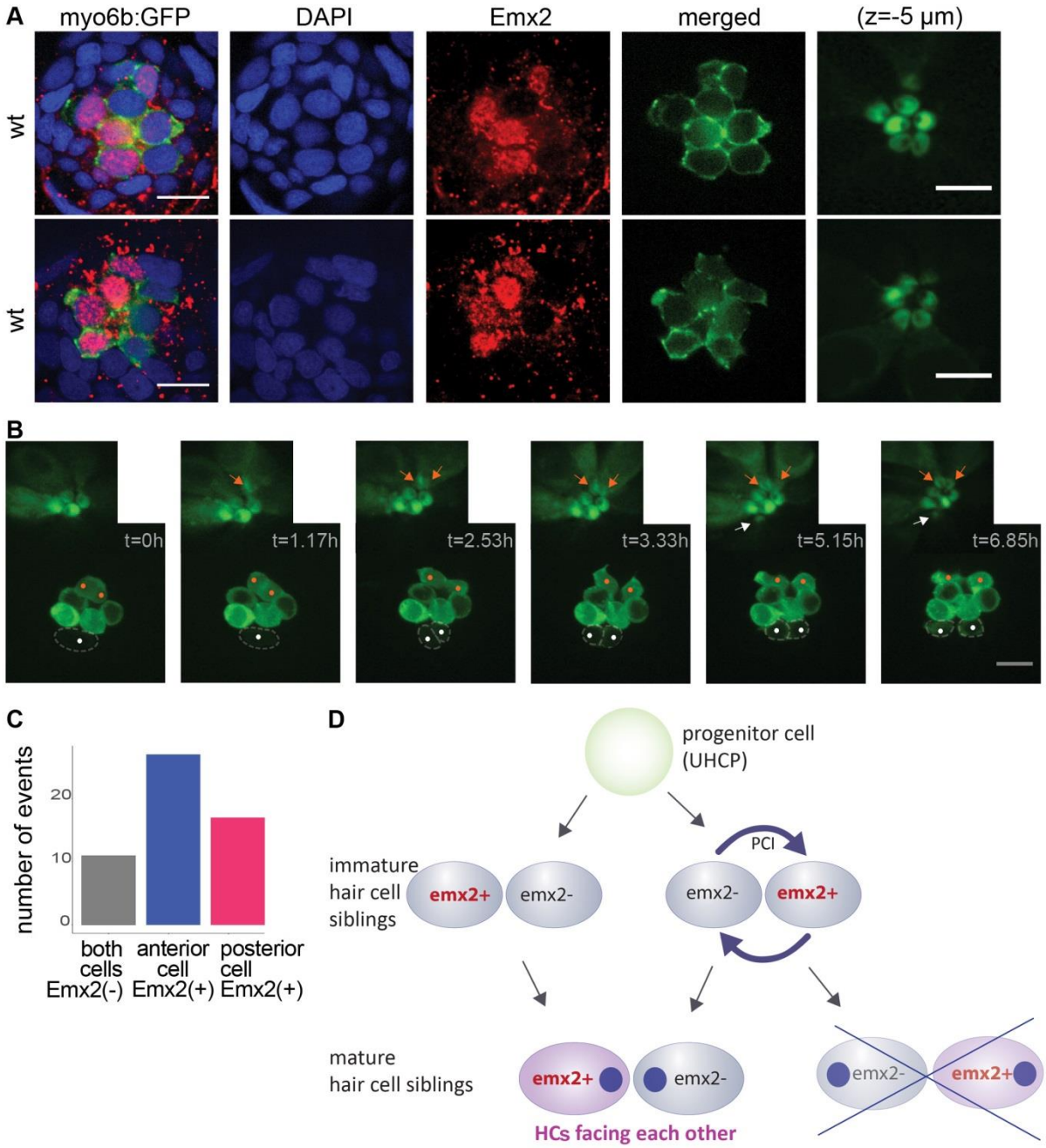

Figure 5.16: Stochasticity of Emx2 expression. (**A**) Immunohistochemical staining of horizontal neuromasts in the wild type, myo6b:GFP transgenic 2dpf larvae, showing HCs in green, nuclei in blue (DAPI staining), and Emx2 in red (antibody staining). The scale bars in the far right panel showing hair bundles (z=-5 µm, with 2x magnification) are 5 µm, in all other panels, 10 µm (as in far left). (**B**) Selected frames from a 6.85-hour time-lapse movie of a myo6b:GFP horizontal neuromast with strongly green-fluorescent hair cells and a weakly fluorescent UHCP (white dot). Note that 2.53 hours after the movie starts, a UHCP divides into a pair of nascent hair cells, which mature during the following 4.32 hours (white dots).

An earlier pair of hair cells is labeled with orange dots. The image series shows that the green fluorescence in myo6b:GFP transgenic line first appears in UHCPs. Moreover, the arrows in the top left images, showing hair bundles (z=-5 µm), highlight the first stages of the formation of hair bundles in hair cells, which was used to estimate the immature hair cells' age. The nascent hair cells were defined as GFP-expressing cells since the division of the UHCP until the kinocilium becomes visible in myo6b:GFP transgenic line; see the far right panel. The scale bar is 10 µm, with 2x magnification in the additional top left images. (**C**) Quantification of events, when the Emx2 was detected in the anterior or posterior, or it was not detected in the nascent sibling hair cells. Only the nascent hair cells (estimated maturity) were used for the quantification. The number of pairs of nascent hair cells analyzed n= 55. (**D**) Model: the role of planar cell inversions in correcting the stochastic relative position of *emx2*-expressing and *emx2*-non-expressing nascent sibling hair cell. wt – wild type, UHCP – unique hair cell progenitor, HCs – hair cells, GFP – green fluorescent protein, dpf – days post-fertilization, PCI – planar cell inversion. Figures 5.16 A-C are published in Kozak et al., 2020.

Altogether, these results indicate that the symmetry breaking of *emx2* expression to only one of the sibling hair cells is stochastic because the relative position of the *emx2*-expressing cell in the sibling cell pair is not predetermined. Therefore, the Notch1a-mediated symmetry breaking of *emx2* expression is a stochastic event (published in Kozak et al., 2020).

Further, I reasoned that the pairs of nascent hair cells in which the more posterior cell was Emx2-positive are the pairs, which would later undergo a planar cell inversion. In addition, the pairs of nascent hair cells, in which the more anterior cell was expressing Emx2, would not undergo a planar cell inversion. Intriguingly, this raises the question if the planar cell inversions take place in *emx2*-mutant larvae as well and if the process of planar cell inversions is disrupted or altered when the emx2 asymmetry is eliminated. Consequently, I next analyzed the process of planar cell inversions.

5.4. Planar cell inversions

Planar cell inversions are fascinating phenomena of nascent sibling hair cells rotating around each other. Following the division of unipotent hair cell progenitor (UHCPs), the sibling pair

of nascent hair cells sometimes undergoes rearrangements when both cells rotate about the axis through their interface, thereby exchanging their positions (Mirkovic et al., 2012; Wibowo et al., 2011). However, it is not understood how or why these rearrangements occur and if they contribute to the formation of the bipolar planar epithelium. My previous results suggested that the symmetry breaking of emx2 expression between sibling hair cells is stochastic, indicating that it occurs before the planar cell inversions take place (see also chapter 5.3). Emx2 or its asymmetry could play a role in this process. The planar cell inversions are, in general, very poorly understood. Therefore I set out to characterize the PCI process and test the importance of Emx2 asymmetry for the planar cell inversions.

To this end, I took advantage of live high-resolution video microscopy. In particular, I observed the production of new hair cells and cellular movements by taking consecutive images of neuromasts for more than 24h. I observed the production of new hair cells and their rearrangements in the transgenic line myo6b:GFP in which hair cells (and less intensely the UHCPs) are labeled with a green fluorescent protein, and the polarity of the hair cells is clearly visible. I also observed the cells in myo6b:GFP, alpl:nlsEGFP and myo6b:GFP, cldnb:GFP larvae to visualize all cells in a neuromast. Specifically, 2-3 dpf old larvae of the transgenic lines were anesthetized with MS-222, mounted in 1% agarose, and bathed in E3 medium with MS-222. I took an image of a neuromast every 2-4 minutes for up to 40h. Afterward, I reconstructed the time-lapse movies and analyzed the cellular movements in Fiji (Schindelin et al., 2012).

5.4.1. Analysis of cellular movements in the whole neuromast

5.4.1.1. Generation of alpl:nlsEGFP transgenic line

The planar cell inversions have been reported as cellular rearrangements of two nascent sibling hair cells (Wibowo et al., 2011). Nevertheless, the movements of other cells in a neuromast have not been sufficiently characterized. Rotational movement could be characteristic also of other neuromast cells, or their migrations could contribute to the planar cell inversions of nascent hair cells. Therefore, I investigated whether there is any collective cellular movement in the neuromast during the process of inversion.

In order to visualize all the cells in a neuromast, I first generated a transgenic line

alpl:nlsEGFP. The line generation consisted of three main steps. The first step included the cloning, the second step injections of the embryos, and the third step screening of fish and establishment of a stable transgenic line. Briefly, I took advantage of the Tol2/Gateway zebrafish cloning kit (Kwan et al., 2007) and cloned 5kb of alpl promoter to generate p5E-alpl. p5E-alpl, pME-nlsEGFP, p3E-polyA, and the donor plasmid 394 were ligated in an LR reaction into alpl:nlsEGFP-polyA plasmid, which was injected into one-cell stage wild type embryos together with transposase mRNA. The embryos were raised to adulthood in standard conditions, and after identifying a carrier fish, F3 larvae were used for videomicroscopy. Therefore, a new transgenic line alpl:nlsEGFP was established (published in Kozak et al., 2020).

In the Tg(alpl:nlsEGFP) transgenic line, the nuclei of neuromast cells are labeled with a green fluorescent protein (Figure 5.17), in contrast to the previously described alpl:mCherry line (Steiner et al., 2014), where only the mantle cells are labeled. The reason for different patterns could be in a slightly shorter sequence of the promoter or in the random integration place of the transgene in the genome. Interestingly, when studying the pattern of alpl:nlsEGFP line, distinct patterns were observed, one of them having labeled only a subset of mantle cells (Figure 5.17 B). Nevertheless, the alpl:nlsEGFP pattern E line was not established, but the alpl:nlsEGFP pattern A line Tg(alpl:nlsEGFP) was established for analysing the cellular movements of all the cells in the neuromast.

Altogether, the generation of a new transgenic zebrafish line with labelled neuromast cells was successful.

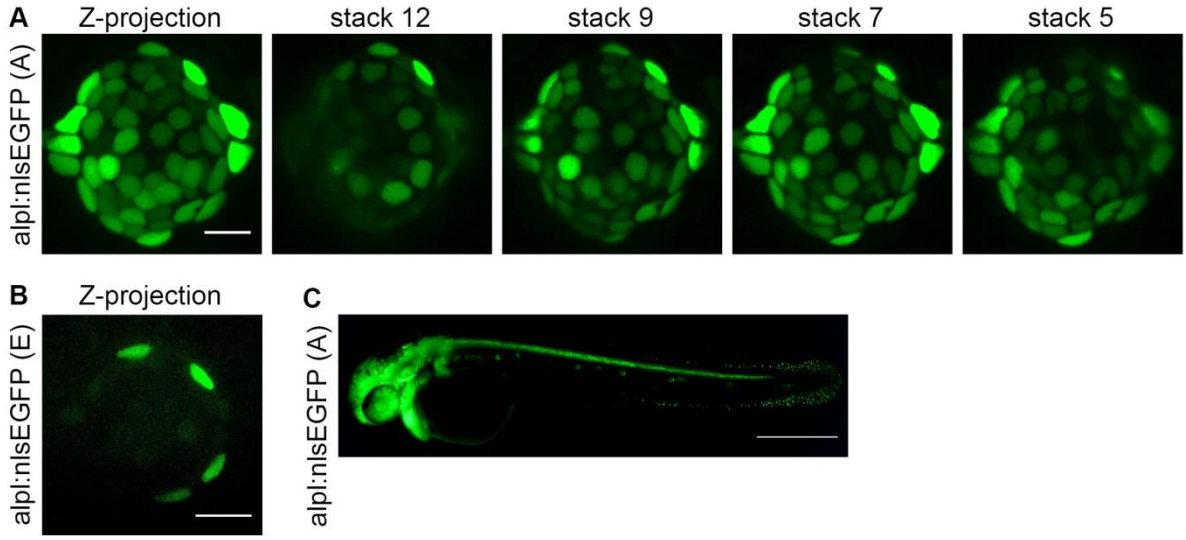

Figure 5.17: alpl:nlsEGFP transgenic line. (**A**) Image of a horizontal neuromast of the Tg(alpl:nlsEGFP) transgenic line (A refers to the pattern A, used for line establishment). Z-projection in the far left panel and selected stacks (1 µm between consecutive stacks) in other panels. Note that the fluorescence intensity is not uniform in all the cells, but all the neuromast cells are visible. The scale bar is 10 µm. (**B**) Z-projection of a horizontal neuromast of the alpl:nlsEGFP pattern E observed in the F1 generation. The scale bar is 10 µm. (**C**) 2 dpf old larva of the Tg(alpl:nlsEGFP) transgenic line, scale bar is 500 µm. dpf – days post-fertilization.

5.4.1.2. Pair-wise analysis of all neuromast cells' movements

To quantitatively confirm the observation that the planar cell inversions are characteristic for nascent hair cells only, and to analyze if the cellular movements of other neuromast cells contribute to the planar cell inversions of nascent hair cells, I analyzed the rotational movements of all neighboring pairs of cells in a neuromast.

In brief, I first generated time-lapse movies of neuromasts from alpl:nlsEGFP, myo6b:GFP and alpl:nlsEGFP, myob6:GFP, cldnb:GFP transgenic lines, selected cell neighbors, and tracked the positions of all cells in time in order to obtain high-quality data describing positions of individual cells in respect to time (Figure 5.18 A). All neighboring cell pairs, regardless of their origin and cell type and filtered only by their initial proximity, were taken into analysis. For each pair, the angle between the line connecting the cells and the anterior-

posterior axis was calculated at each time point, and subsequently, the change in angle per time unit was calculated. Positional angle change was defined as the sum of rotational direction aware angle changes between individual frames and served as a proxy of directed cell movement (Figure 5.18 B, upper left). In order to better estimate the coordination of the movement of cell pairs, I also analyzed rotation consistency, estimated by the ratio between positional angle change and absolute positional angle change (Figure 5.18 B, upper right), the latter being a measure of noise in the movement that does not contribute to the final rotation. Interestingly, when plotted against the positional angle change, this parameter allows for good separation of the nascent hair cells (Figure 5.18 C). The position of nascent hair cells that perform PCI at the far sides of the diagonal strongly suggests that the behavior of these cells is coordinated and is not a result of noise originating from random cell movements.

Interestingly, the pair-wise analysis of the movement of all neuromast cells revealed also a handful of cell-pairs not consisting of nascent hair cells that performed a rotational rearrangement, indicating that behavior, resembling PCI of nascent sibling HCs, is possible in other cell types as well (Figure 5.18 C).

In summary, the analysis of the pair-wise cellular movements of all the cells in a neuromast during the PCI of nascent HCs showed no collective cell movement of the whole tissue. Furthermore, the rotational movement of nascent sibling HCs during the PCI is a coordinated movement.

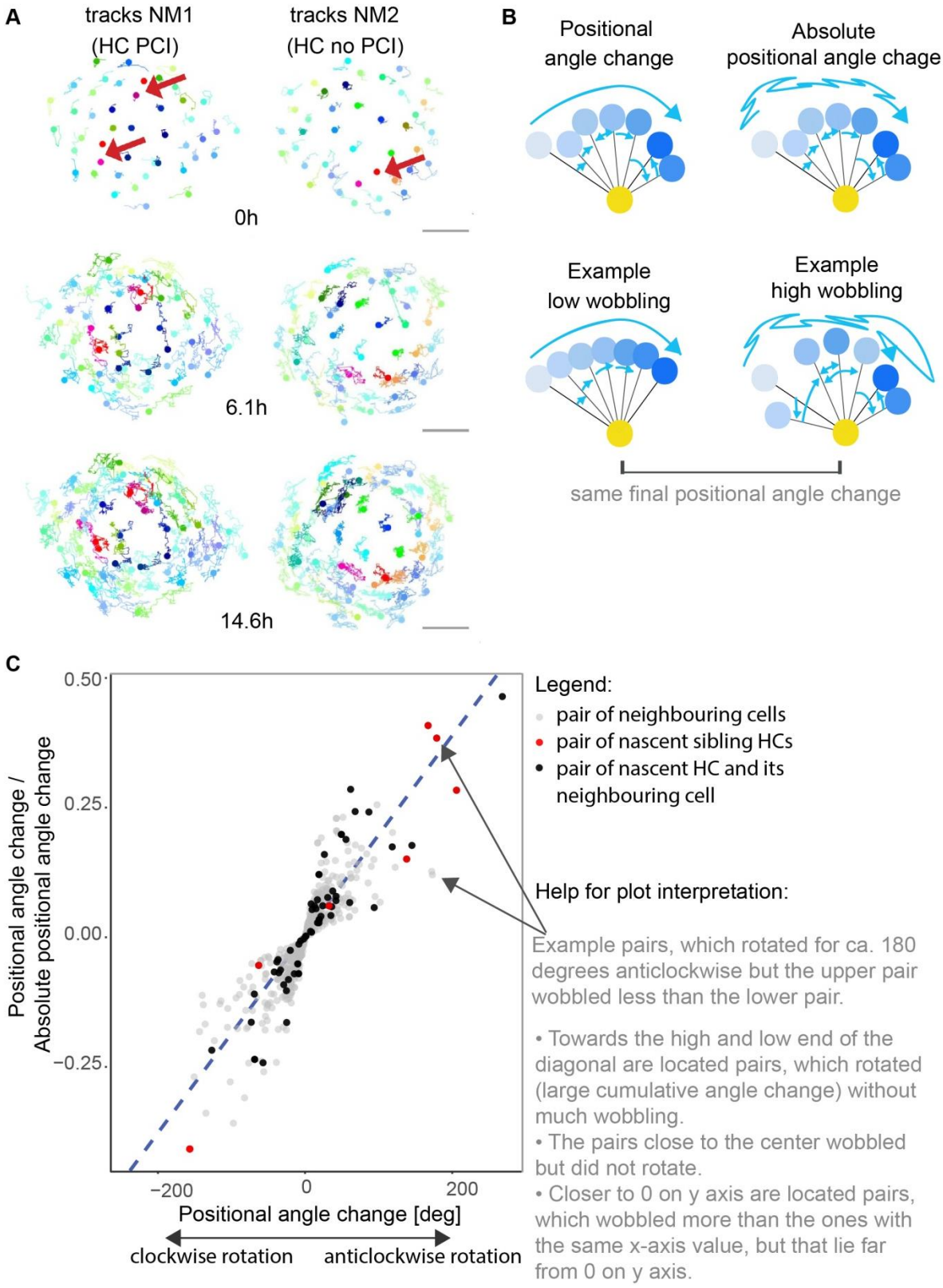

Figure 5.18: Pair-wise analysis of all neuromast movements. (**A**) Cell tracks of two exemplary neuromasts at selected times: 0, 6.1h, and 14.6h. Each dot corresponds to a center of a neuromast cell, with a thin line depicting its position in previous frames. The new pairs of hair cells (undergoing PCI in NM1, not undergoing PCI in NM2) are highlighted with

red arrows. Scale bars are 10 µm. (**B**) Schematic explanation of the difference between the positional angle change (upper left) and the absolute positional angle change (upper right), illustrated with the path of the blue arrow. Below are two examples of pairs with the same positional angle change and relatively low and high wobbling. The yellow and blue dots present a pair of cells, where the lighter shade of blue signifies the position of the blue cell at an earlier time point. (**C**) Scatter plot showing the ratio of positional angle change divided by absolute positional angle change as a measure of the direct rotation and wobbling. The position of HC pairs at far ends of the diagonal strongly indicates larger positional angle changes and, importantly, a higher degree of coordinated movement in the behavior of nascent HCs vs. other cell pairs in a neuromast. On the right, there are notes to facilitate interpretation. NM – neuromast, HCs – hair cells.

5.4.2. Analysis of the planar cell inversions in wt and *emx2* mutant larvae

Emx2 is a transcription factor expressed in only one of the two sibling hair cells. It is necessary and sufficient to determine the orientation of a hair cell (T. Jiang et al., 2017). The results of this thesis have shown that in mature hair cells, Emx2 is expressed in the anteriorly positioned sibling HC. However, among the nascent hair cells, the relative position of the sibling hair cell expressing Emx2 is random. As these results indicate that the planar cell inversions take place to position the Emx2-expressing cell on the anterior side, is Emx2 itself also a possible candidate to play a role in planar cell inversions (see also Figure 5.16).

To determine whether loss of Emx2 has an impact on planar cell inversion process, I performed live videomicroscopy of *emx2* mutant, myo6b:GFP larvae and control wt, myo6b:GFP larvae and compared the movements of nascent hair cells in movies, reconstructed using Fiji (Schindelin et al., 2012). Part of the time-lapse movies of the control wt larvae was generated in collaboration with Dr. Jerónimo Roberto Miranda Rodríguez (Hernán López-Schier lab, Research Unit Sensory Biology and Organogenesis, Helmholtz Zentrum München). Surprisingly, I observed that the planar cell inversions occur not only in wild-type but also in *emx2* mutant larvae (Figure 5.19 A-B). Therefore, the Emx2 transcription factor is not critical for the PCI process to take place. Moreover, the Emx2 asymmetry and the later acquired opposite polarities are dispensable for the PCI process to occur.

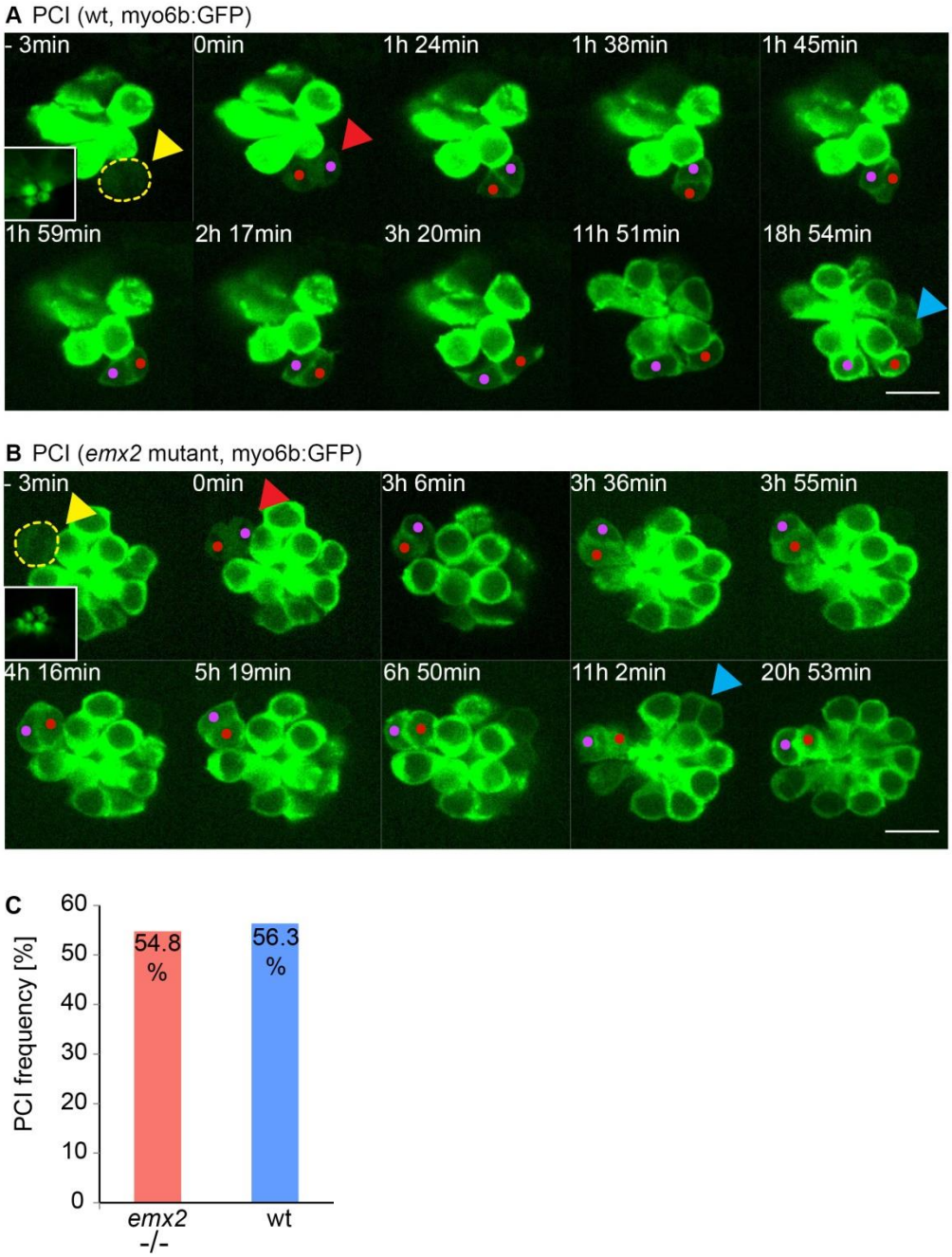

Figure 5.19: PCI in wt and emx2 mutants. Selected frames from movies of a horizontal neuromast in 2-3 dpf myo6b:GFP wild type (**A**) and *emx2* mutant **(B**) larvae. The hair cells and (weakly) the UHCP are labeled in green. Note that the mature hair cells are oversaturated due to higher GFP expression in these cells. The UHCP is outlined with a dashed yellow line in the first frame (-3 min, yellow arrowhead). The inset in the first frame shows the hair cells bundles (z=-5 µm). The division is (0 min) is highlighted with a red arrowhead. The two sibling hair cells are labeled with red and violet dots. Note that the two cells exchange their positions during the movie by rotating around each other. Another pair of sibling hair cells has been produced towards the end of the movie (blue arrowhead). In

the last frames the two analysed hair cells have already matured. The scale bars are 10 µm. (**C**) Frequency of PCI occurrence among the nascent sibling hair cell pairs in wt (n=72) and *emx2* mutant (n=42) larvae. PCI – planar cell inversion, wt – wild type, GFP – green fluorescent protein, UHCP – unique hair cell progenitor, dpf – days post-fertilization.

I quantified the frequency of planar cell inversions in wt and *emx2* mutant larvae. To this end, I defined an inversion as a final change in the angle of the line through the center of both cells with an x-axis larger than 90 degrees. Intriguingly, I discovered that around half of nascent sibling HCs undergo PCI in both genotypes (56.3 % in wild-type and 54.8 % in *emx2* mutant larvae). Even though the PCI was suggested to take place in order to position the Emx2-expressing sibling on the anterior side, the process also occurs without Emx2 or its downstream effectors.

Next, to characterize the PCI process and find out if the dynamics of the PCI in *emx2* mutant larvae differ from those in wild-type larvae, I analyzed several aspects of the PCI process and compared the parameters between both genotypes.

First, I generated plots of angular position in time for all the analyzed sibling HC pairs to obtain a general overview of the process (Figure 5.20 A-F). I set out to analyze when the distinct phases of PCI occur in wild-type and *emx2* mutant larvae. However, neither by directly observing the time-lapse movies nor from the radial plots of positional angle in time was it possible to unbiasedly determine when the PCI starts and ends in all HC pairs. To overcome this, I fitted a sigmoid curve to the tracking data of inverting HC pairs using R 4.0.2 (R Core Team, 2020) (Figure 5.20 G-L). This allowed me to unbiasedly determine the onset and the termination of the PCI (Figure 5.20 G-L).

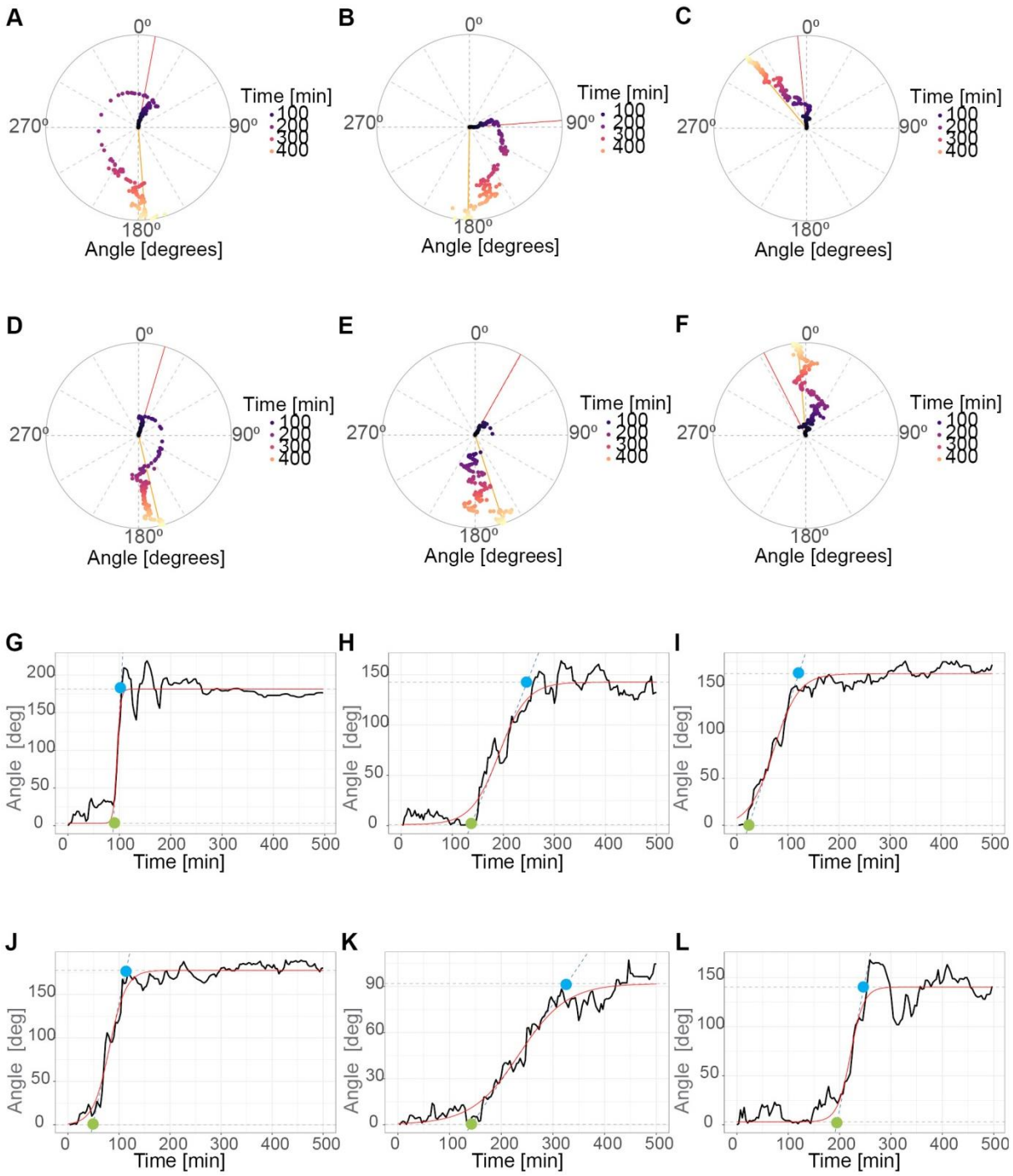

Figure 5.20: Examples of positional angle change in sibling HC pairs. Radial plots showing the positional angle change vs. time for exemplary HC pairs from wild type (**A**-**C**) and *emx2* mutant larvae (**D**-**F**). (**A**-**F**) Each plot presents one sibling HC pair plotting the positional angle change in time. Time 0 corresponds to the first frame in which the hair cell siblings appeared, and the positional angle at that time is highlighted with a red line, the positional angle in the last frame is highlighted with a yellow line. The time increases from the center of the circle towards the periphery with the color code in the legend. For each genotype

(wild type and *emx2* mutant), one example of non-inverting HCs (**A** and **C**, respectively) and 2 examples of inverting HCs (**A**-**B**, wild type, and **D**-**E**, *emx2* mutant) are shown. (**G**-**L**) Plots of positional angle vs. time with a fitted sigmoid curve for exemplary HC pairs. The sigmoid curve is visible in red. Respectively, green and blue dots correspond to the onset and termination of PCI. Only the plots for selected HC pairs are shown. The label Angle signifies the positional angle of the HC pair. wt – wild type, deg – degrees, mut – mutant, PCI – planar cell inversion.

The unbiased approach of fitting a curve to the line, depicting the positional angle change in time, has proven fruitful. In particular, the time of the onset was defined as the time corresponding to the interception of the initial positional angle asymptote and the maximum derivative of the fitted curve, going through the inflection point of the same curve (green dots on the plots in Figure 5.20 G-L). Similarly, the time of the PCI termination was determined as the time corresponding to the interception of the final positional angle asymptote and the maximum derivative of the fitted curve, going through the inflection point of the same curve (blue dots on the plots in Figure 5.20 G-L). Importantly, the time of the onset and termination of PCI were analyzed only in the HC pairs undergoing a PCI (final positional angle change more than 90 degrees). The onset and the termination of PCI were determined in the same way for the HC pairs from wild-type and *emx2* mutant larvae.

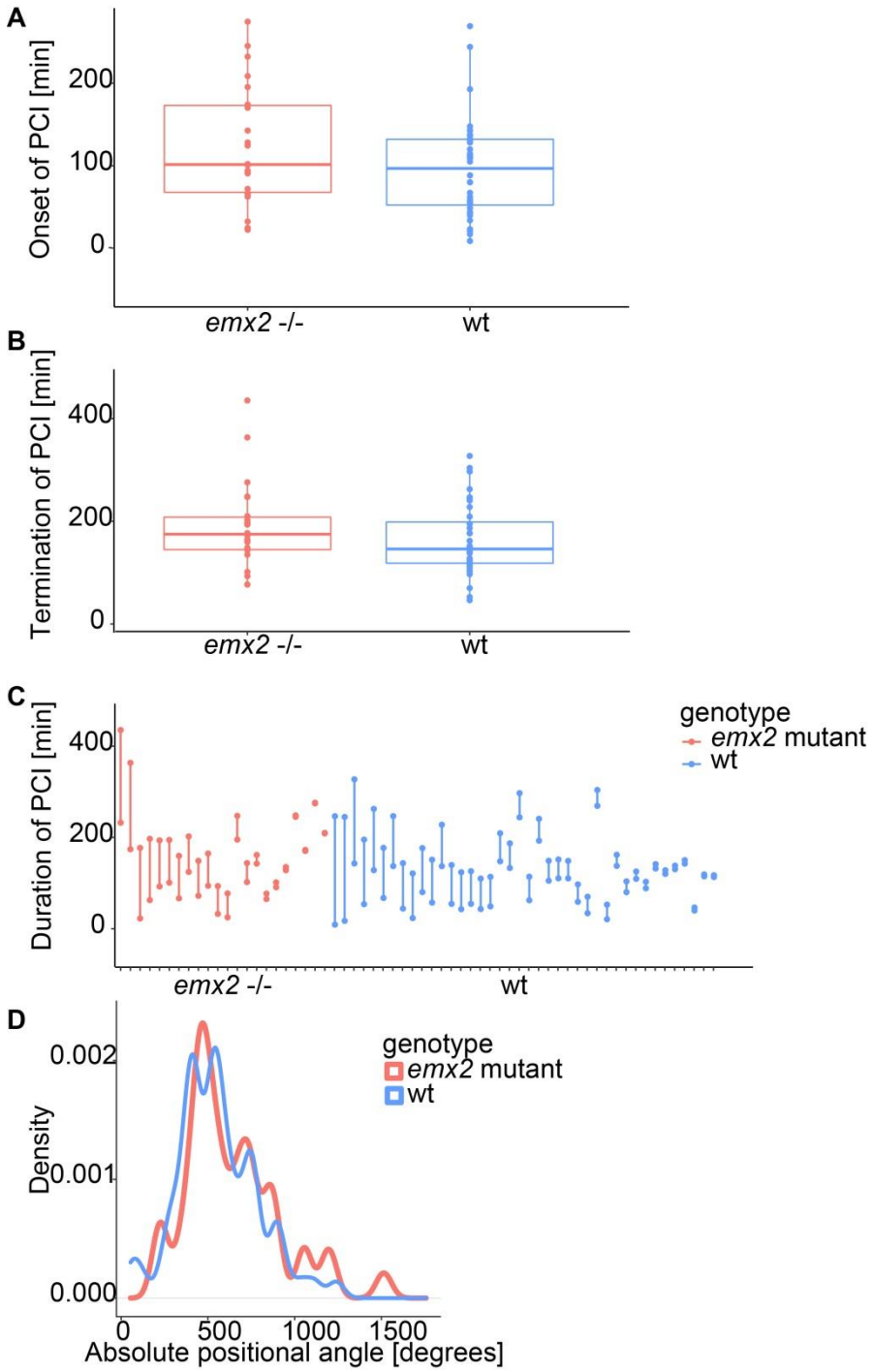

Figure 5.21: PCI dynamics in wt and emx2 mutant larvae. (**A**) The time of the PCI onset, (**B**) the time of the PCI termination, and (**C**) the duration of PCI in wild type (blue) and *emx2* mutant (red) larvae. Only the pairs undergoing PCI were analyzed (wild type, n=40, and *emx2* mutant, n=23). The comparison was performed with a two-sample t-test, revealing no significant differences between wild type and *emx2* mutants. For the determination of onset and termination, see Figure 5.20. The extent of wobbling is reflected in the absolute

positional angle change, shown in (**D**). wt – wild type, mut – mutant, HC(s) – hair cell(s), deg – degrees.

The comparison of the time of PCI onset and termination revealed no significant difference between the HC pairs from wild type and *emx2* mutants, indicating that the lack of Emx2 has no impact on the PCI dynamics. Nevertheless, since incomplete and double inversions have been observed in planar polarity mutant (Mirkovic et al., 2012), I also quantified how much the cells wobble in both genotypes. No significant difference between HCs from *emx2* mutants and wild types was shown (Figure 5.21 D).

Finally, I compared the final positional angle of HC pairs in wild type and *emx2* mutant larvae to find out if the hair cell pairs align with the planar polarity axis. Importantly, the HC pairs in planar polarity mutant (*vangl2* mutant) fail to align with the planar polarity axis after inverting, which may contribute to their random hair cell orientation phenotype (Mirkovic et al., 2012). To determine if the alignment of HC pairs with the PCP-axis is affected in *emx2* mutants, I analyzed their final positional angle. The analysis revealed that the final angular position of the HC sibling pair relative to the PCP-axis (x-axis) was indistinguishable in wild type and *emx2* mutant larvae as the sibling hair cell pairs of both genotypes finally aligned with the planar polarity axis (Figure 5.22). Moreover, the analysis revealed that the final alignment of HC pairs with the PCP-axis is independent of the initial positional angle of the HC pair (Figure 5.22 B). Importantly, the final alignment of HC pairs with PCP-axis results from the positional rearrangements (including PCI) of the sibling hair cells as the pairs, dividing parallel to the PCP-axis tend to invert for about 0^{o} or 180^{o}, but pairs arising perpendicular to the PCP-axis tend to invert for about 90^{o} (Figure 5.22 C).

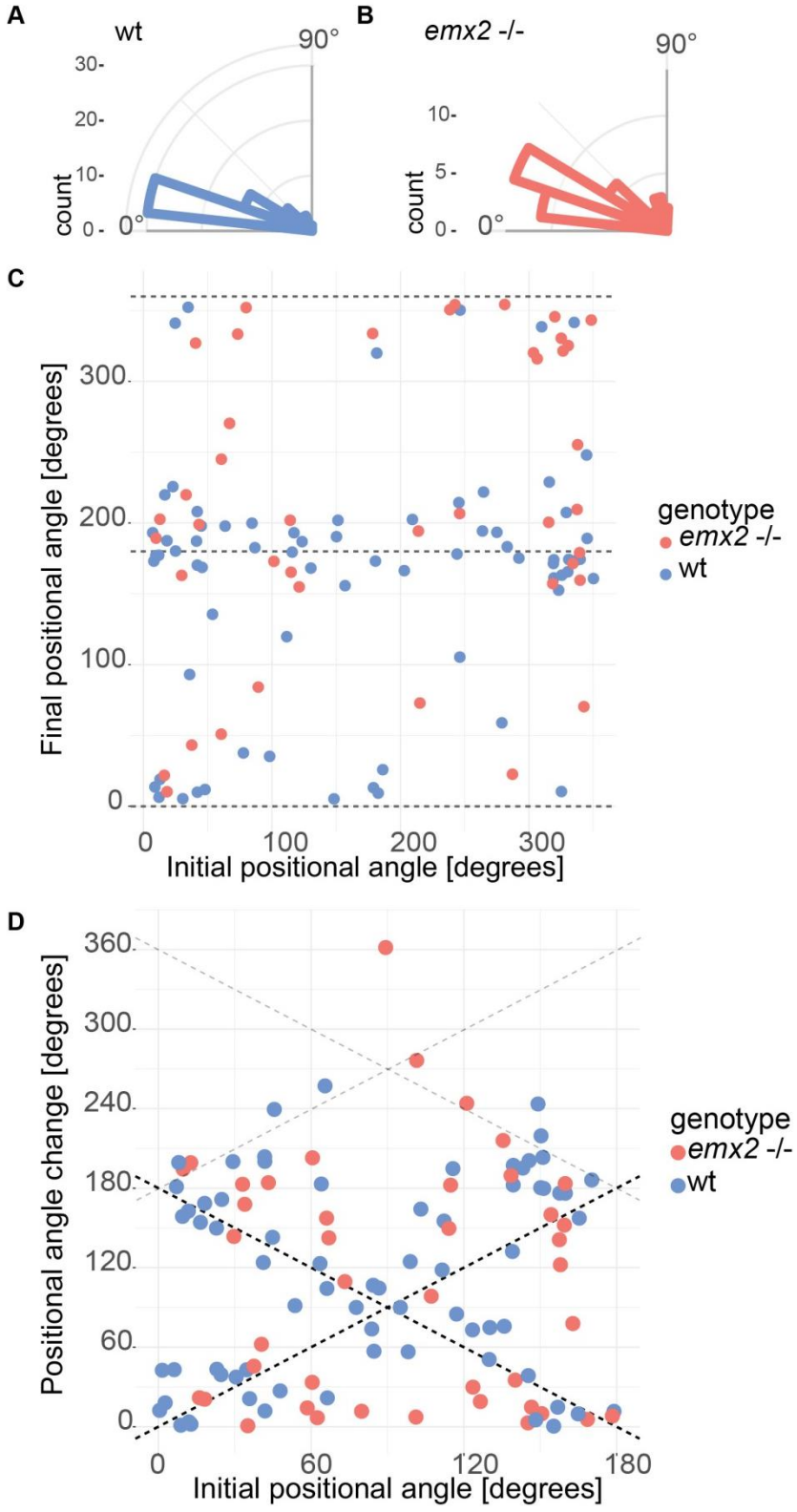

Figure 5.22: Initial and final angular positioning of HC pairs. (**A-B**) Circular histograms are showing the final angle position of sibling HC pairs after they stopped rearranging (500 min after production) in wt (**A**) and *emx2* mutant (**B**) larvae. The horizontal distribution shows the alignment with the x-axis (planar cell polarity axis in horizontal neuromasts). (**C**) Final

positional angle vs. initial positional angle of HC pairs in wt (blue) and *emx2* mutant (red) larvae. Note that the final positional angles around 0^o, 180^o, or 360^o correspond to the final alignment of HC pair with the PCP-axis. (**D**) Positional angle change vs. initial positional angle of HC pairs in wt (blue) and *emx2* mutant (red) larvae. Note that the HC pairs tend to perform a positional angle change, which aligns them with PCP-axis (with or without PCI). Each dot presents one HC pair. wt – wild type, mut – mutant, HC – hair cell, A – anterior, P – posterior.

Altogether, this analysis revealed that the sibling hair cells have an intrinsic ability to invert as the neighboring cells do not contribute to the inversion by migrating. Surprisingly, the planar cell inventions take place in wild type as well as in *emx2* mutant larvae without any significant differences in frequency, wobbling rate, onset, and termination. Thus neither lack of Emx2 nor the cells' consequent lack of mirror-symmetric polarity pattern affects the ability of the cells to rotate about each other. Lack of Emx2 does not prevent cells from inverting, but, importantly, it also does not prevent the cells from ending the invention process. Importantly, the final positional angle of sibling HCs does not depend on the angle of the division of the UHCP, which produces HCs. The HC pairs finally align with the planar polarity axis in wild type and *emx2* mutant larvae, suggesting that Emx2 does not affect the final alignment of hair cells in a neuromast. The uninterrupted final alignment of HC pairs in *emx2* mutant larvae also confirms that the Notch1a/Emx2 pathway is separable from the neuromast-wide cell polarity controlled by the core planar polarity pathway.

6. Discussion

The focus of this thesis is understanding the formation of epithelial planar bipolarity. Previous studies have been focused on tissues with uniformly oriented cells. Therefore the formation of bipolar planar epithelia has remained largely understudied. The establishment of bipolar planar epithelium is a truly puzzling event because an additional level of complexity is added to the tissue polarization. Conceptually, three interwoven components are essential for epithelial planar bipolarity. First, a global frame of reference must be established to form a tissue-wide polarity axis. Second, symmetry breaking must emerge to generate cells of opposing orientations along this axis. Third, the coordination of cellular orientation to generate a line of polarity reversal perpendicular to the planar-polarity axis. Finally, in tissues with high cellular turnover, the process must iterate to ensure homeostasis. The problem of planar bipolarity gained momentum in coincidence to the start of this project, from the discovery that the transcription factor Emx2 is responsible for the generation of bipolar epithelia in the vestibular and lateral-line systems (T. Jiang et al., 2017). This opened the possibility to address the above questions, particularly the symmetry-breaking event leading to the opposite orientations of cells in epithelia. Revealing the mechanism that regulates asymmetric Emx2 activity represents a singular opportunity to understand the formation of epithelial planar bipolarity, which has been the focus of intense attention for remained unsolved.

In combination with advancements and increased availability of experimental techniques best exemplified by single-cell sequencing, I finally found the opportunity to answer such questions, using zebrafish as the experimental model.

6.1. The symmetry-breaking process

Single-cell RNA sequencing, followed by reconstruction of the temporal expression of genes using diffusion pseudotime and immunohistochemical validations, has led to one of the key findings of this thesis. Specifically, it allowed me to identify the moment of the symmetry-breaking event during the differentiation of neuromast hair cells. This is the most upstream step of bipolarity development. Furthermore, the results of this thesis have shown that the population asymmetry in the orientation of hair cells is achieved by breaking the symmetry in cell identity between two sibling cells. Namely, one of the sibling hair cells expresses Emx2

but not the other, resulting in two different cell identities (Emx2+ and Emx2-), with relatively sparse transcriptional differences, as shown in this thesis.

Specifically, the symmetry-breaking event was in this thesis studied by following the expression dynamics of Emx2. Unexpectedly, I found *emx2* expression starts already in UHCPs and is subsequently lost in one of the two sibling hair cells that develop from the division of a UHCP. The resulting asymmetry of Emx2 expression between sibling hair cells remains unchanged as they mature.

In addition to pinpointing when the symmetry-breaking event that leads to the acquisition of two different identities of sibling hair cells occurs, my thesis work also provides novel insights into how it happens. Intriguingly, genetic manipulations and protein visualizations have revealed that symmetry is a stochastic process mediated by signaling via the Notch1a receptor. Therefore, I focused on the role of Notch1a after observing an enrichment of Notch-signalling-related transcripts in UHCPs. My results show that the *notch1a* mutant larvae possess uniformly oriented hair cells and are in agreement with those Jacobo and collaborators published nearly concurrently with mine (2019). Interestingly, global inhibition of Notch signaling results in the opposite phenotype from *notch1a* mutagenesis for a yet unclear reason. Nevertheless, to confirm the role of Notch1a, I took advantage of NICD (mediator of Notch1a signaling) misexpression. In agreement with *notch1a* mutagenesis, misexpression of NICD represses Emx2 and additionally interferes with HC maturation when expressed early.

To the best of my knowledge, the Notch signaling and the specification of Emx2-dependent cell fate, as shown in this thesis, are novel. In particular, the genetic manipulations of *notch1a* (mutagenesis and misexpression, as well as the double mutagenesis of *emx2* and *notch1a*) clearly show that *notch1a* acts upstream of *emx2* and that Notch signaling downregulates *emx2* in hair cells. Thus, Notch1a regulates hair-cell orientation via Emx2.

However, Jacobo et al. (2019) suggest that Notch1a and Emx2 regulate hair-cell polarity by having opposite effects on an unknown polarity effector. Complementing these findings, I clearly show that Notch1a regulates hair-cell orientation via Emx2 by analyzing the HC orientation in *notch1a*, *emx2* double mutant larvae generated by somatic mutagenesis.

Notch signaling is universally required for hair-cell development in vertebrates (Brooker et

al., 2006; Lanford et al., 1999; Ma et al., 2008) and has been linked to asymmetric cell fate determination in other systems via asymmetric cell division (Charnley et al., 2019), or lateral inhibition (Lim et al., 2015). The role of Notch in cell fate acquisition is therefore not unique to neuromast hair cells, suggesting broader relevance of the results of this thesis. One of the great beauties in nature is utilizing the same molecular toolboxes in different tissues and organisms towards distinct goals, limiting the number of macromolecular signaling components encoded in the genomes while still allowing to achieve enormous biological diversity.

The analysis of Emx2 expression in nascent hair cells revealed that symmetry breaking between the sibling hair cells is stochastic. This conclusion derives from the random initial position of the Emx2-expressing cell. Whether Notch1a-mediated symmetry breaking between the siblings is facilitated by asymmetric segregation of the Notch signaling pathway components into the daughter cells during UHCP division or achieved exclusively via an initial stochastic bias of Notch signaling and lateral inhibition remains to be determined. In either case, the results of this thesis demonstrate the stochastic nature of symmetry breaking between sibling hair cells in neuromasts. Symmetry breaking between sibling cells is often explained with the analogy of marbles moving downhill through a hilly landscape, or a water wheel, in which a cell has to choose one of the options (Huang, 2016). For example, water falling onto a water wheel will inevitably push the system into a bi-stable situation, where a wheel will start rotating in either direction (Huang, 2016). Once the symmetry is broken, the system will be locked in a stable situation, creating a pattern. The most basic symmetry-breaking step in early development is the formation of animal and vegetative poles and the body axis (Schier, 2001). Symmetry breaking is a critical step of all tissue patterning mechanisms and fundamental to development and organogenesis. This thesis has provided key findings of the symmetry-breaking step that leads to the formation of the bipolar planar epithelium.

6.2. The hair-cell transcriptome

Some of the key results of this thesis were obtained by analyzing the transcriptional

landscape of single cells, namely the spatiotemporal dynamics of *emx2* expression.

Furthermore, the comparison of transcriptional profiles of individual hair cells in wild-type and *emx2* mutant larvae revealed no significant difference in the fraction of *emx2*-expressing cells in both samples, providing the first evidence that *emx2* is not self-regulated.

Furthermore, *emx2*-correlating genes have been identified. Because this thesis was not focused on identifying Emx2 target genes, only two genes were preliminarily tested. Yet, they were not found to be direct players in hair-cell orientation. The rest would need to be explored. It is important to remember that genes (anti)correlating with *emx2* could be involved in planar polarity determination. However, they alternatively may have other functions in hair cells. For example, hair cells within a single neuromast have different sensitivity to mechanical stimuli (Pichler & Lagnado, 2019). Furthermore, the differential sensitivity of hair cells has been linked to their orientation (Chou et al., 2017). Another example, the hair cells of different orientations are selectively innervated by distinct neurons, so the (anti)correlating with *emx2* genes likely contribute to neuronal target recognition (Dow et al., 2018; Y. R. Ji et al., 2018; Lozano-Ortega et al., 2018).

Taken together, the single-cell transcriptional analysis has provided critical insights into spatiotemporal dynamics of *emx2* expression and has given us broad information of transcriptional changes during HC differentiation. Importantly, the scRNAseq dataset generated in this thesis can be of broader use for other studies on mechanosensing or cell differentiation lineages.

Until recently, insights into single hair cells' transcriptome have been restricted by the limitations of bulk RNA sequencing techniques and by challenges related to hair cell's sensitivity and consequent difficulties with their isolation (Erickson & Nicolson, 2015; Matern et al., 2018). Most previous transcriptional studies of zebrafish hair cells have been performed using adult zebrafish inner ear hair cells or were more focused on support cells (Barta et al., 2018; Lush et al., 2019). Bulk RNA sequencing studies do not enable the identification of distinct cell types but instead only provide information about average gene expression in a certain tissue or organ. Consequently, there has been a knowledge gap calling for neuromast single-cell studies. Filling this gap, the first datasets providing single-cell transcriptional information of zebrafish neuromast cells have been published recently, including the paper resulting from this thesis (Kozak et al., 2020; Lush et al., 2019). In

comparison with the scRNA sequencing study of neuromast cells from zebrafish larvae by Lush et al. (2019), the dataset obtained in this thesis includes a much higher number of single-cell sequenced hair cells, specifically around 1000 hair cells in contrast to less than 200 hair cells from Lush et al. (2019). Having said that, the dataset from Lush et al. is composed of a higher number of single-cell sequenced support cells than the dataset in this thesis, and therefore, these two datasets are complementary.

In summary, I present the first single-cell RNAseq datasets focusing on neuromast hair cells and hereby complement the single-cell RNAseq dataset focused on neuromast support cells. These datasets can be in the future of use to address other questions. For example, comparing the zebrafish scRNAseq dataset with the one from mammals could provide insights into what allows zebrafish hair cells to be constantly replenished, whereas those of mammals can not regrow after damage.

6.3. The planar cell inversions

In the second part of the thesis, I focused on planar cell inversions, a process by which two sibling hair cells exchange their positions by undergoing a rotational migration.
In addition to cell identity and polarity, its localization is also critical for organogenesis. Spatial control of cell identity is critical for correct organ morphogenesis and tissue patterning.

The latter refers to single or collective cell migration to their desired location and plays an important role in development and disease. Single cells or collectives can migrate long distances; for example, cancer cells migrate to form metastasis (Lintz et al., 2017) or the migration of lateral line primordium across the larval body (Ledent, 2002). Intriguingly, cell migration can be critical for proper organ development and regeneration at a much finer scale and a short migrating distance, for example, during a wound closure (Dekoninck & Blanpain, 2019). A truly unique phenomenon of local cell migration of two sibling cells has been observed in the lateral line neuromasts, namely the process of planar cell inversions (Wibowo et al., 2011). Planar cell inversions are unique phenomena, to date only observed in zebrafish neuromasts (Erzberger et al., 2020; Mirkovic et al., 2012; Navajas Acedo et al., 2019; Wibowo et al., 2011). Contrary, the hair cells in other vertebrates have not been

reported to undergo planar cell inversions (Deans et al., 2007), but different types of cellular rearrangements have been shown to take place in distinct organs (Cetera et al., 2018; Naganathan et al., 2016). Nevertheless, the planar cell inversions have been discovered and first described a decade ago without any knowledge about their purpose (Mirkovic et al., 2012; Wibowo et al., 2011). The work of this thesis provides a comprehensive characterization of PCI. It offers novel findings supporting the notion that the PCIs functionally correct the stochasticity during the first step of bipolar epithelium formation, that is the symmetry-breaking event.

Extensive high-resolution live imaging and cell movement analyses have identified the planar cell inversions as a locally isolated event involving the sibling hair cells exclusively. Surprisingly, a combination of live videomicroscopy and mutagenesis eliminated Emx2 and its downstream effectors as promising candidates for controlling the PCI. Furthermore, neither the asymmetry in Emx2-determined cell identity nor the asymmetry in the structural positioning in hair cell bundles is necessary for the planar cell inversions to occur. The result was surprising since a recent study suggested that *notch1a* mutants lack PCI and further attributed the lack of inversions to the absence of asymmetry in the structural positioning of the hair cell bundles (Erzberger et al., 2020). Until a consensus in the field can be reached, the mechanism of the planar cell inversions process remains to be elucidated.

In summary, this thesis has been focused on the characterization of the process, stressing the deterministic aspect of PCI termination. Importantly, with the work of this thesis, a functional purpose of planar cell inversions has been proposed, linking the stochasticity of symmetry-breaking events to the final deterministic organ pattern.

Broadly speaking, a defined final organ structure is the key to proper organ function. The final organ structure needs to be defined in a reproducible manner, meaning that all steps involved in the organogenesis need to be regulated in a manner that makes them reproducible across potentially large temporal and spatial scales. Alternatively, imprecisely regulated or stochastic events taking place during development require the presence of correction mechanisms or alternatively collapse to a single outcome on a tissue-wide scale. Intriguingly, processes involving heterogeneous events, including stochastic and heterogeneous single-cell migration, ultimately leading to the defined outcome, have been shown in other systems. For instance, during the vertebrate retina formation, single

horizontal cells appear apically, then migrate basally in a very heterogeneous manner, but finally return to their proper location on the apical side (Amini et al., 2019). Altogether, such processes are rare and largely understudied and may contain molecular remnants from unrelated processes, recycled by evolution. Recent technical advancements and improved possibilities of visualizing single cells and their movements in their natural environment are enabling detailed cell behavior studies, and possibly more developmentally critical local cell migration events are yet to be discovered.

In organogenesis, heterogeneous or stochastic events need to collapse into a defined outcome to ensure proper organ function. Such mechanisms are critical for proper organ formation and might play an essential role in avoiding or correcting potential developmental inaccuracies. This thesis identifies planar cell inversions as a mechanism for correcting stochasticity in cell fate acquisition.

6.4. Concluding remarks

Understanding the fundamental principles of how cells differentiate and organize into complex three-dimensional structures contributes to our understanding of the form and function of all living organisms. An ample amount of work is still ahead of us before we completely understand cellular patterning mechanisms, even for simple tissues. Nevertheless, this thesis has contributed novel, and significant findings of broad interest as well as opened a door for future studies on the specific subjects of symmetry breaking and planar cell inversions. Importantly, this thesis resulted in key findings of the first and the last steps leading to the establishment of the planar bipolar epithelium, namely the symmetry-breaking event and the planar cell inversions, which, in neuromasts, ensure the epithelial mirror symmetry with facing hair bundles. Specifically, UHCPs initiate the expression of the key polarity-determining factor Emx2, which is ultimately lost in one of the two sibling hair cells via stochastic Notch1a-mediated symmetry breaking. Furthermore, this thesis has opened the question of how the *emx2* expression is regulated, revealing that it is not self-regulated by a feedback loop but initially downregulated via Notch1a in one of the sibling hair cells. Finally, the local rearrangements of cell pairs, called planar cell inversions, were shown to take place independently of Emx2 but with the functional purpose of ensuring epithelial mirror symmetry with facing hair cells.

Altogether, my findings present a novel mechanism of how stochastic or unregulated events can, in the end, lead to robust and reproducible organ formation. Understanding of cellular mechanisms underlying organogenesis and regeneration is providing us with basic knowledge about the inner working of all living organisms and has far-reaching implications in many areas of medicine. Elucidating development, organogenesis, and tissue patterning in the natural context also sheds light on diseases that arise from the failure of those mechanisms. Consequently, our findings pave the way to potential new approaches for treating diseases by contributing in-depth knowledge of organogenesis's molecular and cellular determinants.

7. References

Abate-Shen, C. (2002). Deregulated homeobox gene expression in cancer: cause or consequence? *Nature Reviews Cancer*, *2*(10), 777–785. https://doi.org/10.1038/nrc907

Aigouy, B., Umetsu, D., & Eaton, S. (2016). Segmentation and quantitative analysis of epithelial tissues. *Methods in Molecular Biology*, *1478*, 227–239. https://doi.org/10.1007/978-1-4939-6371-3_13

Amini, R., Labudina, A. A., & Norden, C. (2019). Stochastic single cell migration leads to robust horizontal cell layer formation in the vertebrate retina. *Development*, *146*(12), dev173450. https://doi.org/10.1242/dev.173450

Asakawa, K., & Kawakami, K. (2008). Targeted gene expression by the Gal4-UAS system in zebrafish. *Development, Growth & Differentiation*, *50*(6), 391–399. https://doi.org/10.1111/j.1440-169X.2008.01044.x

Askary, A., Xu, P., Barske, L., Bay, M., Bump, P., Balczerski, B., Bonaguidi, M. A., & Crump, J. G. (2017). Genome-wide analysis of facial skeletal regionalization in zebrafish. *Development (Cambridge)*, *144*(16), 2994–3005. https://doi.org/10.1242/dev.151712

Bagnoli, J. W., Ziegenhain, C., Janjic, A., Wange, L. E., Vieth, B., Parekh, S., Geuder, J., Hellmann, I., & Enard, W. (2018). Sensitive and powerful single-cell RNA sequencing using mcSCRB-seq. *Nature Communications*, *9*(1), 2937. https://doi.org/10.1038/s41467-018-05347-6

Barta, C. L., Liu, H., Chen, L., Giffen, K. P., Li, Y., Kramer, K. L., Beisel, K. W., & He, D. Z. (2018). RNA-seq transcriptomic analysis of adult zebrafish inner ear hair cells. *Scientific Data*, *5*(1), 180005. https://doi.org/10.1038/sdata.2018.5

Bayatti, N., Sarma, S., Shaw, C., Eyre, J. A., Vouyiouklis, D. A., Lindsay, S., & Clowry, G. J. (2008). Progressive loss of PAX6, TBR2, NEUROD and TBR1 mRNA gradients correlates with translocation of EMX2 to the cortical plate during human cortical development. *European Journal of Neuroscience*, *28*(8), 1449–1456. https://doi.org/10.1111/j.1460-9568.2008.06475.x

Beckmann, J., Vitobello, A., Ferralli, J., Bro, D. K., Rijli, F. M., & Chiquet-Ehrismann, R. (2011). Human teneurin-1 is a direct target of the homeobox transcription factor EMX2 at a

novel alternate promoter. *BMC Developmental Biology*, *11*, 35. https://doi.org/10.1186/1471-213X-11-35

Brignull, H. R., Raible, D. W., & Stone, J. S. (2009). Feathers and fins: Non-mammalian models for hair cell regeneration. *Brain Research*, *1277*, 12–23. https://doi.org/10.1016/j.brainres.2009.02.028

Brooker, R., Hozumi, K., & Lewis, J. (2006). Notch ligands with contrasting function: Jagged1 and Delta1 in the mouse inner ear. *Development*, *133*(7), 1277–1286. https://doi.org/10.1242/dev.02284

Butler, M. T., & Wallingford, J. B. (2017). Planar cell polarity in development and disease. *Nature Reviews Molecular Cell Biology*, *18*(6), 375–388. https://doi.org/10.1038/nrm.2017.11

Cecchi, C. (2002). Emx2: A gene responsible for cortical development, regionalization and area specification. *Gene*, *291*(1–2), 1–9. https://doi.org/10.1016/S0378-1119(02)00623-6

Cetera, M., Leybova, L., Joyce, B., & Devenport, D. (2018). Counter-rotational cell flows drive morphological and cell fate asymmetries in mammalian hair follicles. *Nature Cell Biology*, *20*(5), 541–552. https://doi.org/10.1038/s41556-018-0082-7

Charnley, M., Ludford-Menting, M., Pham, K., & Russell, S. M. (2019). A new role for Notch in the control of polarity and asymmetric cell division of developing T cells. *Journal of Cell Science*, *133*(5). https://doi.org/10.1242/jcs.235358

Choi, Y. H., & Kim, J. K. (2019). Dissecting cellular heterogeneity using single-cell RNA sequencing. *Molecules and Cells*, *42*(3), 189–199. https://doi.org/10.14348/molcells.2019.2446

Cholfin, J. A., & Rubenstein, J. L. R. (2008). Frontal cortex subdivision patterning is coordinately regulated by Fgf8, Fgf17, and Emx2. *Journal of Comparative Neurology*, *509*(2), 144–155. https://doi.org/doi:10.1002/cne.21709

Chou, S.-W., Chen, Z., Zhu, S., Davis, R. W., Hu, J., Liu, L., Fernando, C. A., Kindig, K., Brown, W. C., Stepanyan, R., & McDermott, B. M. (2017). A molecular basis for water motion detection by the mechanosensory lateral line of zebrafish. *Nature Communications*,

8(1), 2234. https://doi.org/10.1038/s41467-017-01604-2

Corwin, J. T., & Oberholtzer, J. C. (1997). Fish n' chicks: Model recipes for hair-cell regeneration? *Neuron*, *19*(5), 951–954. https://doi.org/10.1016/S0896-6273(00)80386-4

Cruz, I. A., Kappedal, R., Mackenzie, S. M., Hailey, D. W., Hoffman, T. L., Schilling, T. F., & Raible, D. W. (2015). Robust regeneration of adult zebrafish lateral line hair cells reflects continued precursor pool maintenance. *Developmental Biology*, *402*(2), 229–238. https://doi.org/10.1016/j.ydbio.2015.03.019

Cruz, I. A., Kappedal, R., Mackenzie, S. M., Hailey, D. W., Trevor, L., Schilling, T. F., Raible, D. W., Biology, C., & Angeles, W. L. (2016). *Reflects Continued Precursor Pool Maintenance*. *402*(2), 229–238. https://doi.org/10.1016/j.ydbio.2015.03.019.Robust

Dabdoub, A., Donohue, M. J., Brennan, A., Wolf, V., Montcouquiol, M., Sassoon, D. A., Hseih, J. C., Rubin, J. S., Salinas, P. C., & Kelley, M. W. (2003). Wnt signaling mediates reorientation of outer hair cell stereociliary bundles in the mammalian cochlea. *Development*, *130*(11), 2375–2384. https://doi.org/10.1242/dev.00448

David, N. B., Sapède, D., Saint-Etienne, L., Thisse, C., Thisse, B., Dambly-Chaudière, C., Rosa, F. M., & Ghysen, A. (2002). Molecular basis of cell migration in the fish lateral line: Role of the chemokine receptor CXCR4 and of its ligand, SDF1. *Proceedings of the National Academy of Sciences of the United States of America*, *99*(25), 16297–16302. https://doi.org/10.1073/pnas.252339399

Deans, M. R. (2013). A balance of form and function: Planar polarity and development of the vestibular maculae. *Seminars in Cell and Developmental Biology*, *24*(5), 490–498. https://doi.org/10.1016/j.semcdb.2013.03.001

Deans, M. R., Antic, D., Suyama, K., Scott, M. P., Axelrod, J. D., & Goodrich, L. V. (2007). Asymmetric distribution of Prickle-like 2 reveals an early underlying polarization of vestibular sensory epithelia in the inner ear. *Journal of Neuroscience*, *27*(12), 3139–3147. https://doi.org/10.1523/JNEUROSCI.5151-06.2007

Dekoninck, S., & Blanpain, C. (2019). Stem cell dynamics, migration and plasticity during wound healing. *Nature Cell Biology*, *21*(1), 18–24. https://doi.org/10.1038/s41556-018-0237-6

References

Desmaris, E., Keruzore, M., Saulnier, A., Ratié, L., Assimacopoulos, S., De Clercq, S., Nan, X., Roychoudhury, K., Qin, S., Kricha, S., Chevalier, C., Lingner, T., Henningfeld, K. A., Zarkower, D., Mallamaci, A., Theil, T., Campbell, K., Pieler, T., Li, M., … Bellefroid, E. J. (2018). DMRT5, DMRT3, and EMX2 cooperatively repress GSX2 at the pallium–subpallium boundary to maintain cortical identity in dorsal telencephalic progenitors. *Journal of Neuroscience*, *38*(42), 9105–9121. https://doi.org/10.1523/JNEUROSCI.0375-18.2018

Di Donato, V., Auer, T. O., Duroure, K., & Del Bene, F. (2013). Characterization of the Calcium Binding Protein Family in Zebrafish. *PLoS ONE*, *8*(1), e53299. https://doi.org/10.1371/journal.pone.0053299

Dow, E., Jacobo, A., Hossain, S., Siletti, K., & Hudspeth, A. J. (2018). Connectomics of the zebrafish's lateral-line neuromast reveals wiring and miswiring in a simple microcircuit. *ELife*, *7*, e33988. https://doi.org/10.7554/eLife.33988

Eden, E., Navon, R., Steinfeld, I., Lipson, D., & Yakhini, Z. (2009). GOrilla: A tool for discovery and visualization of enriched GO terms in ranked gene lists. *BMC Bioinformatics*, *10*, 48. https://doi.org/10.1186/1471-2105-10-48

Erickson, T., & Nicolson, T. (2015). Identification of sensory hair-cell transcripts by thiouracil-tagging in zebrafish. *BMC Genomics*, *16*(1), 842. https://doi.org/10.1186/s12864-015-2072-5

Erzberger, A., Jacobo, A., Dasgupta, A., & Hudspeth, A. J. (2020). Mechanochemical symmetry breaking during morphogenesis of lateral-line sensory organs. *Nature Physics*. https://doi.org/10.1038/s41567-020-0894-9

Ezan, J., Lasvaux, L., Gezer, A., Novakovic, A., May-Simera, H., Belotti, E., Lhoumeau, A. C., Birnbaumer, L., Beer-Hammer, S., Borg, J. P., Le Bivic, A., Nürnberg, B., Sans, N., & Montcouquiol, M. (2013). Primary cilium migration depends on G-protein signalling control of subapical cytoskeleton. *Nature Cell Biology*, *15*(9), 1107–1115. https://doi.org/10.1038/ncb2819

Flock, Å., & Lam, D. M. K. (1974). Neurotransmitter synthesis in inner ear and lateral line sense organs. *Nature*, *249*(5453), 142–144. https://doi.org/10.1038/249142a0

Flock, A., & Wersall, J. (1962). A study of the orientation of the sensory hairs of the receptor

cells in the lateral line organ of fish, with special reference to the function of the receptors. *The Journal of Cell Biology*, *15*, 19–27. https://doi.org/10.1083/jcb.15.1.19

Ghysen, A., & Dambly-Chaudière, C. (2004). Development of the zebrafish lateral line. *Current Opinion in Neurobiology*, *14*(1), 67–73. https://doi.org/10.1016/j.conb.2004.01.012

Ghysen, A., & Dambly-Chaudière, C. (2007). The lateral line microcosmos. *Genes and Development*, *21*(17), 2118–2130. https://doi.org/10.1101/gad.1568407

Gompel, N., Cubedo, N., Thisse, C., Thisse, B., Dambly-Chaudière, C., & Ghysen, A. (2001). Pattern formation in the lateral line of zebrafish. In *Mechanisms of Development* (Vol. 105, Issues 1–2). https://doi.org/10.1016/S0925-4773(01)00382-3

Goodrich, L. V., & Strutt, D. (2011). Principles of planar polarity in animal development. *Development*, *138*(10), 1877–1892. https://doi.org/10.1242/dev.054080

Grant, K. A., Raible, D. W., & Piotrowski, T. (2005). Regulation of latent sensory hair cell precursors by glia in the zebrafish lateral line. *Neuron*, *45*(1), 69–80. https://doi.org/10.1016/j.neuron.2004.12.020

Gray, M., Moens, C. B., Amacher, S. L., Eisen, J. S., & Beattie, C. E. (2001). Zebrafish deadly seven functions in neurogenesis. *Developmental Biology*, *237*(2), 306–323. https://doi.org/10.1006/dbio.2001.0381

Groves, A. K., Zhang, K. D., & Fekete, D. M. (2013). The Genetics of Hair Cell Development and Regeneration. *Annual Review of Neuroscience*, *36*(1), 361–381. https://doi.org/10.1146/annurev-neuro-062012-170309

Groves, J. A., Gillman, C., DeLay, C. N., & Kroll, T. T. (2019). Identification of Novel Binding Partners for Transcription Factor Emx2. *Protein Journal*, *38*(1), 2–11. https://doi.org/10.1007/s10930-019-09810-1

Haas, P., & Gilmour, D. (2006). Chemokine Signaling Mediates Self-Organizing Tissue Migration in the Zebrafish Lateral Line. *Developmental Cell*, *10*(5), 673–680. https://doi.org/10.1016/j.devcel.2006.02.019

Haghverdi, L., Büttner, M., Wolf, F. A., Buettner, F., & Theis, F. J. (2016). Diffusion pseudotime robustly reconstructs lineage branching. *Nature Methods*, *13*(10), 845–848.

https://doi.org/10.1038/nmeth.3971

Hale, R., Brittle, A. L., Fisher, K. H., Monk, N. A. M., & Strutt, D. (2015). Cellular interpretation of the long-range gradient of Four-jointed activity in the Drosophila wing. *ELife*, *4*, e05789. https://doi.org/10.7554/eLife.05789

Harris, J. A., Cheng, A. G., Cunningham, L. L., MacDonald, G., Raible, D. W., & Rubel, E. W. (2003). Neomycin-induced hair cell death and rapid regeneration in the lateral line of zebrafish (Danio rerio). *JARO - Journal of the Association for Research in Otolaryngology*, *4*(2), 219–234. https://doi.org/10.1007/s10162-002-3022-x

Hernández, P. P., Moreno, V., Olivari, F. A., & Allende, M. L. (2006). Sub-lethal concentrations of waterborne copper are toxic to lateral line neuromasts in zebrafish (Danio rerio). *Hearing Research*, *213*(1–2), 1–10. https://doi.org/10.1016/j.heares.2005.10.015

Holley, M., Rhodes, C., Kneebone, A., Herde, M. K., Fleming, M., & Steel, K. P. (2010). Emx2 and early hair cell development in the mouse inner ear. *Developmental Biology*, *340*(2), 547–556. https://doi.org/10.1016/j.ydbio.2010.02.004

Howe, K., Clark, M. D., Torroja, C. F., Torrance, J., Berthelot, C., Muffato, M., Collins, J. E., Humphray, S., McLaren, K., Matthews, L., McLaren, S., Sealy, I., Caccamo, M., Churcher, C., Scott, C., Barrett, J. C., Koch, R., Rauch, G. J., White, S., … Stemple, D. L. (2013). The zebrafish reference genome sequence and its relationship to the human genome. *Nature*, *496*(7446), 498–503. https://doi.org/10.1038/nature12111

Huang, S. (2016). Where to Go: Breaking the Symmetry in Cell Motility. *PLOS Biology*, *14*(5), e1002463. https://doi.org/10.1371/journal.pbio.1002463

Hudspeth, A. J., & Corey, D. P. (1977). Sensitivity, polarity, and conductance change in the response of vertebrate hair cells to controlled mechanical stimuli. *Proceedings of the National Academy of Sciences of the United States of America*, *74*(6), 2407–2411. https://doi.org/10.1073/pnas.74.6.2407

Jacobo, A., Dasgupta, A., Erzberger, A., Siletti, K., & Hudspeth, A. J. (2019). Notch-Mediated Determination of Hair-Bundle Polarity in Mechanosensory Hair Cells of the Zebrafish Lateral Line. *Current Biology*, *29*(21), 3579-3587.e7. https://doi.org/10.1016/j.cub.2019.08.060

Ji, D., Li, L., Zhang, S., & Li, H. (2015). Identification of a Ly-6 superfamily gene expressed in lateral line neuromasts in zebrafish. *Development Genes and Evolution*, *225*(1), 47–53. https://doi.org/10.1007/s00427-015-0487-2

Ji, Y. R., Warrier, S., Jiang, T., Wu, D. K., & Kindt, K. S. (2018). Directional selectivity of afferent neurons in zebrafish neuromasts is regulated by Emx2 in presynaptic hair cells. *ELife*, *7*, e35796. https://doi.org/10.7554/eLife.35796

Jiang, L., Romero-Carvajal, A., Haug, J. S., Seidel, C. W., & Piotrowski, T. (2014). Gene-expression analysis of hair cell regeneration in the zebrafish lateral line. *Proceedings of the National Academy of Sciences of the United States of America*, *111*(14), e1383–e1392. https://doi.org/10.1073/pnas.1402898111

Jiang, T., Kindt, K., & Wu, D. K. (2017). Transcription factor emx2 controls stereociliary bundle orientation of sensory hair cells. *ELife*, *6*, e23661. https://doi.org/10.7554/eLife.23661

Johnson, W. E., Li, C., & Rabinovic, A. (2007). Adjusting batch effects in microarray expression data using empirical Bayes methods. *Biostatistics*, *8*(1), 118–127. https://doi.org/10.1093/biostatistics/kxj037

Jørgensen, J. M. (1989). Evolution of Octavolateralis Sensory Cells. In S. Coombs, P. Görner, & H. Münz (Eds.), *The Mechanosensory Lateral Line* (pp. 115–145). Springer. https://doi.org/10.1007/978-1-4612-3560-6_6

Kalmijn, A. J. (1989). Functional Evolution of Lateral Line and Inner Ear Sensory Systems. In S. Coombs, P. Görner, & H. Münz (Eds.), *The Mechanosensory Lateral Line* (pp. 187–215). https://doi.org/10.1007/978-1-4612-3560-6_9

Kawakami, K., & Noda, T. (2004). *Transposition of the Tol2 Element, an Ac-Like Element From the Japanese Medaka Fish Oryzias latipes, in Mouse Embryonic Stem Cells*. *899*(2), 895–899.

Kindt, K. S., Finch, G., & Nicolson, T. (2012). Kinocilia Mediate Mechanosensitivity in Developing Zebrafish Hair Cells. *Developmental Cell*, *23*(2), 329–341. https://doi.org/10.1016/j.devcel.2012.05.022

Kondrychyn, I., Teh, C., Garcia-Lecea, M., Guan, Y., Kang, A., & Korzh, V. (2011). Zebrafish

Enhancer TRAP Transgenic Line Database ZETRAP 2.0. *Zebrafish*, *8*(4), 181–182. https://doi.org/10.1089/zeb.2011.0718

Kozak, E. L., Palit, S., Miranda-Rodríguez, J. R., Janjic, A., Böttcher, A., Lickert, H., Enard, W., Theis, F. J., & López-Schier, H. (2020). Epithelial Planar Bipolarity Emerges from Notch-Mediated Asymmetric Inhibition of Emx2. *Current Biology*, *30*(6), 1142-1151.e6. https://doi.org/10.1016/j.cub.2020.01.027

Kwan, K. M., Fujimoto, E., Grabher, C., Mangum, B. D., Hardy, M. E., Campbell, D. S., Parant, J. M., Yost, H. J., Kanki, J. P., & Chien, C. Bin. (2007). The Tol2kit: A multisite gateway-based construction Kit for Tol2 transposon transgenesis constructs. *Developmental Dynamics*, *236*(11), 3088–3099. https://doi.org/10.1002/dvdy.21343

La Manno, G., Soldatov, R., Zeisel, A., Braun, E., Hochgerner, H., Petukhov, V., Lidschreiber, K., Kastriti, M. E., Lönnerberg, P., Furlan, A., Fan, J., Borm, L. E., Liu, Z., van Bruggen, D., Guo, J., He, X., Barker, R., Sundström, E., Castelo-Branco, G., … Kharchenko, P. V. (2018). RNA velocity of single cells. *Nature*, *560*(7719), 494–498. https://doi.org/10.1038/s41586-018-0414-6

Labuhn, M., Adams, F. F., Ng, M., Knoess, S., Schambach, A., Charpentier, E. M., Schwarzer, A., Mateo, J. L., Klusmann, J. H., & Heckl, D. (2018). Refined sgRNA efficacy prediction improves largeand small-scale CRISPR-Cas9 applications. *Nucleic Acids Research*, *46*(3), 1375–1385. https://doi.org/10.1093/nar/gkx1268

Ledent, V. (2002). Postembryonic development of the posterior lateral line in zebrafish 597. *Development*, *129*(3), 597–604.

Li, H., Bishop, K. M., & O'Leary, D. D. M. (2006). Potential target genes of EMX2 include Odz/Ten-M and other gene families with implications for cortical patterning. *Molecular and Cellular Neuroscience*, *33*(2), 136–149. https://doi.org/10.1016/j.mcn.2006.06.012

Lim, K. J., Brandt, W. D., Heth, J. A., Muraszko, K. M., Fan, X., Bar, E. E., & Eberhart, C. G. (2015). Lateral inhibition of Notch signaling in neoplastic cells. *Oncotarget*, *6*(3), 1666–1677. https://doi.org/10.18632/oncotarget.2762

Lintz, M., Muñoz, A., & Reinhart-King, C. A. (2017). The Mechanics of Single Cell and Collective Migration of Tumor Cells. *Journal of Biomechanical Engineering*, *139*(2), 210051–210059. https://doi.org/10.1115/1.4035121

López-Schier, H., & Hudspeth, A. J. (2006). A two-step mechanism underlies the planar polarization of regenerating sensory hair cells. *Proceedings of the National Academy of Sciences of the United States of America*, *103*(49), 18615–18620. https://doi.org/10.1073/pnas.0608536103

López-Schier, H., Starr, C. J., Kappler, J. A., Kollmar, R., & Hudspeth, A. J. (2004). Directional cell migration establishes the axes of planar polarity in the posterior lateral-Line organ of the zebrafish. *Developmental Cell*, *7*(3), 401–412. https://doi.org/10.1016/j.devcel.2004.07.018

Lozano-Ortega, M., Valera, G., Xiao, Y., Faucherre, A., & López-Schier, H. (2018). Hair cell identity establishes labeled lines of directional mechanosensation. *PLoS Biology*, *16*(7), e2004404. https://doi.org/10.1371/journal.pbio.2004404

Lush, M. E., Diaz, D. C., Koenecke, N., Baek, S., Boldt, H., St Peter, M. K., Gaitan-Escudero, T., Romero-Carvajal, A., Busch-Nentwich, E. M., Perera, A. G., Hall, K. E., Peak, A., Haug, J. S., & Piotrowski, T. (2019). scRNA-Seq reveals distinct stem cell populations that drive hair cell regeneration after loss of Fgf and Notch signaling. *ELife*, *8*, e44431. https://doi.org/10.7554/eLife.44431.001

Ma, E. Y., Rubel, E. W., & Raible, D. W. (2008). Notch signaling regulates the extent of hair cell regeneration in the zebrafish lateral line. *Journal of Neuroscience*, *28*(9), 2261–2273. https://doi.org/10.1523/JNEUROSCI.4372-07.2008

Matern, M. S., Beirl, A., Ogawa, Y., Song, Y., Paladugu, N., Kindt, K. S., & Hertzano, R. (2018). Transcriptomic profiling of zebrafish hair cells using RiboTag. *Frontiers in Cell and Developmental Biology*, *6*, 47. https://doi.org/10.3389/fcell.2018.00047

May-Simera, H., & Kelley, M. W. (2012). Planar Cell Polarity in the Inner Ear. *Current Topics in Developmental Biology*, *101*, 111–140. https://doi.org/10.1016/B978-0-12-394592-1.00006-5

McDermott, B. M., Baucom, J. M., & Hudspeth, A. J. (2007). Analysis and functional evaluation of the hair-cell transcriptome. *Proceedings of the National Academy of Sciences of the United States of America*, *104*(28), 11820–11825. https://doi.org/10.1073/pnas.0704476104

Meijering, E., Dzyubachyk, O., & Smal, I. (2012). Methods for cell and particle tracking.

Methods in Enzymology, *504*, 183–200. https://doi.org/10.1016/B978-0-12-391857-4.00009-4

Metcalfe, W. K., Kimmel, C. B., & Schabtach, E. (1985). Anatomy of the posterior lateral line system in young larvae of the zebrafish. *Journal of Comparative Neurology*, *233*(3), 377–389. https://doi.org/10.1002/cne.902330307

Mirkovic, I., Pylawka, S., & Hudspeth, A. J. (2012). Rearrangements between differentiating hair cells coordinate planar polarity and the establishment of mirror symmetry in lateral-line neuromasts. *Biology Open*, *1*(5), 498–505. https://doi.org/10.1242/bio.2012570

Miyamoto, N., Yoshida, M., Kuratani, S., Matsuo, I., & Aizawa, S. (1997). Defects of urogenital development in mice lacking Emx2. *Development*, *124*(9), 1653–1664.

Monnier, A., Boniface, R., Bouvet, R., Etcheverry, A., Aubry, M., Avril, T., Quillien, V., Chevet, E., & Mosser, J. (2018). The expression of EMX2 lead to cell cycle arrest in glioblastoma cell line. *BMC Cancer*, *18*(1), 1213. https://doi.org/10.1186/s12885-018-5094-y

Montcouquiol, M., Rachel, R. A., Lanford, P. J., Copeland, N. G., Jenkins, N. A., & Kelley, M. W. (2003). Identification of Vangl2 and Scrb1 as planar polarity genes in mammals. *Nature*, *423*(6936), 173–177. https://doi.org/10.1038/nature01618

Naganathan, S. R., Middelkoop, T. C., Fürthauer, S., & Grill, S. W. (2016). Actomyosin-driven left-right asymmetry: From molecular torques to chiral self organization. *Current Opinion in Cell Biology*, *38*, 24–30. https://doi.org/10.1016/j.ceb.2016.01.004

Namdaran, P., Reinhart, K. E., Owens, K. N., Raible, D. W., & Rubel, E. W. (2012). Identification of modulators of hair cell regeneration in the zebrafish lateral line. *Journal of Neuroscience*, *32*(10), 3516–3528. https://doi.org/10.1523/JNEUROSCI.3905-11.2012

Navajas Acedo, J., Voas, M. G., Alexander, R., Woolley, T., Unruh, J. R., Li, H., Moens, C., & Piotrowski, T. (2019). PCP and Wnt pathway components act in parallel during zebrafish mechanosensory hair cell orientation. *Nature Communications*, *10*(1), 3993. https://doi.org/10.1038/s41467-019-12005-y

Nechiporuk, A., & Raible, D. W. (2008). FGF-dependent mechanosensory organ patterning in

zebrafish. *Science*, *320*(5884), 1774–1777. https://doi.org/10.1126/science.1156547

Nédélec, S., Foucher, I., Brunet, I., Bouillot, C., Prochiantz, A., & Trembleau, A. (2004). Emx2 homeodomain transcription factor interacts with eukaryotic translation initiation factor 4E (eIF4E) in the axons of olfactory sensory neurons. *Proceedings of the National Academy of Sciences of the United States of America*, *101*(29), 10815–10820. https://doi.org/10.1073/pnas.0403824101

Nicolson, T. (2017). The genetics of hair-cell function in zebrafish. *Journal of Neurogenetics*, *31*(3), 102–112. https://doi.org/10.1080/01677063.2017.1342246

Norden, C. (2017). Pseudostratified epithelia - cell biology, diversity and roles in organ formation at a glance. *Journal of Cell Science*, *130*(11), 1859—1863. https://doi.org/10.1242/jcs.192997

Nuñez, V. A., Sarrazin, A. F., Cubedo, N., Allende, M. L., Dambly-Chaudière, C., & Ghysen, A. (2009). Postembryonic development of the posterior lateral line in the zebrafish. *Evolution and Development*, *11*(4), 391–404. https://doi.org/10.1111/j.1525-142X.2009.00346.x

Ogun, O., & Zallocchi, M. (2014). Clarin-1 acts as a modulator of mechanotransduction activity and presynaptic ribbon assembly. *Journal of Cell Biology*, *207*(3), 375–391. https://doi.org/10.1083/jcb.201404016

Oteiza, P., Odstrcil, I., Lauder, G., Portugues, R., & Engert, F. (2017). A novel mechanism for mechanosensory-based rheotaxis in larval zebrafish. *Nature*, *547*(7664), 445–448. https://doi.org/10.1038/nature23014

Papalexi, E., & Satija, R. (2018). Single-cell RNA sequencing to explore immune cell heterogeneity. *Nature Reviews Immunology*, *18*(1), 35–45. https://doi.org/10.1038/nri.2017.76

Pei, W., Xu, L., Huang, S. C., Pettie, K., Idol, J., Rissone, A., Jimenez, E., Sinclair, J. W., Slevin, C., Varshney, G. K., Jones, M. P., Carrington, B., Bishop, K., Huang, H., Sood, R., Lin, S., & Burgess, S. M. (2018). Guided genetic screen to identify genes essential in the regeneration of hair cells and other tissues. *NPJ Regenerative Medicine*, *3*, 11. https://doi.org/10.1038/s41536-018-0050-7

Pellegrini, M., Mansouri, A., Simeone, A., Boncinelli, E., & Gruss, P. (1996). Dentate gyrus formation requires Emx2. *Development*, *122*(12), 3893–3898. http://dev.biologists.org/content/122/12/3893.abstract

Pellegrini, M., Pantano, S., Lucchini, F., Fumi, M., & Forabosco, A. (1997). Emx2 developmental expression in the primordia of the reproductive and excretory systems. *Anatomy and Embryology*, *196*(6), 427–433. https://doi.org/10.1007/s004290050110

Pichler, P., & Lagnado, L. (2019). The transfer characteristics of hair cells encoding mechanical stimuli in the lateral line of zebrafish. *Journal of Neuroscience*, *39*(1), 112–124. https://doi.org/10.1523/JNEUROSCI.1472-18.2018

Pinto-Teixeira, F., Viader-Llargués, O., Torres-Mejía, E., Turan, M., González-Gualda, E., Pola-Morell, L., & Lopez-Schier, H. (2015). Inexhaustible hair-cell regeneration in young and aged zebrafish. *Biology Open*, *4*(7), 903–909. https://doi.org/10.1242/bio.012112

Potter, S. S. (2018). Single-cell RNA sequencing for the study of development, physiology and disease. *Nature Reviews Nephrology*, *14*(8), 479–492. https://doi.org/10.1038/s41581-018-0021-7

Pröls, F., Ehehalt, F., Rodriguez-Niedenführ, M., He, L., Huang, R., & Christ, B. (2004). The role of Emx2 during scapula formation. *Developmental Biology*, *275*(2), 315–324. https://doi.org/10.1016/j.ydbio.2004.08.003

Pujol-Martí, J., Faucherre, A., Aziz-Bose, R., Asgharsharghi, A., Colombelli, J., Trapani, J. G., & López-Schier, H. (2014). Converging axons collectively initiate and maintain synaptic selectivity in a constantly remodeling sensory organ. *Current Biology*, *24*(24), 2968–2974. https://doi.org/10.1016/j.cub.2014.11.012

Python Software Foundation. (2009). *Python Language Reference* (pp. 457–538). Centrum voor Wiskunde en Informatica (CWI). https://doi.org/10.1201/9781584889304.axd

R Core Team. (2020). A Language and Environment for Statistical Computing. In *R Foundation for Statistical Computing* (4.0.0; Vol. 2). R Foundation for Statistical Computing. http://www.r-project.org

Raudvere, U., Kolberg, L., Kuzmin, I., Arak, T., Adler, P., Peterson, H., & Vilo, J. (2019). G:Profiler: A web server for functional enrichment analysis and conversions of gene lists

(2019 update). *Nucleic Acids Research*, *47*(W1), W191–W198. https://doi.org/10.1093/nar/gkz369

Rhodes, C. R., Parkinson, N., Tsai, H., Brooker, D., Mansell, S., Spurr, N., Hunter, A. J., Steel, K. P., & Brown, S. D. M. (2003). The homeobox gene Emx2 underlies middle ear and inner ear defects in the deaf mouse mutant pardon. *Journal of Neurocytology*, *32*(9), 1143–1154. https://doi.org/10.1023/B:NEUR.0000021908.98337.91

Romero-Carvajal, A., Navajas Acedo, J., Jiang, L., Kozlovskaja-Gumbrienė, A., Alexander, R., Li, H., & Piotrowski, T. (2015). Regeneration of Sensory Hair Cells Requires Localized Interactions between the Notch and Wnt Pathways. *Developmental Cell*, *34*(3), 267–282. https://doi.org/10.1016/j.devcel.2015.05.025

RStudio Team. (2016). *RStudio: Integrated development environment for R* (1.0.143). RStudio, Inc. http://www.rstudio.org

Sapède, D., Gompel, N., Dambly-Chaudière, C., & Ghysen, A. (2002). Cell migration in the postembryonic development of the fish lateral line. *Development*, *129*(3), 605–615.

Scheer, N., & Campos-Ortega, J. A. (1999). Use of the Gal4-UAS technique for targeted gene expression in the zebrafish. *Mechanisms of Development*, *80*(2), 153–158. https://doi.org/https://doi.org/10.1016/S0925-4773(98)00209-3

Schier, A. F. (2001). Axis formation and patterning in zebrafish. *Current Opinion in Genetics & Development*, *11*(4), 393–404. https://doi.org/10.1016/s0959-437x(00)00209-4

Schindelin, J., Arganda-Carreras, I., Frise, E., Kaynig, V., Longair, M., Pietzsch, T., Preibisch, S., Rueden, C., Saalfeld, S., Schmid, B., Tinevez, J.-Y., White, D. J., Hartenstein, V., Eliceiri, K., Tomancak, P., & Cardona, A. (2012). Fiji: an open-source platform for biological-image analysis. *Nature Methods*, *9*(7), 676–682. https://doi.org/10.1038/nmeth.2019

Seiler, C., Ben-David, O., Sidi, S., Hendrich, O., Rusch, A., Burnside, B., Avraham, K. B., & Nicolson, T. (2004). Myosin VI is required for structural integrity of the apical surface of sensory hair cells in zebrafish. *Developmental Biology*, *272*(2), 328–338. https://doi.org/10.1016/j.ydbio.2004.05.004

Shotwell, S. L., Jacobs, R., & Hudspeth, A. J. (1981). Directional Sensitivity of Individual Vertebrate Hair Cells To Controlled Deflection of Their Hair Bundles. *Annals of the New*

York Academy of Sciences, *374*(1), 1–10. https://doi.org/10.1111/j.1749-6632.1981.tb30854.x

Sieger, D., Tautz, D., & Gajewski, M. (2003). The role of Suppressor of Hairless in Notch mediated signalling during zebrafish somitogenesis. *Mechanisms of Development*, *120*(9), 1083–1094. https://doi.org/https://doi.org/10.1016/S0925-4773(03)00154-0

Sierra, H., Cordova, M., Chen, C. S. J., & Rajadhyaksha, M. (2015). Confocal imaging-guided laser ablation of basal cell carcinomas: An ex vivo study. *Journal of Investigative Dermatology*, *135*(2), 612–615. https://doi.org/10.1038/jid.2014.371

Siletti, K., Tarchini, B., & Hudspeth, A. J. (2017). Daple coordinates organ-wide and cell-intrinsic polarity to pattern inner-ear hair bundles. *Proceedings of the National Academy of Sciences of the United States of America*, *114*(52), E11170–E11179. https://doi.org/10.1073/pnas.1716522115

Simeone, A., Gulisano, M., Acampora, D., Stornaiuolo, A., Rambaldi, M., & Boncinelli, E. (1992). Two vertebrate homeobox genes related to the Drosophila empty spiracles gene are expressed in the embryonic cerebral cortex. *The EMBO Journal*, *11*(7), 2541–2550. https://doi.org/10.1002/j.1460-2075.1992.tb05319.x

Steiner, A. B., Kim, T., Cabot, V., & Hudspeth, A. J. (2014). Dynamic gene expression by putative hair-cell progenitors during regeneration in the zebrafish lateral line. *Proceedings of the National Academy of Sciences of the United States of America*, *111*(14), E1393-E1401. https://doi.org/10.1073/pnas.1318692111

Stemmer, M., Thumberger, T., Del Sol Keyer, M., Wittbrodt, J., & Mateo, J. L. (2015). CCTop: An intuitive, flexible and reliable CRISPR/Cas9 target prediction tool. *PLoS ONE*, *10*(4), e0124633. https://doi.org/10.1371/journal.pone.0124633

Stewart, W. J., Cardenas, G. S., & McHenry, M. J. (2013). Zebrafish larvae evade predators by sensing water flow. *Journal of Experimental Biology*, *216*(3), 388–398. https://doi.org/10.1242/jeb.072751

Tarchini, B., & Lu, X. (2019). New insights into regulation and function of planar polarity in the inner ear. *Neuroscience Letters*, *709*, 134373. https://doi.org/10.1016/j.neulet.2019.134373

Tarchini, B., Tadenev, A. L. D., Devanney, N., & Cayouette, M. (2016). A link between planar polarity and staircase-like bundle architecture in hair cells. *Development*, *143*(21), 3926–3932. https://doi.org/10.1242/dev.139089

Taylor, H. (2015). The role of EMX2 in uterine development. *Fertil Steril.*, *103*(3), 633–634. https://doi.org/10.1016/j.fertnstert.2015.01.009

Thisse, B., Pflumio, S., Fürthauer, M., Loppin, B., Heyer, V., Degrave, A., Woehl, R., Lux, A., Steffan, T., Charbonnier, X. Q., & Thisse, C. (2001). Expression of the zebrafish genome during embryogenesis. *ZFIN Direct Data Submission*.

Thisse, Bernard, Heyer, V., Lux, A., Alunni, V., Degrave, A., Seiliez, I., Kirchner, J., Parkhill, J. P., & Thisse, C. (2004). Spatial and temporal expression of the zebrafish genome by large-scale in situ hybridization screening. *Methods in Cell Biology*, *2004*(77), 505–519. https://doi.org/10.1016/s0091-679x(04)77027-2

Thomas, E. D., & Raible, D. W. (2019). Distinct progenitor populations mediate regeneration in the zebrafish lateral line. *ELife*, *8*, e43736. https://doi.org/10.7554/eLife.43736

Trapnell, C., Cacchiarelli, D., Grimsby, J., Pokharel, P., Li, S., Morse, M., Lennon, N. J., Livak, K. J., Mikkelsen, T. S., & Rinn, J. L. (2014). The dynamics and regulators of cell fate decisions are revealed by pseudotemporal ordering of single cells. *Nature Biotechnology*, *32*(4), 381–386. https://doi.org/10.1038/nbt.2859

Varshney, G. K., Pei, W., LaFave, M. C., Idol, J., Xu, L., Gallardo, V., Carrington, B., Bishop, K., Jones, M., Li, M., Harper, U., Huang, S. C., Prakash, A., Chen, W., Sood, R., Ledin, J., & Burgess, S. M. (2015). High-throughput gene targeting and phenotyping in zebrafish using CRISPR/Cas9. *Genome Research*, *25*(7), 1030–1042. https://doi.org/10.1101/gr.186379.114

Viader-Llargués, O., Lupperger, V., Pola-Morell, L., Marr, C., & López-Schier, H. (2018). Live cell-lineage tracing and machine learning reveal patterns of organ regeneration. *ELife*, *7*, e30823. https://doi.org/10.7554/eLife.30823

Vieth, B., Parekh, S., Ziegenhain, C., Enard, W., & Hellmann, I. (2019). A systematic evaluation of single cell RNA-seq analysis pipelines. *Nature Communications*, *10*(1), 4667. https://doi.org/10.1038/s41467-019-12266-7

Wada, H., Ghysen, A., Satou, C., Higashijima, S.-I., Kawakami, K., Hamaguchi, S., & Sakaizumi, M. (2010). Dermal morphogenesis controls lateral line patterning during postembryonic development of teleost fish. *Developmental Biology*, *340*(2), 583–594. https://doi.org/10.1016/j.ydbio.2010.02.017

Wang, J., Hamblet, N. S., Mark, S., Dickinson, M. E., Brendan, C., Segil, N., Fraser, S. E., Chen, P., & Wallingford, J. B. (2006). *Dishevelled genes mediate a conserved mammalian PCP pathway to regulate convergent extension during neurulation*. *133*(9), 1767–1778. https://doi.org/10.1242/dev.02347.Dishevelled

Wang, L., Joy, J. I. N., Zhou, Y., Tian, Z., Biao, H. E., Huang, Y., & Ding, F. (2019). EMX2 is epigenetically silenced and suppresses epithelial-mesenchymal transition in human esophageal adenocarcinoma. *Oncology Reports*, *42*(5), 2169–2178. https://doi.org/10.3892/or.2019.7284

Westerfield, M. (2007). *The Zebrafish Book. A Guide for the Laboratory Use of Zebrafish (Danio rerio)* (5th ed.). University of Oregon Press.

Whitfield, T. T., Granato, M., van Eeden, F. J., Schach, U., Brand, M., Furutani-Seiki, M., Haffter, P., Hammerschmidt, M., Heisenberg, C. P., Jiang, Y. J., Kane, D. A., Kelsh, R. N., Mullins, M. C., Odenthal, J., & Nusslein-Volhard, C. (1996). Mutations affecting development of the zebrafish inner ear and lateral line. *Development*, *123*(1), 241–254. http://dev.biologists.org/content/123/1/241.abstract

Wibowo, I., Pinto-Teixeira, F., Satou, C., Higashijima, S. I., & López-Schier, H. (2011). Compartmentalized Notch signaling sustains epithelial mirror symmetry. *Development*, *138*(6), 1143–1152. https://doi.org/10.1242/dev.060566

Wickham, H. (2016). *ggplot2: Elegant Graphics for Data Analysis*. Springer-Verlag New York. https://ggplot2.tidyverse.org

Wigglesworth, V. B. (1940). Local and General Factors in the Development of "Pattern" in Rhodnius Prolixus (Hemiptera). *Journal of Experimental Biology*, *17*(2), 180–201.

Williams, J. A., & Holder, N. (2000). Cell turnover in neuromasts of zebrafish larvae. *Hearing Research*, *143*(1–2), 171–181. https://doi.org/10.1016/S0378-5955(00)00039-3

Wolf, F. A., Angerer, P., & Theis, F. J. (2018). Open Access SCANPY : large-scale single-cell

gene expression data analysis. *Genome Biology*, *15*(19). https://doi.org/10.1186/s13059-017-1382-0

Wolock, S. L., Lopez, R., & Klein, A. M. (2019). Scrublet: Computational Identification of Cell Doublets in Single-Cell Transcriptomic Data. *Cell Systems*, *8*(4), 281-291.e9. https://doi.org/https://doi.org/10.1016/j.cels.2018.11.005

Wu, R. S., Lam, I. I., Clay, H., Duong, D. N., Deo, R. C., & Coughlin, S. R. (2018). A Rapid Method for Directed Gene Knockout for Screening in G0 Zebrafish. *Developmental Cell*, *46*(1), 112-125.e4. https://doi.org/10.1016/j.devcel.2018.06.003

Wu, Y., & Zhang, K. (2020). Tools for the analysis of high-dimensional single-cell RNA sequencing data. *Nature Reviews Nephrology*. https://doi.org/10.1038/s41581-020-0262-0

Xiao, T., & Baier, H. (2007). Lamina-specific axonal projections in the zebrafish tectum require the type IV collagen Dragnet. *Nature Neuroscience*, *10*(12), 1529–1537. https://doi.org/10.1038/nn2002

Yoshida, M., Suda, Y., Matsuo, I., Miyamoto, N., Takeda, N., Kuratani, S., & Aizawa, S. (1997). Emx1 and Emx2 functions in development of dorsal telencephalon. *Development*, *124*(1), 101–111. http://dev.biologists.org/content/124/1/101.abstract

Zallen, J. A. (2007). Planar Polarity and Tissue Morphogenesis. *Cell*, *129*(6), 1051–1063. https://doi.org/10.1016/j.cell.2007.05.050

Zallen, J. A., & Wieschaus, E. (2004). Patterned gene expression directs bipolar planar polarity in Drosophila. *Developmental Cell*, *6*(3), 343–355. https://doi.org/10.1016/S1534-5807(04)00060-7

Zembrzycki, A., Griesel, G., Stoykova, A., & Mansouri, A. (2007). Genetic interplay between the transcription factors Sp8 and Emx2 in the patterning of the forebrain. *Neural Development*, *2*, 8. https://doi.org/10.1186/1749-8104-2-8

Zhang, X., Li, T., Liu, F., Chen, Y., Yao, J., Li, Z., Huang, Y., & Wang, J. (2019). Comparative Analysis of Droplet-Based Ultra-High-Throughput Single-Cell RNA-Seq Systems. *Molecular Cell*, *73*(1), 130-142.e5. https://doi.org/10.1016/j.molcel.2018.10.020

Ziegenhain, C., Vieth, B., Parekh, S., Reinius, B., Guillaumet-Adkins, A., Smets, M., Leonhardt,

H., Heyn, H., Hellmann, I., & Enard, W. (2017). Comparative Analysis of Single-Cell RNA Sequencing Methods. *Molecular Cell*, *65*(4), 631-643.e4. https://doi.org/10.1016/j.molcel.2017.01.023

List of publications

Kozak, E. L., Palit, S., Miranda-Rodríguez J. R., Janjic A., Böttcher, A., Lickert, H., Enard, W., Theis, F., López-Schier, H. (2020) Epithelial Planar Bipolarity Emerges from Notch-mediated Asymmetric Inhibition of Emx2, Current Biology**,** volume 30, issue 6, P1142-1151.E6, https://doi.org/10.1016/j.cub.2020.01.027

(*in preparation*) Kozak, E. L.*, Miranda-Rodríguez, J. R.*, Borges, A., Dierkes, K., Mineo, A., Pinto-Teixeira, F., Viader-Llargués, O., Chara, O., López-Schier, H. Symmetry breaking regularizes collective cell rotations in a mechanosensory organ.
*equally contributing authors

Conference presentations:

Arnold Sommerfeld School on the Physics of Life
7.10. – 11.10. 2019, München, Germany
Poster presentation: Establishment of epithelial planar bipolarity

Circuits and Behavior in Tuscany
19.6. – 24.6. 2019, Montecastelli, Italy
Oral presentation: Establishment of bipolar epithelium

Computational Single Cell Genomics
26.3. – 27.3.2019, München, Germany
Poster presentation: Single-cell transcriptional profiling as a tool for understanding subtle cell differences

Stem Cells and Cellular Plasticity internal seminar
5.11.208, München, Germany
Oral presentation: Mechanisms of Cellular Dynamics and Differentiation in Zebrafish Neuromasts

Engineering Multicellular Self-Organisation III

3.9. – 4.9. 2018, Cambridge, UK

Poster presentation: Exploring the cellular dynamics underlying organ morphostasis and regeneration

Opening of the stem cell center meeting,

14.12. – 15.12.2017 München, Germany

Poster presentation: Wnt involvement in neuromast size and self-assembly